UNIVERSITY OF CONCEPCION - CHILE
DEPARTMENT OF ELECTRICAL ENGINEERING

Suitability of axial-flux matrix-rotor induction motors for low-speed high-torque applications: a robust design approach

by

Carlos Felipe Ignacio Madariaga Cifuentes

Supervisor

Juan Antonio Tapia Ladino

Concepcion, July 2024

A thesis submitted for the degree of

DOCTOR OF ENGINEERING SCIENCES
with a specialization in electrical engineering

Suitability of axial-flux matrix-rotor induction motors for low-speed high-torque applications: a robust design approach

Carlos Felipe Ignacio Madariaga Cifuentes

A thesis from

Department of Electrical Engineering

Submitted in Partial Fulfillment of the Requirements for the Degree of Doctor of Engineering Sciences, with Specialization in Electrical Engineering of the Graduate School of the University of Concepcion, Chile

July 2024

Abstract

Suitability of axial-flux matrix-rotor induction motors for low-speed high-torque applications: a robust design approach

Carlos Felipe Ignacio Madariaga Cifuentes
Universidad de Concepción, 2024

Low-speed high-torque (LSHT) electrical machines have been dominated by permanent magnet synchronous machines, given their high torque density, efficiency and power factor. Nevertheless, in direct-drive low-speed applications, a solution consisting of a conventional induction machine and a mechanical converter is used considering the self-starting capability of the IM and acceptable efficiency of the system. The solution for direct-drive LSHT applications is to adopt machines with inherently low speed, self-starting capacity, and high performance, which has not been possible to date from conventional induction machines and synchronous reluctance machines. In this regard, this thesis addresses the sizing, analysis, and optimization of axial flux induction motors with a novel matrix structure rotor (AF-MRIM) to meet the requirements of LSHT applications. Furthermore, in order to identify the competitivity of these machines and their application niche, opening a path to further research on this promising topology, considering both deterministic and robust design features.

Firstly, an analytical pre-sizing methodology focusing on the main and particular design parameters of an AF-MRIM is provided, considering guidelines for a suitable selection of the matrix rotor structure. A semi-analytical tool based on finite element simulations was specifically devised to quickly assess the performance of AF-MRIM, simplifying the matrix rotor structure, and enabling the time-efficiency design and multi-objective optimization of an AF-MRIM, unfeasible to perform with conventional techniques so far.

Secondly, several finite-element tools and solutions to assess the effect of unavoidable, manufacturing and assembly tolerances on the performance of asynchronous and synchronous machines are presented, meant to serve as input for a detailed comparative analysis between different machine designs from deterministic and robust design approaches.

Finally, a detailed comparison of optimized AF-MRIM with other non-conventional and conventional topologies is provided, considering raw performance and robust design capability. Two objective speeds (250 and 500 rpm) are evaluated by means of specific design optimization and

robustness assessment of the different topologies. It was demonstrated that an optimized AF-MRIM has superior performance among rare-earth free topologies but does not reach the performance and torque density of an optimized PMSM. Nonetheless, the MRIM has the highest robustness ratings of all the four selected topologies. At last, it was found that the proposed matrix-rotor IM is actually suitable for LSHT applications, with significant superiority at 250 rpm, direct-drive operation; and slight advantages at 500 rpm when compared to prominent rare-earth free topologies.

To the past, present and future students of L.E.M.E.

Acknowledgments

This work was supported in part by the Agencia Nacional de Investigación y Desarrollo (ANID), Chile, under:

- Grant ANIDPFCHA/Doctorado Nacional/2020-21200350
- Project FONDECYT REGULAR 1230670.
- Project FONDEF ID21I10099

Table of Contents

Table List

Figure List

Nomenclature

Uppercase

A	: Peak linear current density
$A_{\mathrm{fe,r}}$	: Cross-sectional area of the ferromagnetic material of one rotor pole
A_{slot}	: Stator slot area
B_{r}	: Magnet remanence
$\hat{B}_{\mathrm{rotor}}$	: Maximum flux density value in rotor electrical steel
$\hat{B}_{t}$	: Maximum flux density value in stator tooth
$\hat{B}_{\mathrm{ys}}$	: Maximum flux density value in stator yoke
$\hat{B}_{\delta}$	: Maximum value of airgap flux density
D_{fe}	: Iron wire diameter
D_{i}	: Inner diameter
D_{o}	; Machine outer diameter
D_{ri}	: Rotor inner diameter
D_{ring}	: Outer diameter of short-circuit ring
D_{ro}	: Rotor outer diameter
D_{si}	: Stator inner diameter
D_{so}	: Stator outer diameter
E_{max}, E_{f}	: Stator non-load induced voltage (max and rms)
F	: Number of failures considered within the tolerance range.
J_{o}	: Overload current density
$\mathrm{J}_{\mathrm{rated}}$	: Rated current density
J_{r}	: Rotor current density
J_{s}	: Stator current density
J_{w}	: Worst current density.
$\boldsymbol{M}_{\mathbf{tol},\boldsymbol{i}}$	: Tolerance matrix of the i-th parameter
N	: Number of winding turns
N_{l}	: Number of stator winding layers
N_{p}	: Number of parameters
$\mathrm{N}_{\mathrm{fe,columns}}$	: Number of iron wire columns within the copper matrix structure
$\mathrm{N}_{\mathrm{fe,rows}}$	: Number of iron wire rows within the copper matrix structure.
N_{phase}	: Turns per phase
N_{m}	: Rotor synchronous speed
N_{su}	: Number of structural units
$\overline{PF}$	: Median of power factor
PF_{w}	: Worst power factor
P_{i}	: Parameter number *i*
$P_{i,\mathrm{f}}$	: Faultless value of the i-th parameter
P_{r}	: Rated output power
Q_{eval}	: Number of evaluations required for full-range tolerance analysis.
R_{b}	: Inner barrier radius
T_{f}	: Torque waveform of the flawless machine
$\overline{T}_{\mathrm{m}}$	: Median of mean torque

$T_{\mathrm{m},w}$	: Worst mean torque
$\mathrm{T}_{\mathrm{o}_{\mathrm{rp}}}$	: Overload torque ripple
$\mathrm{T}_{\mathrm{o}_{\mathrm{mean}}}$	: Overload mean torque
T_{r}	: Rated torque
$\overline{T}_{\mathrm{rp}}$	: Median of torque ripple
$\mathrm{T}_{\mathrm{r}_{\mathrm{rp}}}$	: Rated torque ripple
$T_{\mathrm{rp},w}$	: Worst torque ripple
T_{max}	: Maximum torque
$\mathrm{T}_{\mathrm{RSU}}$	: Torque of the machine with deviated reference structural unit.
T_{stall}	: Stall torque
Q_{r}	: Rotor slot count
Q_{s}	: Stator slot count.
V_{overall}	: Overall volume
V_{ph}	: Phase voltage

Lowercase

b	: Number of flux barriers per pole
b_{o}	: Slot opening
b_{oef}	: Effective slot opening
b_{s}	: Slot width
$\cos\phi$	: Power factor
$\cos\phi_{\mathrm{max}}$	: Maximum power factor
$\cos\phi_{\mathrm{o}}$	: Overload power factor
d_{fe}	: Distance between adjacent iron wires
f	: Supply frequency.
i, j, k	: Counters
$\mathrm{k}_{\mathrm{air}}$	: Insulation ratio
k_{c}	: Carter factor
k_{fill}	: Fill factor.
k_{matrix}	: Rotor iron proportion.
k_{si}	: *i*-th harmonic of the pitch factor
k_{di}	: *i*-th harmonic of the distribution factor
k_{pi}	: *i*-th harmonic of the slot opening factor
$k_{\mathrm{w}i}$	: *i*-th harmonic of the winding factor
h_{fe}	: Vertical distance between aligned iron wires
h_{pm}	: Magnet height
h_{s}	: Slot height
h_{s0}	: Squirrel cage depth
h_{tt}	: Tooth-tip height
h_{tt1}	: Tooth-tip minor height
h_{tt2}	: Tooth-tip major height
h_{yr}	: Rotor yoke height
h_{ys}	: Stator yoke height

l_{stk}	: Stack length
l_{r}	: Rotor axial length
h_{r}	: Rotor height (axial length for the MRIM)
n	: Distance in number of structural units
n_{cond}	: Number of conductors per slot layer
p	: Number of pole pairs
$\mathrm{s_o}$	: Overload slip
$\mathrm{s_r}$	: Rated slip
$t_{b\,q}$	: Flux barrier width q-axis
$t_{b\,dr}$	: Flux barrier width d-axis (right)
$t_{b\,dl}$	: Flux barrier width d-axis (left)
$t_{\mathrm{simulation}}$	: Simulation time.
$\mathrm{w_q}$	: Width between barriers

Symbols

ΔP_i	: Maximum deviation of the *i*-th parameter (tolerance boundary)
α	: Aspect ratio
$\mathrm{\alpha_i^e}$	: Current angle
α_{r}	: Flux barrier position (right)
α_{l}	: Flux barrier position (left)
β	: Geometric factor
$\mathrm{\beta_r}$	: Flux barrier opening (right)
$\mathrm{\beta_l}$	: Flux barrier opening (left)
δ	: Airgap length
δ_{e}	: Equivalent airgap length
$\mathrm{\eta_o}$	: Overload efficiency
η_{max}	: Maximum efficiency
η_{r}	: Rated efficiency
η_{w}	: Worst efficiency
γ	: Geometric factor; also mechanical angular shift for tolerance analysis.
ω	: Rotational speed in rad/s
Φ	: Magnetic flux
$\hat{\phi}_{\delta\mathrm{pole}}$	: Maximum magnetic flux crossing the airgap per pole
$\hat{\phi}_{\mathrm{rotor,pole}}$	: Maximum magnetic flux crossing the rotor per pole
$\hat{\phi}_{\mathrm{ts,pole}}$	: Maximum magnetic flux traveling through the stator teeth
$\hat{\phi}_{\mathrm{ys,pole}}$	: Maximum magnetic flux traveling through the stator yoke
σ	: Standard deviation
τ_s	: Slot pitch in m
μ_{r}	: Relative recoil permeability
μ_{PMS}	: Permeability of the equivalent PMS model.
μ_x	: x-axis permeability
μ_y	: y-axis permeability
μ_y	: z-axis permeability
$\xi_{i,j}$	: Tolerance error of the *i*-th parameter of the *j*-th structural unit

ξ : Ratio between induced voltage and input phase voltage.

Abbreviatures

Uppercase

AC	: Alternating current
AF	: Axial flux
AFIM	: Axial flux induction machine
AR-AFIM	: Axial flux induction machine with anisotropic rotor
CAD	: Computer-aided design
CNC	: Computer numerical control
DC	: Direct current
DL	: Double layer
DOE	: Design of experiments
EMF	: electro-motive force
FE	: Finite element
FEA	: Finite element analysis
FEM	: Finite element method
GO	: General objective
LSHT	: Low-speed high-torque
IM	: Induction machine/motor
MMF	: Magneto-motive force
MOGA	: Multi-objective genetic algorithm
MPMSM	: Modular permanent magnet synchronous machine
MR	: Matrix rotor
MUMPS	: Multifrontal massively parallel sparse direct solver
PM	: Permanent magnet
PMS	: Progressive model simplification
PMSM	: Permanent magnet synchronous machine
RAM	: Random access memory
RF	: Radial flux
RMS	: Root mean square
RSU	: Reference structural unit
SC	: Squirrel cage
SCIM	: Squirrel cage induction motor
SL	: Single layer
SO	: Specific objective
SU	: Structural unit
SSD	: Solid state drive
SynRM	: Synchronous reluctance machine
UUM	: Uniform-uncertainty method
1D	: One-dimensional
2D	: Two-dimensional
3D	: Three-dimensional

Lowercase

rpm	: revolutions per minute
p.u.	: per unit

1. Introduction

1.1. General introduction

PMSMs have become the predominant choice in general LSHT applications due to their high torque density, efficiency and power factor [1]-[3]. However, within direct-drive LSHT applications, a frequently adopted configuration involves integrating a conventional IM with a mechanical converter, chosen for its cost-effectiveness and inherent self-starting capability [4]-[5]. Nonetheless, this solution comes at the expense of a more complex system design and comparatively lower efficiency [6]-[7]. Owing to the operational stresses of high torque and friction, regular maintenance becomes imperative, leading to diminished reliability and elevated system costs [8]. As a result, there has been a growing focus on enhancing the performance of LSHT drive systems utilized in industrial applications.

A known solution for direct-drive LSHT applications involves designing machines with inherently low speed, self-starting capability, and high performance. One approach is to consider induction machines with a high pole count, which reduces synchronous speed and enables direct connection to the load. Nevertheless, conventional high-pole-count induction machines suffer from low power factor and efficiency issues, despite ambitious attempts to achieve acceptable performance [9]-[10]. Alternatively, SynRMs featuring a dual-stator and innovative rotor structure have been also proposed as a rare-earth free option, operating within the 300-500 rpm range [11]. These machines achieved an impressive 87% efficiency, but they exhibit high ripple torque as a trade-off.

In this context, for high pole-count applications, axial flux induction motors (AFIM) have emerged as a viable choice due to several advantages over their counterparts: compactness, shorter axial length and higher power density [12]-[16]. AFIMs can be categorized based on the number of stators and rotors, the simplest configuration being single-rotor and single-stator setups, as shown in Fig. 1.1(a). More complex configurations with multiple rotors and stators are employed in high-power applications to minimize mechanical stress on bearings [17].

FE modelling and analytical studies of various AFIM topologies are extensively documented in recent literature [6],[15],[18]-[20], highlighting their potential and applicability across several applications. However, while AFIM present an attractive option for LSHT applications, they are prone to high leakage flux [15],[21]-[22]. This diminishes their overall performance and can lead to significant reductions in back-EMF, increased ripple torque, and other undesired effects [23]-[25].

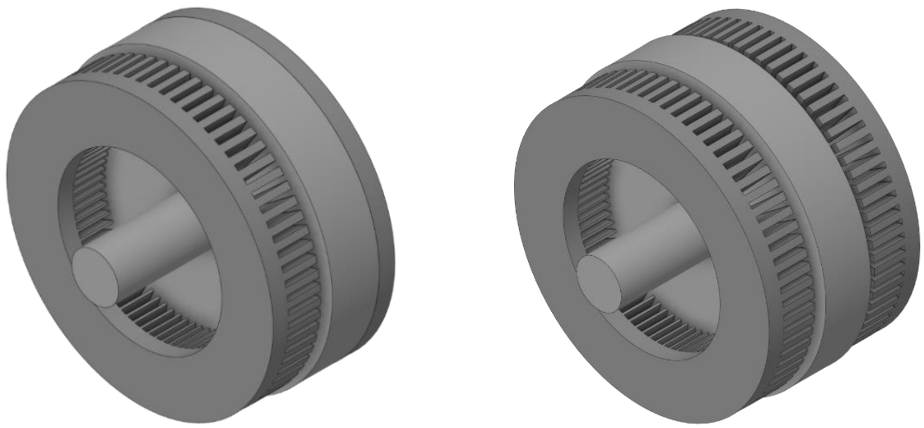

(a) (b)

Fig. 1.1 AFIM configurations based on rotor/stator count.
a) single-stator single-rotor, b) double-stator and single-rotor.

A promising solution to mitigate this drawback involves changing the rotor structure, as initially proposed in [21], by adopting a solid matrix rotor with anisotropic magnetic properties. This is accomplished by embedding evenly spaced iron wires within a solid copper rotor, as illustrated in Fig. 1.2.

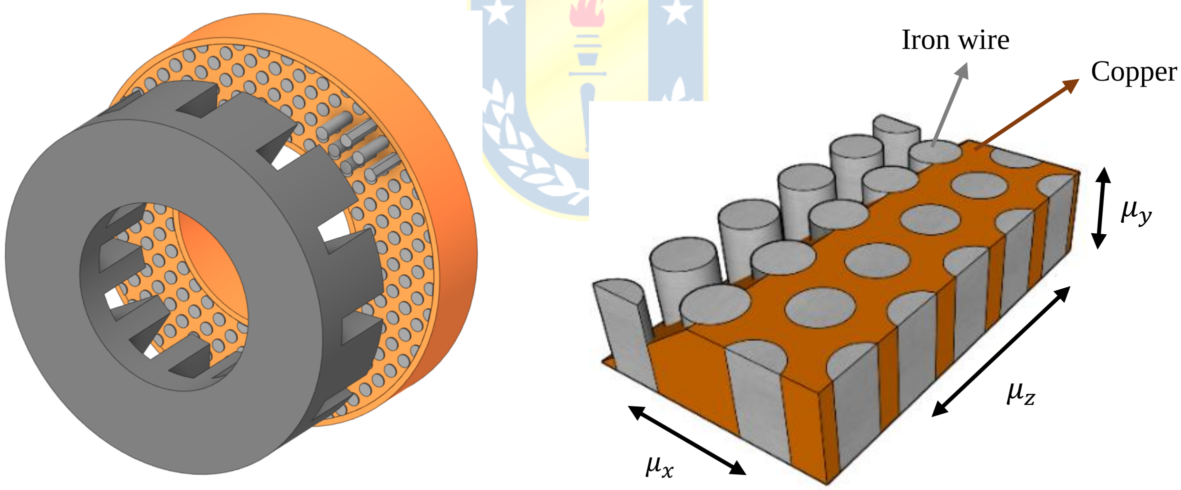

(a) (b)

Fig. 1.2 Schematics of a matrix rotor structure.
(a) Single-stator single-rotor AFIM with matrix rotor structure; (b) Close-up to the iron-copper arrangement comprising the matrix rotor.

The arrangement of iron wires exhibits high permeability in the axial direction (μ_y as depicted in Fig. 1.2), facilitating the flow of flux density lines in that orientation while maintaining low permeability in other directions to minimize leakage flux. Furthermore, the copper-iron configuration and short-circuit rings enable the free circulation of currents through the rotor structure, thereby reducing equivalent resistance [26]. However, despite the promising initially put forward by this machine design, the computational resources and design considerations were significantly different from today's capabilities. Large-scale 3D FE analysis of various designs and FE-based optimization routines were not feasible by the time this machine was proposed. As a result, the machine's competitiveness and its specific application niche were never fully explored or disclosed [27].

Recent FE evaluations of an AFIM with matrix rotor have demonstrated promising results, showing increased electromagnetic torque and reduced ripple torque and noise compared to an AFIM with a conventional cage rotor [6]. Moreover, advancements in manufacturing technologies such as additive manufacturing are enabling the development of novel and unconventional electrical machines [28]-[31], potentially enhancement the competitive edge of AF-MRIM. However, several aspects related to the design, manufacturing and assembly of these machines have not been fully disclosed so far, as described in the following sections.

1.2. Literature review

This section begins by examining recent research on modern electrical machine design, focusing on robust design optimization, as well as on techniques that allow a rapid evaluation of multiple design candidates. Subsequently, research on AFIMs is identified and discussed, followed by a description of the findings of recent studies on AF-MRIM. Finally, the identified research gap is described and discussed.

1.2.1 Modern industrial electrical machine design: robust design optimization

In search of enhancing electrical machine performance, such as achieving higher power density and efficiency or reducing manufacturing costs, various design optimization methods have been developed and documented in technical literature. These methods can be classified into deterministic or robust approaches, depending on how they handle uncertainties [32]. The deterministic approach has dominated the field of electrical machine optimization for several decades [33]-[40]. Through the disclosure and analysis of the Pareto front, this method enables designers to identify the best electrical machine candidates while managing computational time effectively. However, the deterministic approach overlooks uncertainties inherent in the electrical machine industry, such as material variations and manufacturing tolerances [32],[41]-[43]. These uncertainties can significantly affect machine performance [44]-[46], deviating from the originally intended specifications, a critical issue in mass production. Addressing this issue requires stringent quality control and management practices to ensure consistent manufacturing quality, which can impose additional time and costs, particularly burdensome for small and medium-sized enterprises. To tackle these challenges, robust design optimization methods have been developed to assess the impact of potential uncertainties early in the product development stages, particularly for electrical machines.

The primary goal of the robust design approach is to identify designs that exhibit minimal sensitivity to variations in design variables and predefined parameters [32], [42], [44], as well as identifying the design robustness. A robust design is characterized by its ability to maintain expected performance, even in the face of unavoidable manufacturing or assembly tolerances [41]. Fig. 1.3 illustrates a basic optimization scenario (maximization) where a target *y* depends on a parameter *x*. In the optimal solution depicted, a slight change in parameter *x* leads to a significant decrease in *y* value, indicating a lack of robustness. Conversely, the robust solution, while yielding a lower *y* value initially, demonstrates minimal sensitivity to such variations in *x*, avoiding performance degradation.

Identifying robust designs typically requires dealing with a tradeoff between rated performance and robustness [47]. Therefore, it is critical to determine which performance indicators can be adjusted to enhance robustness. This assessment should be preceded by a comprehensive sensitivity analysis, taking into account the specific requirements of the machine's intended application.

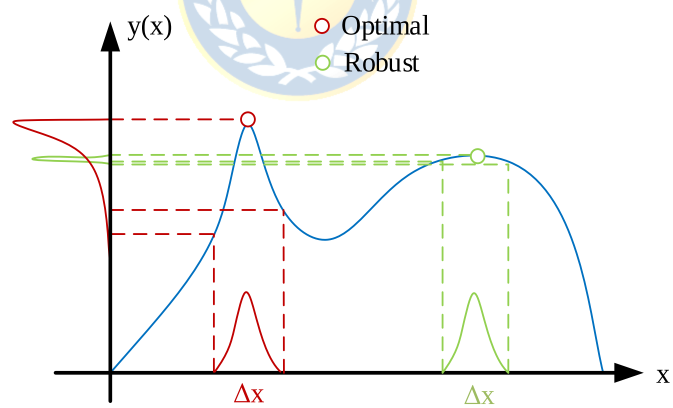

Fig. 1.3 Example illustrating the difference between an optimal and a robust solution for a single parameter decision.

As discussed in the literature, robust design optimization of electrical machines poses a computational challenge due to the extensive simulation time required for evaluating robustness. Assessing numerous design candidates using FE simulations to account for asymmetry and material uncertainties results in substantial time investments. Moreover, when dealing with a large number of dimensional parameters subject to tolerances, direct FE simulations for robustness become impractical, necessitating the use of complementary analytical or semi-analytical tools [41].

In response to these challenges, recent research has introduced space reduction optimization strategies aimed at reducing computational overhead and minimizing the number of design evaluations [32], [48]. In the past decade, superposition techniques have been implemented and validated for MPMSMs and PMSMs [41], [49]-[50]. These methods reconstruct torque waveforms by analyzing the contribution of individual pole-pairs, and in some cases, even individual magnets or slots. Robustness indicators can be derived through a comprehensive analysis of the superposition method results, involving statistical evaluation across a set of representative machine designs, as discussed in [41] and [50].

While these modern design techniques have already been applied to PMSMs and SynRMs [50], research on AFIM has taken a deterministic approach so far, as outlined in the following sections.

1.2.2 Research on axial flux induction machines

Efforts in the literature have focused on analyzing the electromagnetic, mechanical and thermal responses of AFIMs, highlighting key design aspects and underlining the potential and applicability of these machines across various applications.

The impact of design parameters on the performance of AFIMs has been analyzed in [51]-[52], focusing on stator and rotor structures, particularly the number of slots and airgap length. In [51], numerical methods evaluate the influence of slot number on an aluminum-cage AFIM with a solid-rotor, revealing that an increased number of slots severely impacts electromagnetic performance, reluctance torque, rotor losses and power factor. The study discourages the use of an odd number of slots due to resulting unbalanced magnetic forces. While FE simulations support these findings, the study does not extend to prototyping or assembly considerations. In turn, [52] addresses the impact of the airgap length on AFIM performance. The authors emphasize the importance of selecting and appropriate airgap length, as it significantly influences the motor’s efficiency and power factor. The authors also highlight the necessity for meticulous design of AFIMs due to the severe eddy-current losses observed when these machine are fed by frequency converters.

The proposal of design improvements and novel designs of AFIMs can be found in [53]-[55], based on stacking machine structures, reducing rotor yoke dimensions, and implementing adjustable airgaps. In [53], the authors analyze a stack configuration comprising two partial machines based on single-stator SC-AFIMs, discussing performance improvements achieved by reducing the rotor yoke. The authors observe increased stator current due to enhanced magnetic coupling compared to single induction machines, resulting in higher copper losses. Also, operational recommendations are provided for these magnetically coupled machines, valuable for exploring multiple-stator multiple-rotor AFIM configurations. In [54], a novel single-rotor single-stator AFIM with an adjustable airgap length is presented, while [55] enhances this design further by introducing a novel radial slot opening shape. The designs proposed in both studies enable minimization of the airgap, addressing the high magnetic pull typical in axial machines. As a result, these design refinements significantly boost motor performance compared to configurations with longer airgaps.

Analytical models of various AFIM designs can be found in [12], [15], [56]-[57], aimed at providing sizing methodologies and estimating performance indicators. In [15], an analytical and numerical evaluation of a single-stator, single rotor AFIM prototype with a copper squirrel cage is presented. The authors emphasize the key design parameter of the copper-iron ratio in the rotor structure, which directly affects rotor core saturation and magnetizing current requirements. In [56], a preliminary electromagnetic sizing algorithm for double-rotor AFIMs is presented, utilizing a geometric approach to develop equations for key machine parameters. The algorithm's efficacy is validated using FE simulations with exact dimensions, although manufacturing or assembly tolerances are not considered. In [57], a dual-stator solid-rotor AFIM is analyzed using a multi-slice and multi-layer method. The authors treat the machine as a set of linear induction motors, allowing fast assessment through Maxwell's equations. The electromagnetic field distribution computed analytically aligns well with FEM results. In turn, the electromagnetic torque, efficiency, and power factor of a 5 kW, 7100 rpm prototype was validated by means of FE simulations and experimental testing, demonstrating acceptable accuracy. More recently, [12] presents an analytical model of an AFIM with a solid rotor. The study proposes a quasi-3D analytical method to estimate eddy currents, complemented by 1D and 2D analytical expressions for torque calculation. Comparison with 3D FE simulations and experimental data shows good concordance, accompanied by optimization guidelines aimed at enhancing torque characteristics at higher speeds.

In summary, AFIMs featuring magnetically isotropic rotor have been studied in recent technical literature through the development of precise analytical models, FE evaluations and prototype assessments. However, as of yet, the robust design approach has not been covered for this topology.

1.2.3 Research on AFIM with anisotropic rotor structure

While very useful for designing AFIMs, the studies described in the previous section do not cover AFIMs with an anisotropic rotor. This distinction is crucial because the magnetic properties and electromagnetic response of AF-MRIMs differ significantly from those of conventional AFIMs [21],[58]. Therefore, analytical and semi-analytical tools used for isotropic rotor AFIMs cannot be directly applied to AF-MRIMs due to differing rotor modeling assumptions. In this regard, [58] proposes an initial analytical method to estimate the flux density distribution and electromagnetic torque in AF-MRIMs based on solutions to Maxwell's equations. However, the rotor is treated as homogeneous, with simplified characteristics represented by different fixed permeabilities along axes. While the model assesses electromagnetic torque, it lacks validation through FE simulations or experimental results.

Recently, in [22], analytical expressions based on a multilayer model (depicted in Fig. 1.4) were developed to cover a broader range of parameters: rotor resistance and reactance, input current per stator as a function of the slip, and efficiency. Using this model, the efficiency of a 25 HP AFIM was estimated between 85% to 90% during low-slip operation (neglecting mechanical and yoke iron losses), and the torque-slip characteristic was analyzed for slip values ranging from 0 to 1. The model's validity was confirmed through evaluation against a simplified 2D FE model, which did not incorporate rotor magnetic anisotropy due to the absence of the iron-copper arrangement.

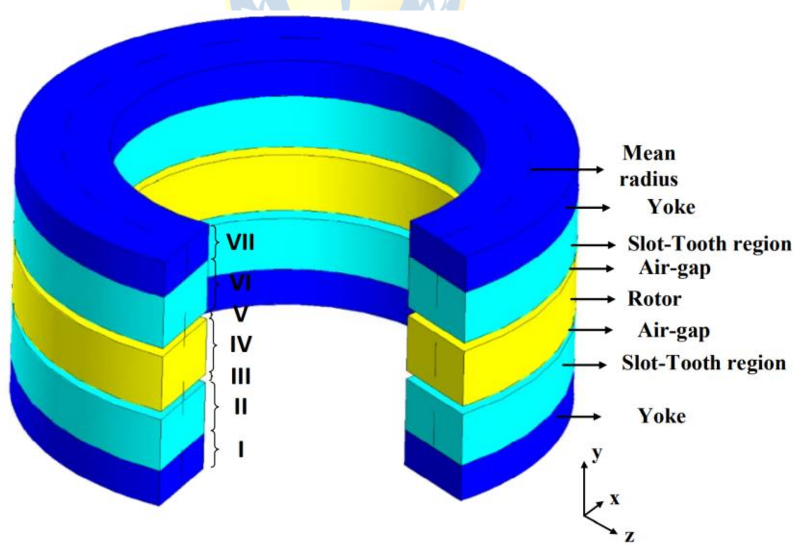

Fig. 1.4 Multilayer model of an AFIM and its 3D representation. [22].

In turn, [27] explores the impact of varying key structural parameters on the performance of an AF-MRIM. Torque-slip characteristic, efficiency and power factor were assessed using FE analysis of two 3D models of a 72-slot 24-pole machine. Findings indicate that reducing rotor thickness or slot height can trigger a performance reduction at low-slip operation, while decreasing the airgap length notably enhances torque, efficiency, and power factor. Moreover, results from [22] were partially challenged as the inclusion of rotor structure in 3D simulations revealed an efficiency close to 60%, significantly lower than the 85% to 90% estimated by the simplified model in [22] for the same machine design.

1.2.4 Comments and research gap.

Recent research found in [22] provides a robust foundation for designing AF-MRIMs, yet the proposed models exhibit inaccuracies in assessing efficiency and power factor. These performance indices are notably overestimated when compared to findings from 3D FE simulations [27] or experimental prototypes, primarily due to manufacturing tolerances. Moreover, there is a notable absence of literature addressing fabrication, assembly, or material degradation effects on machine performance, despite their recognized significance in moder machine design practices.

The assembly of an AFIM faces several challenges related to achieving a uniform airgap and managing inevitable manufacturing tolerances, which are more pronounced when employing a matrix-rotor structure [6]. However, while stator and rotor imperfections may be difficult to eliminate entirely, proactive design measures can mitigate their impact.

In summary, several aspects of AF-MRIM design remain undiscovered, including manufacturing and assembly considerations, tolerance analysis results, robust design methodologies, anisotropic rotor modelling, competitive analysis against conventional machines, and more. Addressing these aspects comprehensively is crucial for accurately identifying the application niche of these machines in LSHT applications.

1.3. Hypothesis

By means of robust design techniques, it is possible to improve both the performance and the sensitiveness of AF-MRIM designs to the extent that they surpass those of conventional machines for industrial applications.

In addition, the following research questions are raised:

- *What is the application niche in which AF-MRIMs have superior performance compared to state-of-the-art topologies?*
- *Which are the AF-MRIMs parameters involved in the trade-off between robustness and raw performance?*

- *How much can the sensitiveness of AF-MRIMs be reduced considering typical tolerance limits?*

1.4. Objectives

In this section, the general and specific objectives defined that aim to fill the identified research gap are presented.

1.4.1 General Objective (GO)

Identify, optimize, and evaluate designs of axial flux induction motors with matrix rotor structure that provide superior performance to that of other conventional machines in low-speed high-torque applications from a robust design approach.

1.4.2 Specific Objectives (SO)

- **SO1:** Develop generalized semi-analytical methods applicable to AF-MRIM that provide a quick and accurate estimation of the efficiency, losses, torque and power a given prototype can develop, considering exact dimensions and material properties of the matrix rotor.
- **SO2:** Develop and implement a methodology based on finite element solutions that includes the effect of unavoidable manufacturing and assembly tolerances when assessing the performance of AF-MRIM, providing guidelines to address the key parameters that have the most impact from a design standpoint.
- **SO3:** Evaluate and compare the performance and robustness of multiple AF-MRIM designs against other AFIM topologies and conventional machines in low-speed high-torque applications.
- **SO4:** Provide guidelines to optimal and robust design of AFIM for low-speed high-torque applications.

2. Productivity and contribution

Findings of this thesis have been documented in various conference papers and journal articles, detailed below. Notable contributions include: i) the development and validation of a pre-sizing methodology for AF-MRIMs; ii) identification of key parameters influencing AF-MRIM performance; iii) comparison of robustness and performance indicators between state-of-the art topologies and AF-MRIMs, and iv) guidelines for efficient robust identification and optimization of AF-MRIMs.

The journal and conference papers resulting from this thesis are listed as follows:

2.1. Journal papers

2.1.1 As first author

- **C. Madariaga**, C. Gallardo, N. Reyes, J. A. Tapia, W. Jara and M. Degano, " Time-Efficient Design Refinement of Induction Motors with Matrix-Rotor Structure for Low-Speed High-Torque Applications," IEEE Transactions on Energy Conversion (*sent*).
- **C. Madariaga**, C. Gallardo, N. Reyes, J. A. Tapia, W. Jara and M. Degano, " Design and evaluation of matrix rotor induction motor for high-torque low-speed applications," IEEE Transactions on Energy Conversion (*accepted*).
- **C. Madariaga**, C. Gallardo, J. A. Tapia, W. Jara, A. Escobar and M. Degano, "Fast assessment of rotor barrier dimensional allowances in synchronous reluctance machines," in IEEE Access, vol. 11, pp. 58349-58358, Jun. 2023.

2.1.2 As a relevant contributor

- A. Escobar, G. Sánchez, W. Jara, **C. Madariaga**, J. A. Tapia, J. Riedemann, E. Reyes, "Impact of manufacturing tolerances on axial flux permanent magnet machines with ironless rotor core: a statistical approach," Machines, vol. 11, no. 5, p. 535, May 2023.
- C. Gallardo, **C. Madariaga**, J. A. Tapia, and M. Degano, "A method to determine the torque ripple harmonic reduction in skewed synchronous reluctance machines," Applied Sciences, vol. 13, no. 5, p. 2949, Feb. 2023.
- D. Riquelme, **C. Madariaga**, W. Jara, G. Bramerdorfer, J. A. Tapia, and J. Riedemann, "Study on stator-rotor misalignment in modular permanent magnet synchronous machines with different slot/pole combinations," Applied Sciences, vol. 13, no. 5, p. 2777, Feb.

2023.

2.2. Conference papers

2.2.1 *As first author*

- **C. Madariaga**, J. E. Ruiz-Sarrio, J. A. Antonino-Daviu, C. Gallardo, Juan. A. Tapia, "Non-invasive bar breakage diagnosis of axial flux induction machines through steady-state signal analysis," in IEEE Energy Conversion Congress and Expo (ECCE), Phoneix, Arizona, Oct. 2024 (*accepted*).
- **C. Madariaga**, J. E. Ruiz-Sarrio, J. A. Antonino-Daviu, C. Gallardo, Juan. A. Tapia, "Broken bar detection of axial-flux induction machines through advanced transient current signature analysis," in 26th International Conference on Electrical Machines (ICEM), Torino, Italy, Sep. 2024 (*accepted*).
- **C. Madariaga**, C. Gallardo, Juan. A. Tapia, W. Jara, N. Reyes and F. Santacruz, "Comparison of matrix-rotor induction motor and permanent magnet machine for low-speed high-torque applications," in 2023 IEEE CHILEAN Conference on Electrical, Electronics Engineering, Information and Communication Technologies, Valdivia, Chile, Dic. 2023.
- **C. Madariaga**, C. Gallardo, Juan. A. Tapia, W. Jara and D. Riquelme, "Quick comparison of the cogging torque severity in permanent magnet synchronous machines with segmented stator core," in 2022 IEEE International Conference on Automation/XXV
- **C. Madariaga**, J. Tapia, N. Reyes, W. Jara, M. Degano, "Influence of constructive parameters on the performance of an axial-flux induction machine with solid and magnetically anisotropic rotor," in IEEE Energy Conversion Congress and Exposition (ECCE), Vancouver, Canada, Oct. 2021.

2.2.2 *As a relevant contributor*

- N. Reyes, M. Jiménez, A. Hoffer, **C. Madariaga**, C. Gallardo, J. A. Tapia, W. Jara, M. Degano, "Structural feasibility and electromagnetic analysis of an ironless-rotor axial flux permanent magnet synchronous machine," in 15th IEEE Energy Conversion Congress and Expo (ECCE), Nashville, TN, Oct./Nov. 2023.

- C. Gallardo, **C. Madariaga**, J. A. Tapia, M. Degano, “Effects of rotor asymmetries on d-q axis parameters in synchronous reluctance machines,” in International Electric Machines and Drives Conference (IEMDC), San Francisco, CA, USA, May. 2023.
- C. Gallardo, **C. Madariaga**, V. Rodriguez, and J. A. Tapia, "Comparative analysis of a synchronous reluctance and a solid-rotor induction machine for high-speed applications," in IEEE Andean Conference (ANDESCON2022), Barranquilla, Colombia, Nov. 2022.
- A. Escobar, **C. Madariaga**, W. Jara, J. A. Tapia, M. Degano and J. Riedemann, "Continuous-domain semi-analytical method for tolerance analysis of axial flux permanent magnet machines ," in 14th IEEE Energy Conversion Congress and Expo (ECCE), Detroit, Michigan, Oct. 2022.
- D. Riquelme, **C. Madariaga,** W. Jara, J. A. Tapia, G. Bramerdorfer and J. Riedemann, "Impact of axial-varying eccentricity on the performance of PMSM with segmented stator core ", in XXV International Conference on Electrical Machines (ICEM), Valencia, España, Sep. 2022.
- E. Perez, **C. Madariaga**, W. Jara, G. Bramerdorfer, J. Tapia and J. Riedemann, "Comparison of optimized fault-tolerant modular stator machines with U-shape and H-shape core structure," in IEEE Energy Conversion Congress and Exposition (ECCE), Vancouver, Canada, Oct. 2021.
- D. Riquelme, W. Jara, **C. Madariaga**, J. Tapia, G. Bramerdorfer, J. Riedemann, “Impact of static and dynamic eccentricity on the performance of permanent magnet synchronous machines with modular stator core,” in IEEE Energy Conversion Congress and Exposition (ECCE), Vancouver, Canada, Oct. 2021.
- A. Escobar, G. Sanchez, W. Jara, **C. Madariaga**, M. Degano and J. Tapia, "Statistical analysis of manufacturing tolerances effect on axial-flux permanent magnet machines cogging torque", in IEEE Energy Conversion Congress and Exposition (ECCE), Vancouver, Canada, Oct. 2021.

2.3. Contribution

The contribution of each section of this thesis is described below.

- **Section 3** provides an analytical pre-sizing methodology that focuses on key design parameters of AF-MRIMs, emphasizing the selection of the matrix rotor structure. This methodology led to the development of a semi-analytical tool capable of efficiently evaluating AF-MRIM performance, significantly reducing computational burden by 99%. Additionally, individual sensitivity analyses were conducted to shed light on critical design parameters affecting machine performance. The proposed tools enable rapid design iterations and multi-objective optimization of AF-MRIMs, which were previously impractical with conventional techniques. Electrical machine designers are encouraged to adopt the proposed methods to accurately assess MRIM performance based on available computational resources.
- **Section 4** presents several FE tools and solutions to evaluate the impact of unavoidable, manufacturing and assembly tolerances on the performance of asynchronous and synchronous machines. Tools include UUM and non-UUM adaptations, with recommendations on their applicability and representativeness. A generalized non-UUM method is developed to evaluate the impact of unevenly distributed dimensional tolerances on torque waveform characteristics in SynRMs and PMSMs. These tools serve as inputs for comprehensive comparative analyses of machine designs from a robust design approach.
- **Section 5** provides an in-depth comparison between AF-MRIMs and other conventional and non-conventional topologies, focusing on raw performance and robust design capabilities. Specifically, two objective speeds (250 and 500 rpm) are evaluated through design optimization and robustness assessments. It is demonstrated that while optimized AF-MRIMs exhibit superior performance compared to other rare-earth free topologies, they do not match the performance and torque density of optimized PMSMs. Nonetheless, MRIMs consistently achieve the highest robustness ratings among the selected topologies. Furthermore, this section discloses the suitability and competitiveness of AF-MRIMs in LSHT applications.

3. Sizing methodology and optimization guidelines for the design of AF-MRIM

3.1. Introduction

The AF-MRIM relies on the adoption of a novel iron-copper structure of the machine rotor, as schematized in Fig. 3.1. The arrangement of iron wires exhibits high permeability in the axial direction (μ_y as depicted in Fig. 3.1), facilitating the flow of flux density lines in that orientation while maintaining low permeability in other directions to minimize leakage flux and increase relevant performance ratings.

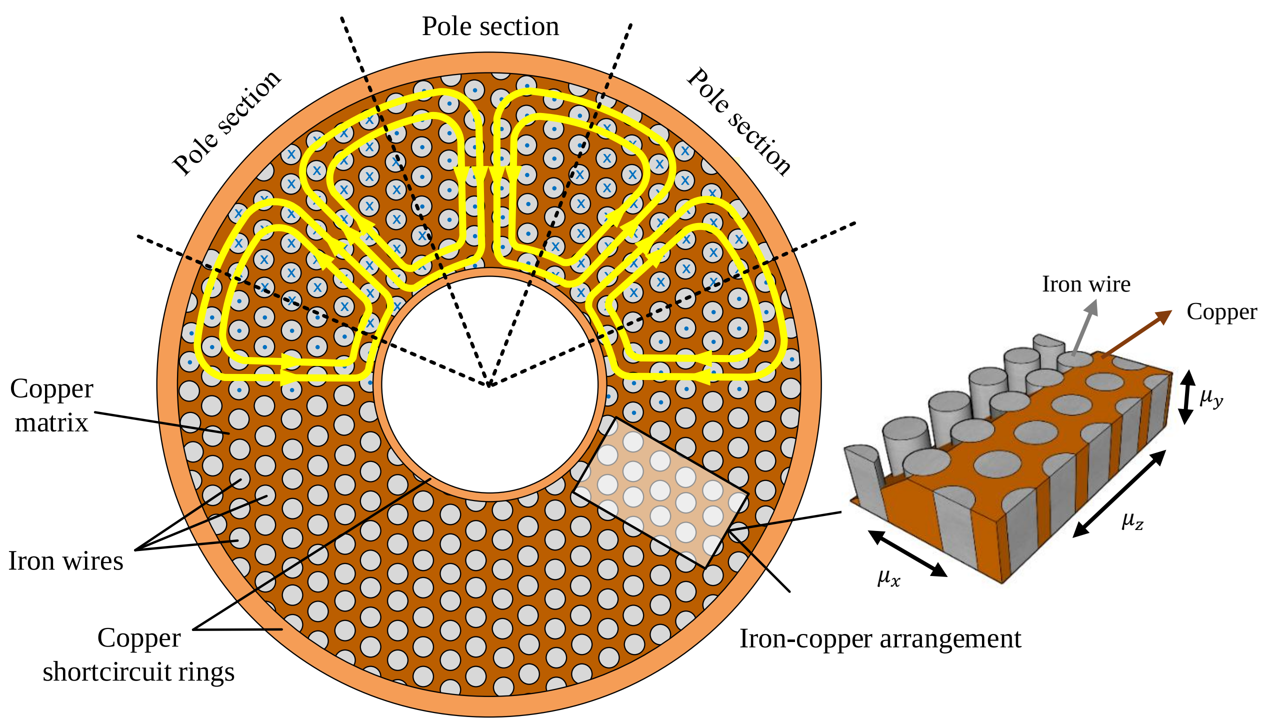

Fig. 3.1 Schematic of the anisotropic rotor structure. Magnetic flux density in the iron wires is represented as dots and crosses, and current density paths are indicated by yellow lines.

In this work, double-stator single-rotor AF-MRIM are selected for further analysis due to mechanical considerations: the dual stator setup is chosen to reduce bearing stress and facilitate the design of high torque-density machines.

The proposed design methodology begins with the development of an initial design identification process, followed by the creation and implementation of fast optimization tools to refine this initial design. This section aims to provide guidelines for selecting and enhancing specific and critical design aspects of MRIMs. An initial sizing methodology is proposed and validated, alongside recommendations for the multi-objective optimization of this machine topology. Furthermore, key dimensional parameters that significantly impact AF-MRIM performance are identified and discussed.

3.2. Analytical initial sizing and design considerations

The proposed sizing methodology of an AF-MRIM employs a conventional approach to estimate flux density within critical zones of the main magnetic circuit, adhering to dimensional constraints. This determines the most relevant stator and rotor dimensions [59].

The magnetic circuit analysis of a double-stator AF-MRIM considers the teeth and yoke of each stator, along with the airgaps and matrix rotor. Assuming identical winding arrangements for both stators, magnetic flux must cross the airgaps and matrix rotor in the axial direction. Referring to the geometry illustrated in Fig. 1.1(b), and with prescribed outer and inner diameters, the maximum magnetic flux crossing the airgap per pole ($\hat{\phi}_{\delta\mathrm{pole}}$) can be simplified to

$$\hat{\phi}_{\delta\mathrm{pole}} = \hat{B}_{\delta}\left(\frac{{D_o}^2 - {D_i}^2}{4p}\right), \tag{3.1}$$

where $\hat{B}_{\delta}$ is derived from literature and empirical data [59], and p is chosen based on the desired operational speed and available supply frequency. For direct drive applications considered in this thesis, the supply frequency is typically 50Hz or 60Hz, depending on the geographical location of implementation.

In turn, magnetic flux traveling through the stator teeth ($\hat{\phi}_{\mathrm{ts,pole}}$) and stator yoke ($\hat{\phi}_{\mathrm{ys,pole}}$) are estimated by considering the flux conservation law [59]:

$$\hat{\phi}_{ts\ \mathrm{pole}} = \frac{1}{\pi p}\hat{B}_t\left[\pi\left(\frac{{D_o}^2 - {D_i}^2}{4}\right) - \left(\frac{D_o - D_i}{2}\right) b_s Q_s\right], \tag{3.2}$$

$$\hat{\phi}_{\mathrm{ys,pole}} = 2\hat{B}_{\mathrm{ys}}\left(\frac{D_o - D_i}{2}\right) h_{\mathrm{ys}}, \tag{3.3}$$

where $\hat{B}_t$ and $\hat{B}_{\mathrm{ys}}$ are chosen from literature suggestions, considering usual tooth and stator yoke magnetic loads.

To evaluate the magnetic flux of the matrix rotor ($\hat{\phi}_{\text{rotor,pole}}$), the total cross-sectional area of the iron wires in a pole section of the rotor must be considered:

$$\hat{\phi}_{\text{rotor,pole}} = \hat{B}_{\text{rotor}} \left(\frac{{D_o}^2 - {D_i}^2}{4p} \right) \cdot k_{\text{matrix}}, \tag{3.4}$$

where k_{matrix} is the proportion between the total cross-section area of iron wires and the total pole section area. In turn, k_{matrix} depends on D_{fe} and d_{fe}. To derive the relationship between k_{matrix}, D_{fe} and d_{fe}, the rotor iron/copper arrangement is modeled after a structure resembling a beehive, as depicted in Fig. 3.2.

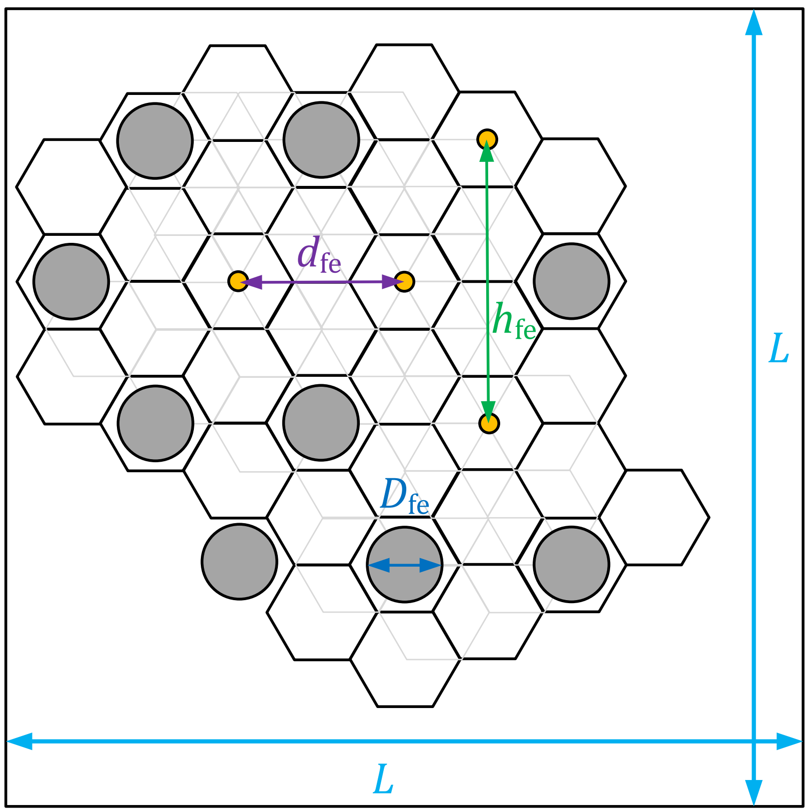

Fig. 3.2 Sketch of the iron-copper arrangement of the matrix rotor.

Given that all iron wires are equidistant, d_{fe} represents the horizontal distance between two adjacent iron wires, and D_{fe} denotes the diameter of each iron wire. In turn, h_{fe} corresponds to twice the height of an equilateral formed by three iron wires:

$$h_{\text{fe}} = 2 \cdot \left(\frac{\sqrt{3}}{2} d_{\text{fe}} \right) \tag{3.5}$$

Considering that the iron-copper arrangement is enclosed by a squared space with side L, then the number of iron wire rows inside that squared space can be estimated as:

$$\mathrm{N}_{\mathrm{fe,rows}} = \frac{L}{h_{\mathrm{fe}}/2} + 1. \tag{3.6}$$

In turn, the number of iron wire columns inside the square is given by

$$\mathrm{N}_{\mathrm{fe,columns}} = \frac{L}{d_{\mathrm{fe}}} + 1. \tag{3.7}$$

Then, the total area occupied by iron wires inside the squared space can be calculated as

$$\mathrm{A}_{\mathrm{iron}} = \left(\frac{2L}{\sqrt{3}d_{\mathrm{fe}}} + 1\right)\left(\frac{L}{d_{\mathrm{fe}}} + 1\right) \cdot \pi \left(\frac{D_{\mathrm{fe}}}{2}\right)^2. \tag{3.8}$$

Consequently, the ratio between $\mathrm{A}_{\mathrm{iron}}$ and the total area of the square is:

$$\mathrm{k}_{\mathrm{iron/total}} = \frac{\left(\frac{2L}{\sqrt{3}d_{\mathrm{fe}}} + 1\right)\left(\frac{L}{d_{\mathrm{fe}}} + 1\right) \cdot \pi \left(\frac{D_{\mathrm{fe}}}{2}\right)^2}{L^2} \tag{3.9}$$

In an AF-MRIM, the total area is assumed to be the entire rotor surface area, and $\mathrm{k}_{\mathrm{iron/total}} = k_{\mathrm{matrix}}$. In addition, the number of iron wire rows and iron wire columns is considerably high in an AF-MRIM. In such a case, $\frac{2L}{\sqrt{3}d_{\mathrm{fe}}} \gg 1$ and $\frac{L}{d_{\mathrm{fe}}} \gg 1$, and then:

$$\mathrm{k}_{\mathrm{matrix}} \cong \frac{\pi}{2\sqrt{3}}\left(\frac{D_{\mathrm{fe}}}{d_{\mathrm{fe}}}\right)^2 \tag{3.10}$$

From a magnetic standpoint, it is advisable for the iron wires to maintain a flux density value similar to that of the stator teeth. This approach helps to prevent uncontrolled rotor saturation and restrain rotor flux leakage. According to the law of magnetic flux conservation, it can be assumed that $\hat{\phi}_{\mathrm{ts,pole}} = \hat{\phi}_{\mathrm{rotor,pole}}$. Then:

$$\frac{1}{\pi p}\hat{B}_t\left[\pi\left(\frac{{D_o}^2 - {D_i}^2}{4}\right) - \left(\frac{D_o - D_i}{2}\right) b_s Q_s\right] = \hat{B}_{\mathrm{rotor}}\left(\frac{{D_o}^2 - {D_i}^2}{4p}\right) \cdot k_{\mathrm{matrix}} \tag{3.11}$$

In this regard, it is suggested that $\hat{B}_t \cong \hat{B}_{\text{rotor}}$, and (3.11) becomes

$$k_{\text{matrix}} \cong 1 - \frac{b_s Q_s}{\pi \frac{(D_o + D_i)}{2}} \tag{3.12}$$

From (3.1)-(3.4) and considering the flux conservation in the entire magnetic circuit, flux density values in the different parts of the machine can be initially selected to propose a first design. As a starting point, teeth and airgap magnetic load reference values can be found in the literature [59]-[60] or be chosen based on specific application requirements.

In turn, since the airgap length significantly influences the magnetomotive-force requirements of the magnetic circuit, the Carter factor can be useful to determine an analytical equivalent airgap:

$$\delta_{\text{e}} = k_c \delta \tag{3.13}$$

Considering standard rectangular slots, as illustrated in Fig. 3.3, k_c can be calculated following Ostovic's formulation, given by [60]:

$$k_{\text{c}} = \begin{cases} \dfrac{\tau_s}{\tau_s - \gamma\delta} & \text{, if } b_{\text{oef}} < \tau_s \\ \dfrac{1}{1-\beta} & \text{, if } b_{\text{oef}} > \tau_s \end{cases} \tag{3.14}$$

where b_{oef} depends on the geometric factors β and γ as per

$$b_{\text{oef}} = \frac{\gamma\delta}{\beta} \tag{3.15}$$

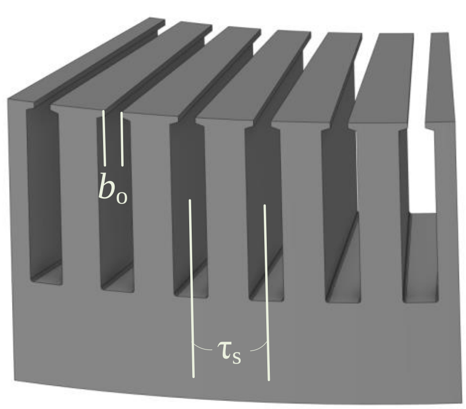

Fig. 3.3 Rectangular stator slots of the MR-AFIM. The slot pitch and slot opening are highlighted.

$$\beta = \frac{\left(1 - \frac{b_o}{2\delta} - \sqrt{1 + \left(\frac{b_o}{2\delta}\right)^2}\right)^2}{2\left(1 + \left[\frac{b_o}{2\delta} + \sqrt{1 + \left(\frac{b_o}{2\delta}\right)^2}\right]^2\right)} \tag{3.16}$$

$$\gamma = \frac{4}{\pi}\left[\frac{b_o}{2\delta}\tan^{-1}\left(\frac{b_o}{2\delta}\right) - \ln\sqrt{1 + \left(\frac{b_o}{2\delta}\right)^2}\right] \tag{3.17}$$

b_s and h_{ys}, as well as an initial k_{matrix} can be therefore determined from the above procedure. In turn, h_{s} can be initially estimated from tangential stress and current density limitations, as suggested in [60]. In addition, h_{r} can be initially sized from current density limitations, being a function of J_{s} and J_{r}:

$$h_{\mathrm{rotor}} = \frac{J_{\mathrm{s}}}{J_{\mathrm{r}}} \cdot \frac{4 b_s h_{\mathrm{s}} N Q_{\mathrm{s}} N_{\mathrm{l}} k_{\mathrm{fill}} \cos\phi}{p(D_{\mathrm{o}} - D_{\mathrm{i}})(1 - k_{\mathrm{matrix}})} \tag{3.18}$$

where $\cos\phi$ is the estimated power factor of the machine, and N is defined from V_{ph}, k_{w1} and $\hat{\phi}_{\delta\mathrm{pole}}$ as per

$$N = \frac{\xi V_{\mathrm{ph}}}{\pi\sqrt{2} f k_{\mathrm{w1}} \hat{\phi}_{\delta\mathrm{pole}}}, \tag{3.19}$$

In turn, k_{w1} is given by:

$$k_{w1} = k_{s1} k_{d1} k_{p1}, \tag{3.20}$$

In summary, the pre-sizing of the AF-MRIM begins with specific dimensional constraints (outer and inner diameter) and a target operating speed, which determine the number of poles and stator slots. Utilizing recommended air-gap flux density values, the magnetic flux per pole can be obtained using (3.2), equating it to the flux passing through the stator teeth and stator yoke (3.3). Next, predefined tooth flux density values dictate the maximum slot width and minimum stator yoke dimensions. Objective torque, and recommendations for maximum tangential stress and maximum current density are used to determine the stator slot and rotor heights. Winding turns are calculated based on the available supply voltage. Finally, it is recommended to minimize the airgap length and maintain a rotor iron proportion close to that prescribed in (3.12).

3.2.1 Considerations on the iron wire diameter

One crucial aspect in designing MR-AFIMs is determining the dimensions of the rotor copper-iron matrix structure. As stated in (3.10) and (3.12), the parameter k_{matrix} plays a key role in configuring the saturation of the rotor iron wires. Nonetheless, with a fixed k_{matrix} value, different D_{fe} and d_{fe} values can be chosen (refer to (3.10)). Theoretically, the diameter of the iron wires influences the establishment of current paths within the rotor structure, hence directly impacting torque generation. Given that iron has a significantly lower conductivity than copper, the iron wires act as high-resistance paths. Consequently, rotor currents will mostly flow through the copper structure, while the iron wires impede the ideal current paths, as illustrated in Fig. 3.4. When larger D_{fe} values are considered (as depicted on the right side of Fig. 3.4), the actual current paths deviate more from the ideal paths, and several areas of the rotor's ferromagnetic material will not be enclosed by circulating currents. In these regions, flux density does not contribute to torque generation, consequently decreasing the machine performance.

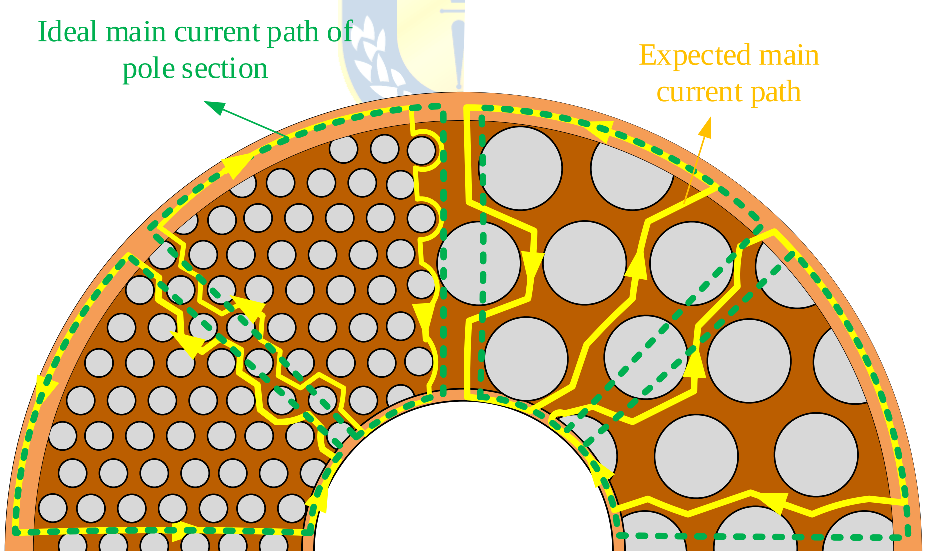

Fig. 3.4 Sketch of the expected main current path depending on the rotor iron wire diameter.

Therefore, it is advisable to opt for smaller values of D_{fe} to facilitate unrestricted circulation of rotor currents and maximize the utilization of magnetic flux density through the rotor structure. Nevertheless, manufacturing limitations and tolerances can be faced when very small D_{fe} are adopted, which should be considered as a trade-off in the design stage of MRIMs.

3.3. Validation of pre-sizing methodology

In this section, the sizing methodology described in Section 3.2 is validated using FE simulations and experimental testing. To this end, a 20 HP AF-MRIM is sized and assessed.

3.3.1 Pre-sizing a 20 HP MRIM: Main data

Following the proposed sizing methodology and based on the requirements outlined in Table 3.1, a case study is presented with a 72-slot 24-pole machine. The machine is designed for an operational speed of ~250 rpm when directly connected to a 50 Hz power supply. A DL-DW was chosen due to its advantages in heat dissipation and minimizing low spatial harmonic of the winding magneto-motive force (MMF) distribution. The main data of the machine are presented in Table 3.2.

Table 3.1 Initial parameters/requirements of a MRIM study case

Symbol	Variable	Value	Unit
D_{o}	Outer diameter	600	mm
D_{i}	Inner diameter	400	mm
N_{m}	Rotor synchronous speed	250	RPM
δ	Airgap length	2 x 1.5	mm
D_{fe}	Iron wire diameter	3	mm
P_r	Rated power	20	HP
J_{s}	Stator current density	3	A/mm2

Table 3.2 Data of the initially sized AF-MRIM

Symbol	Variable	Value	Unit
Q_{s}	Number of slots per stator	72	-
p	Number of pole pairs	12	-
h_{r}	Rotor axial length	67.5	mm
h_{ys}	Height of stator yoke	38	mm
k_{matrix}	Rotor iron proportion	0.45	-
b_{s}	Slot width	12	mm
h_{s}	Slot height	60	mm

3.3.2 Pre-sizing a 20 HP MRIM: Evaluation of design recommendations

To assess the performance of the initial AF-MRIM design, the FE method was employed using the commercial software package ANSYS Electronics Desktop. A 3D model of the machine was created, depicted in Fig. 3.5(a). A tetrahedral mesh with high density in the airgap and the rotor iron/cupper matrix was generated, as shown in Fig. 3.5(b), as the major interest in this thesis focuses on the rotor structure and its electromagnetic response. The periodicity of the machine was exploited to reduce computational load, resulting in a mesh of 1.2 million tetrahedra for the two-pole section presented in Fig. 3.5. To obtain stable-state performance indicators, slip/speed was set as an input parameter, and simulations were conducted over 1000 ms with a step size of 0.5 ms. Stator coil and rotor copper conductivities were adjusted to an operating temperature of 80 °C. Evaluating this model required 60GB of RAM when using a direct solver, such as the MUMPS, and the evaluation of stable-state performance indicators required 15 hours per slip value when using a high-end desktop 32-core computer.

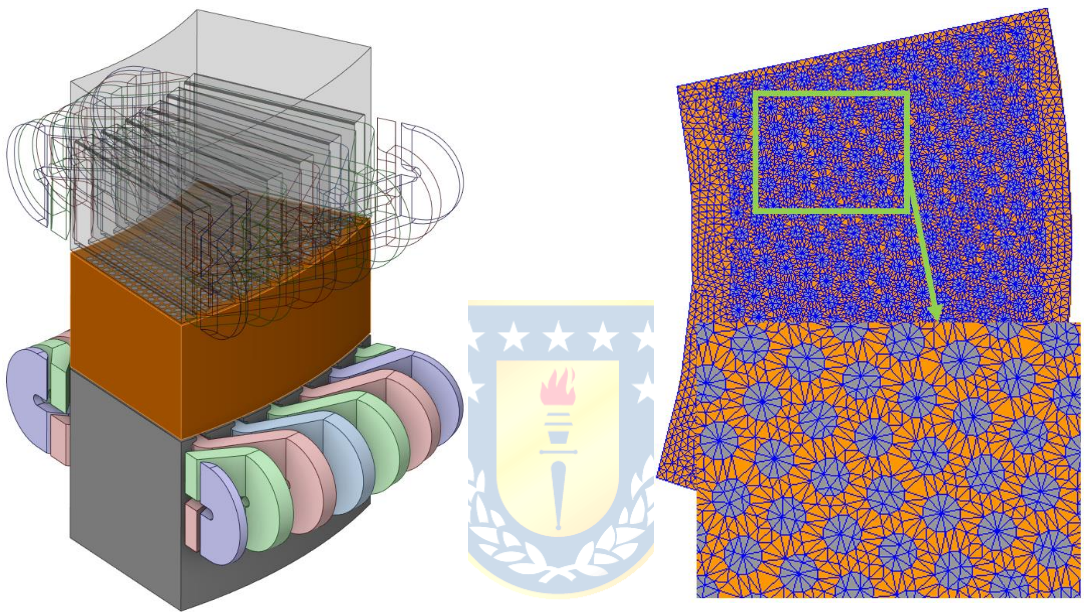

(a) (b)

Fig. 3.5 3D FE model used for the evaluation of an AF-MRIM.
(a) A two-pole section of the machine is modeled to take advantage of the machine periodicity; (b) a dense mesh is considered in the rotor iron/copper structure.

Two main suggestions were addressed in Section 3.2 for designing an AF-MRIM: i) minimizing D_{fe} to facilitate free current circulation in the rotor copper structure; and ii) ensuring k_{matrix} aligns with (3.12). In order to evaluate the first suggestion, Fig. 3.6 compares current paths for two different D_{fe} values (7 and 20 mm). In Fig. 3.6(a), it is evident that adopting a smaller D_{fe} results in current paths that closely approximate the theoretically ideal configuration (refer to Fig. 3.4): predominantly radial in the iron/copper structure and tangential in the short-circuit rings. Furthermore, with a lower D_{fe}, the current paths ensure most iron wires are adequately enclosed by current, enhancing torque capacity. This is demonstrated as the rotor with 7 mm iron wires exhibits a 23% higher mean torque compared to the 20 mm case.

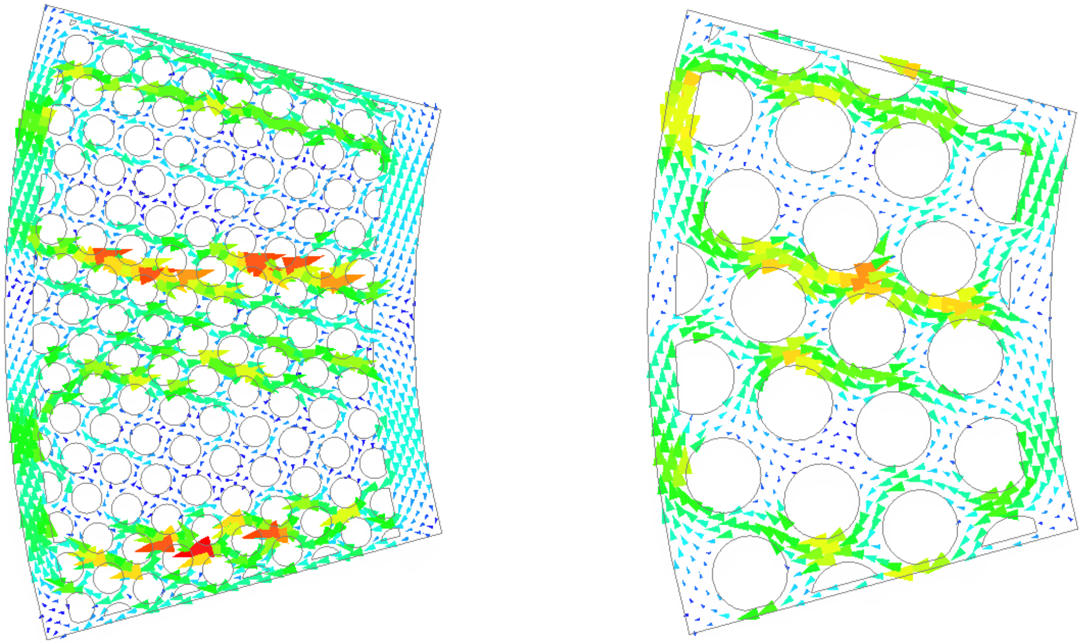

(a) (b)

Fig. 3.6 Comparison of the current density distribution across the cross-sectional area of the matrix rotor with the same k_{matrix} but varying iron wire diameters.

(a) Iron wires have a diameter of 7 mm; (b) Iron wires have a diameter of 20 mm.

Addressing the k_{matrix} recommendation provided in Section 3.2, Fig. 3.7 presents the relative maximum torque and efficiency of the proposed AF-MRIM for different values of k_{matrix}, obtained using 3D FEA. The analysis covered 16 slip values ranging from 0 to 1. Fixed values of D_{fe} and h_{r} from Table 3.1 and Table 3.2 were maintained to isolate the effect of varying k_{matrix}.

As per (3.12), the suggested value of k_{matrix} for the initially sized AF-MRIM is approximately 0.45, considering stator dimensions and geometric factors. This suggested value is denoted by a vertical green line in Fig. 3.7. The figure also includes a visual representation of three k_{matrix} values: extreme values (0.1 and 0.9) and the suggested value (0.45). In addition, 1 p.u represents the maximum torque and maximum efficiency that were found for the entire simulation set.

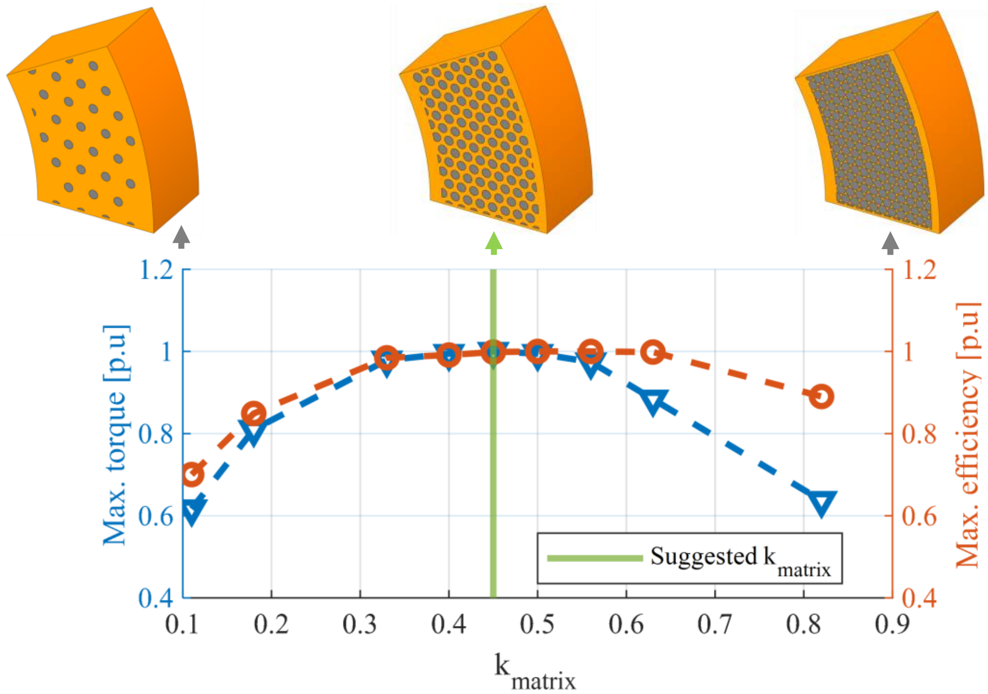

Fig. 3.7 Relative torque and efficiency of the proposed AF-MRIM as a function of k_{matrix}.

From Fig. 3.7, it can be noted that extreme values of k_{matrix} adversely affect the torque and efficiency of the machine, with best performance observed near the suggested vale (0.45). Choosing higher k_{matrix} values might appear beneficial as they reduce the magnetic load on the iron wires, potentially maintaining torque capacity. However, increasing k_{matrix} further raises rotor current density, leading to higher thermal losses. Conversely, lower k_{matrix} values decrease rotor current density but increase iron wire saturation, reducing the leakage-restriction effect and torque capacity. It is therefore recommended to start with a k_{matrix} value close to (3.12) as a design guideline, depending on manufacturing feasibility, to achieve a good torque and efficiency for the AF-MRIM.

3.3.3 Pre-sizing a 20 HP MRIM: Evaluation and validation of electromagnetic performance

In Fig. 3.8, relevant performance indicators of the proposed AF-MRIM are presented, obtained using 3D FE simulations. Since low-voltage industrial direct-drive is desired, two line-to-line voltage values were applied: 220V@50Hz and 380V@50Hz, emulating star and delta connections.

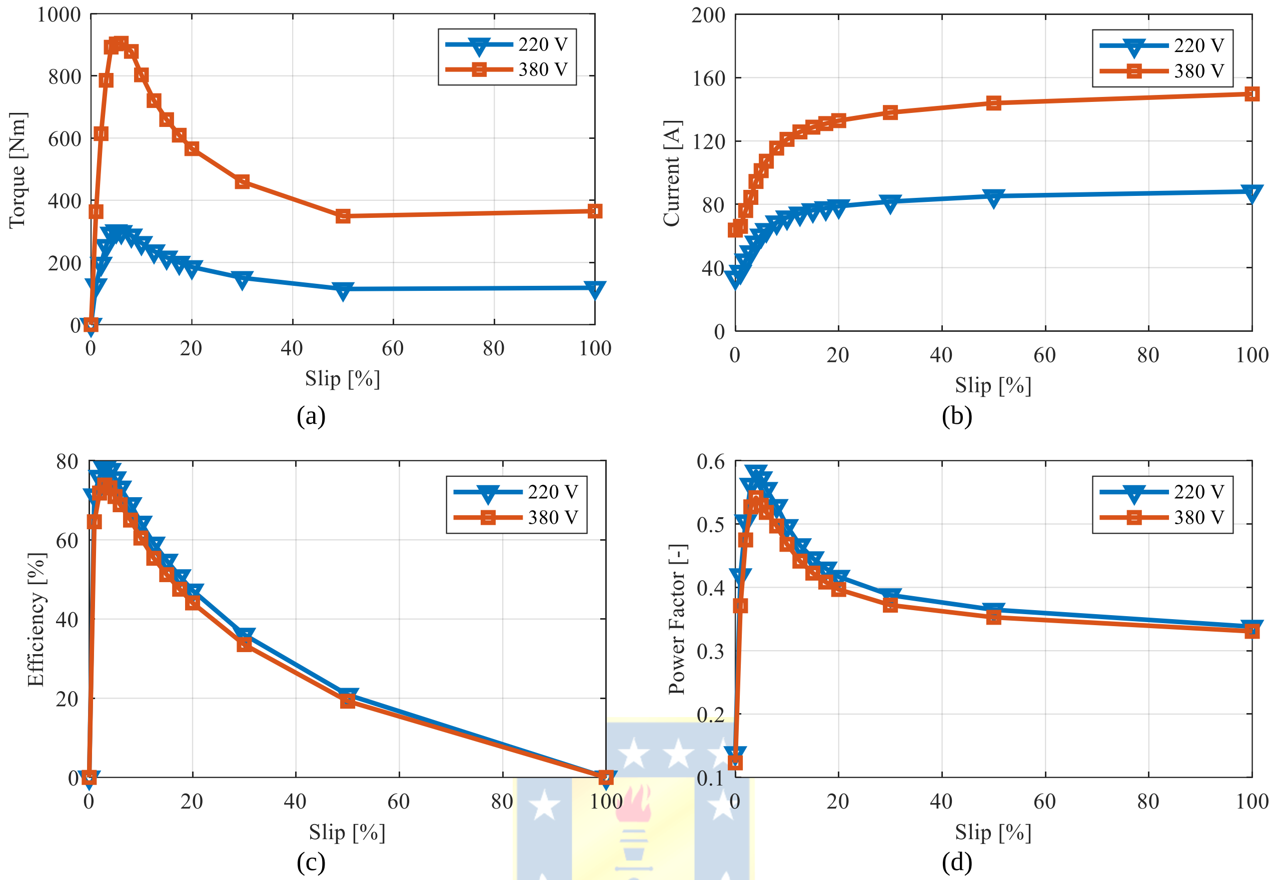

Fig. 3.8 Electromagnetic response of the AF-MRIM considering motor slip values at different voltage levels
(a) Electromagnetic torque. (b) RMS value of stator line current. (c) Efficiency. (d) Power factor.

Average torque, efficiency, stator current and power factor were analyzed for 16 different slip values during motor mode operation. Referring to Fig. 3.8(a), the objective torque is achieved at 2% slip with a supply voltage of 380 V, resulting in an output power of 20 HP at 245 rpm. Additionally, the maximum torque peaks at 920 Nm under 380 V supply, decreasing to approximately 310 Nm under 220 V supply. Maximum torque is roughly twice the starting torque, and the machine exhibits a narrow stable speed range in both cases, demonstrating robust speed response. Variations in load torque have minimal impact on speed stability. Fig. 3.8(b) illustrates that stator line current ranges from 34 to 88 A with a 220 V supply, and from 64 to 150A with a 380 V supply. The starting current of the AF-MRIM, which is twice the current during low-slip operations, contrasts favorably with traditional SCIM that can have starting currents 5-7 times their rated values. This underscores the suitability of the AF-MRIM for direct-drive applications. Efficiency and power factor, depicted in Fig. 3.8(c) and Fig. 3.8(d) respectively, show comparable trends for both 220 V and 380 V operating scenarios. Efficiency exceeds 60% across most of the linear zone for slip values between 1 and 10%, peaking at approximately 75% around 3% slip. Considering the topology, high pole count, low speed, and direct drive operation, these efficiency values are within expectations. In turn, maximum power factor is around 0.55 for both voltage supplies, although a slight decrease is observed with the 380 V supply due to the increased saturation of the rotor iron wires, leading to higher flux leakage in the iron-copper matrix.

In these simulations, iron wire losses were disregarded due to the complexities involved in their calculation and their scarce effect on machine performance. Iron loss calculation is a challenging task unless precise laminations and consistent manufacturer data is available, and its calculation on the matrix rotor arrangement is a challenging task. According to classic methods for iron loss computation [61], these losses depend on the flux density peak value and frequency, and specific coefficients are required for each source of iron loss. These coefficients are typically determined experimentally and are provided in tables for specific frequencies, usually starting from 50 Hz. Considering the operational conditions of the proposed MRIM, the frequency of rotor currents and the relative frequency at which flux density circulates through the matrix rotor are low. The rated slip was below 2%, and the overload slip was around 5%. Comparatively, other conventional IM designs operate below 5% rated slip, depending on specific design characteristics. Consequently, the frequency of rotor currents is approximately 2-4% of the power supply frequency, which for the proposed MRIM design is 50 Hz. Given a rated slip of 1.8%, the frequency of induced currents in the rotor is less than 1 Hz. Additionally, rotor copper losses are significantly higher and a significant factor in efficiency reduction, reason why the calculation of iron losses in the matrix rotor may be neglected during the initial machine sizing. In order to partially validate this approach, FE simulations were carried out with solid non-laminated iron wires incorporating eddy current losses computation. The results were compared with simulations where iron losses were not considered in the wires, revealing differences of less than 2% in all cases and no significant efficiency penalty from neglecting iron losses. Nevertheless, if a higher supply frequency is considered, different operating conditions are anticipated, or further refinement of the design approach is desired, considering iron losses as part of an optimization process could be advised.

3.3.4 Pre-sizing a 20 HP MRIM: Experimental validation of electromagnetic performance

Based on the dimensions and design considerations explained earlier, a 20 HP prototype was tested, depicted in the exploded view in Fig. 3.9. The stator core utilizes M400-50A electrical steel, while 1020 steel was chosen for the iron wires. The mechanical design of the motor included the shaft and case design to withstand fatigue and high cyclic loads. The shaft was constructed from SAE4340 steel, and the case was made of aluminum alloy C355 for its advantageous properties such low weight, high thermal conductivity, and good mechanical strength. Steel inserts were incorporated into the aluminum parts to enhance structural rigidity. Tapered rolling bearings were utilized to support the shaft and maintain rotor alignment.

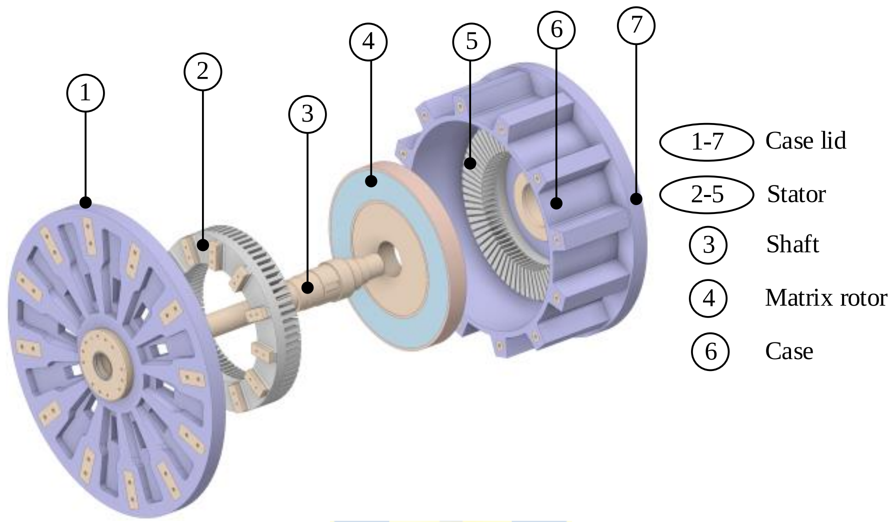

Fig. 3.9 Exploded view of the AF-MRIM. The mechanical parts of the machine are listed for clarity.

The rotor manufacturing process followed a four-step technique akin to the method used for NbTi superconductors. Initially, the Fe-Cu assembly involved packaging hexagonal copper rods and hexagonal copper tubes filled with low-carbon steel wires, which were joined to create a copper cylinder. The second step included isostatic pressing of the assembly after prior stretching to enhance cohesion between the copper hexagons. The process considered heating to 400° C and isostatic pressing at 150 MPa helium. Subsequently, the third step heated the Fe-Cu assembly to 800° C, subjected it to slow-speed pressure stretching, achieving an area reduction ratio of 3.3. The resulting stretched cylinder initially measured 278 mm in diameter. Finally, the pressure-drawn bar was machined flat on two sides and divided into uniform segments. These segments were then soldered together side by side using a silver alloy. The manufacturing process was conducted in the Outokumpu Copper Research & Development Metal Laboratory, Finland, whilst the assembly of the machine was carried out in facilities of the University of Concepcion, Chile. The resulting rotor and stators, adhering to the dimensions specified in Table 3.1 and Table 3.2, are shown in Fig. 3.10.

(a) (b) (c)

Fig. 3.10 Manufactured parts of the AF-MRIM prototype.
(a) Stator and winding. (b) Rotor and shaft. (c) Anisotropic matrix rotor

The test bench, depicted in Fig. 3.11, comprises a dynamometer, a control unit and a monitoring unit. The dynamometer features an 8-pole 45-kW IM coupled with an ABB ACS800-11 55-kW converter operating in regenerative mode to simulate mechanical loads. The control and monitoring units include a Danfoss FC 302 55-kW converter connected to the AF-MRIM in order to control the operation of the motor. Load tests were conducted using U/f control at different voltage levels and constant frequency. Voltage and current measurements were taken using Yokogawa voltage probes and Tektronix A621 current sensors, connected to a Yokogawa WT1806E power analyzer. Torque and speed measurements were estimated by the ABB converter, with these signals processed in the power analyzer. Additionally, a Yokogawa DL850 oscilloscope and Yokogawa voltage probes were used to register winding line-to-line voltage during testing

.

Fig. 3.11 Test bench and equipment used to operate the AF-MRIM prototype.

Fig. 3.12 compares relevant performance metrics obtained by FE evaluating the initial AF-MRIM design with experimental measurements. Average torque, efficiency, stator current and power factor were obtained using the experimental test bench presented in Fig. 3.11. The machine was operated below 3% slip to stay within thermal limits.

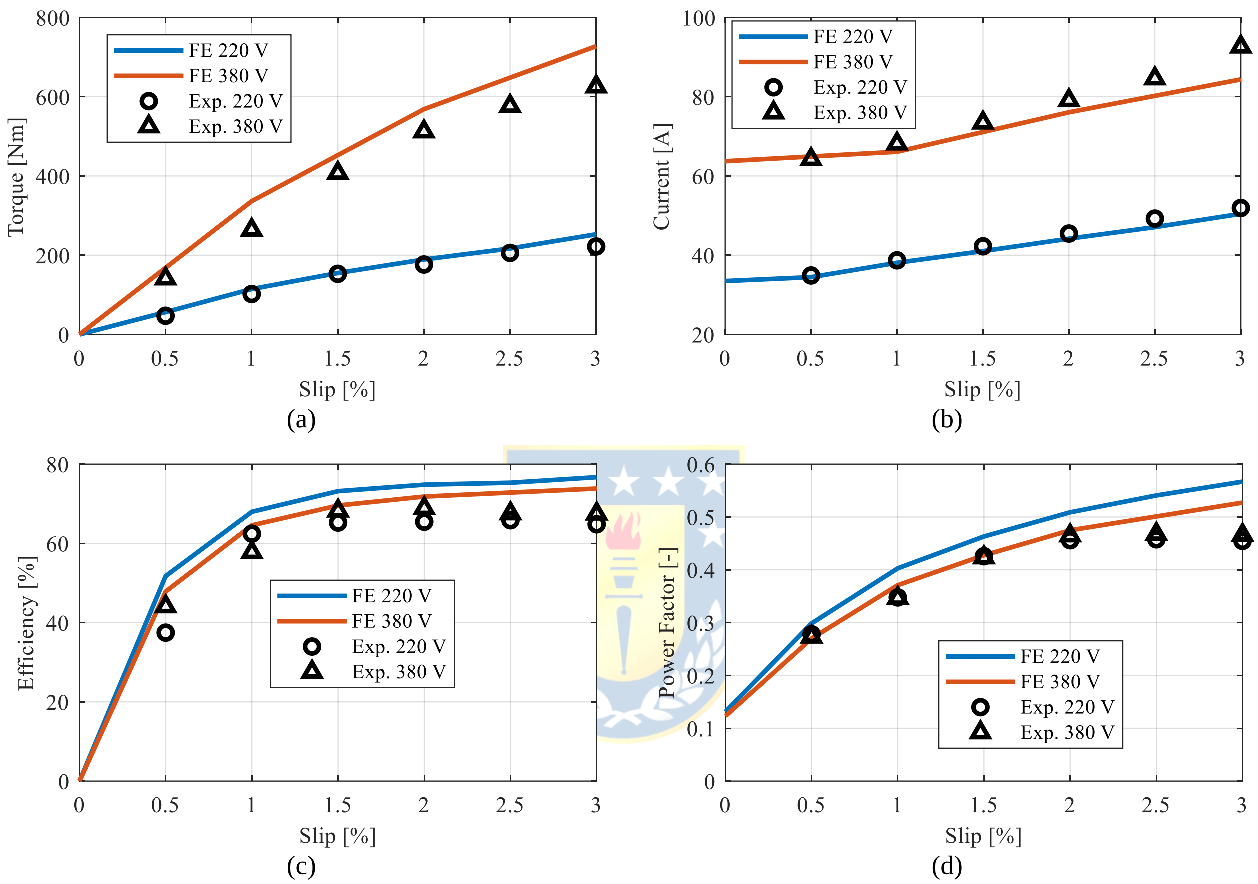

Fig. 3.12 Comparison of FE and experimental results of the MR-AFIM at different voltage levels.
(a) Electromagnetic torque; (b) Phase RMS current; (c) Efficiency; (d) Power factor

Temperature readings were captured using a Fluke TiS55 infrared thermographic camera during operation at 2.0% slip, revealing temperatures below 75 °C at the end-winding area and rotor inner surface when connected to a 380 V voltage source, indicating feasible continuous operation. As it can be seen from Fig. 3.12, there was good agreement between experimental data and FE results: the constructed machine achieved up to 540 Nm at 245 rpm in direct-drive operation at 380 V, 50 Hz, meeting the target torque and output power. A very precise estimation was observed for the 220 V case, owing to low machine saturation within the speed range considered. For the 380 V case, a slightly higher estimation error was observed in slip-torque and slip-current characteristics due to increased saturation, potential variations in leakage inductance calculations, as well as manufacturing and assembly tolerances. Nevertheless, the FE model effectively predicted machine performance, validating both the proof of concept and the sizing methodology.

3.4. Optimizing AF-MRIM: Progressive model simplification (PMS)

Section 3.3 validated a 3D FE model through experimental testing, establishing it as a foundational tool for evaluating various MRIM designs. However, due to its impractical computational burden (exceeding 24 hours per MRIM design), it is not recommended for optimization or large-scale analysis ends. To address this challenge, a progressive model simplification (PMS) methodology is proposed in this thesis to allow faster MRIM optimization, at the cost of decreasing overall accuracy.

3.4.1 PMS methodology: assumptions and details

The proposed PMS simplification involves transitioning from a detailed 3D model to a simplified approach using both 3D and 2D representations of an AF-MRIM, This is achieved by simplifying the rotor's magnetic and electric response to an anisotropic material with an equivalent BH curve. In this regard, and assuming the MRIM has low-diameter iron-wires as recommended in Section 3.2.1, the following considerations apply:

- The magnetic characteristics of the iron-copper matrix are represented by an equivalent anisotropic structure with a z-axis permeability derived from a converted BH curve, while other components retain the permeability of free space.
- The electric properties of the iron-copper matrix can be simplified to a uniform structure with conductivity reduced relative to copper.

Fig. 3.13 illustrates this PMS process: starting with the validated full model in Fig. 3.13(a), which is then simplified by replacing the rotor matrix structure with an anisotropic material exhibiting equivalent magnetic and electric behavior in Fig. 3.13(b). Subsequently, the simplified 3D model is segmented into three slices, as depicted in Fig. 3.13(c) and these slices are converted into 2D linear models for efficient evaluation. Mild saturation can be assessed, since the evaluation of the machine performance is conducted by means of FE simulations.

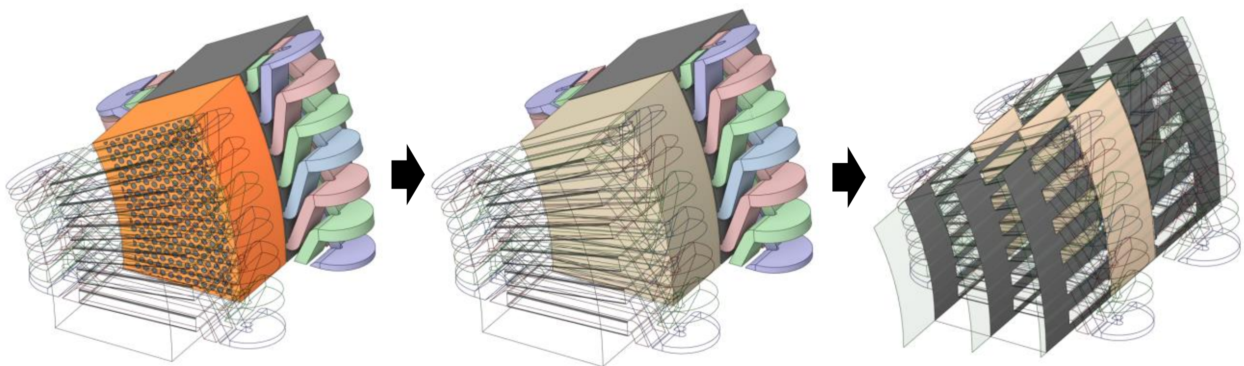

(a) (b) (c)

Fig. 3.13 Progressive model simplification to quickly evaluate the performance of an AF-MRIM.
(a) Two pole sections of the full model, capturing the precise magnetic and electric characteristics of the machine. (b) Rotor matrix structure is replaced by an equivalent material, with converted magnetic and electric properties. (c) Three slices of the MRIM are extracted to enable a linear 2D assessment.

The BH curve of the equivalent rotor is obtained by adjusting the material's permeability. In the original matrix structure, the cross-sectional area of the ferromagnetic material of one rotor pole is defined as:

$$A_{\mathrm{fe,r}} = \pi\left(\frac{{D_o}^2 - {D_i}^2}{8p}\right)\cdot k_{\mathrm{matrix}} \tag{3.21}$$

In contrast, in the equivalent rotor, the cross-sectional area of one rotor pole is

$$A_{\mathrm{fe,r}} = \pi\left(\frac{{D_o}^2 - {D_i}^2}{8p}\right) \tag{3.22}$$

Since the rotor magnetic flux must be conserved between the original matrix structure and the equivalent rotor, the following condition from (3.4) should be considered:

$$\hat{B}_{\mathrm{rotor,eq}} \cong \hat{B}_{\mathrm{rotor,original}}\cdot k_{\mathrm{matrix}} \tag{3.23}$$

Therefore, under the same stator current excitation and given magnetic field intensity in [A/m], the material exhibits have a different flux density response, which is adjusted based on the BH curve. To proceed with the second step of the PMS, the material's permeability (μ_{PMS}) is calculated by means as follows:

$$\mu_{\mathrm{PMS}}(|\vec{H}|) \cong (\mu_{\mathrm{original}}(|\vec{H}|) - \mu_0) \cdot k_{\mathrm{matrix}} + \mu_0. \tag{3.24}$$

Here, μ_{original} represents the magnetic permeability of the ferromagnetic material used in the iron wires of the original matrix structure.

The electrical conductivity of the equivalent rotor structure is estimated by taking into account the ratio between the original copper area of the main current path (adjusted for the presence of iron wires), and the area of the main current path in the new uniform material. This is given by:

$$\sigma_{\mathrm{PMS}} \cong \sigma_{\mathrm{original}} \cdot (1 - k_{\mathrm{matrix}}) \tag{3.25}$$

Additionally, since the variable reluctance paths present on the surface of the original matrix rotor structure are absent in the equivalent rotor, adjustments to the airgap of the machine are necessary using the rotor Carter factor.

Once the 3D equivalent model is devised following the above considerations, three slices of the model can be extracted for assessing machine performance through 2D analysis. While a single slice at the mean radius could be used for this purpose, significant errors could arise from neglecting phenomena at the inner and outer radii, which are partially addressed by the triple-slice methodology. End-winding inductance can be estimated using methods outlined in [59],[62] and must be incorporated into the 2D simulation. Additionally, the periodicity of the machine can also be exploited in the 2D model to reduce computational load.

3.4.2 PMS trade-off: low computation burden at the cost of slightly lower accuracy

To demonstrate the computational efficiency and accuracy impact of the PMS, the initial MRIM design introduced in Section 3.3.2 is assessed using three different modeling approaches: the full 3D model, the equivalent 3D model, and the triple-slice 2D linear model. The comparison results at 380V are presented in Fig. 3.14, showcasing torque, power factor, efficiency and current density characteristics. A summary of the comparison for relevant performance indicators at 380V is presented in Table 3.3, covering starting and rated conditions, as well as maximum values.

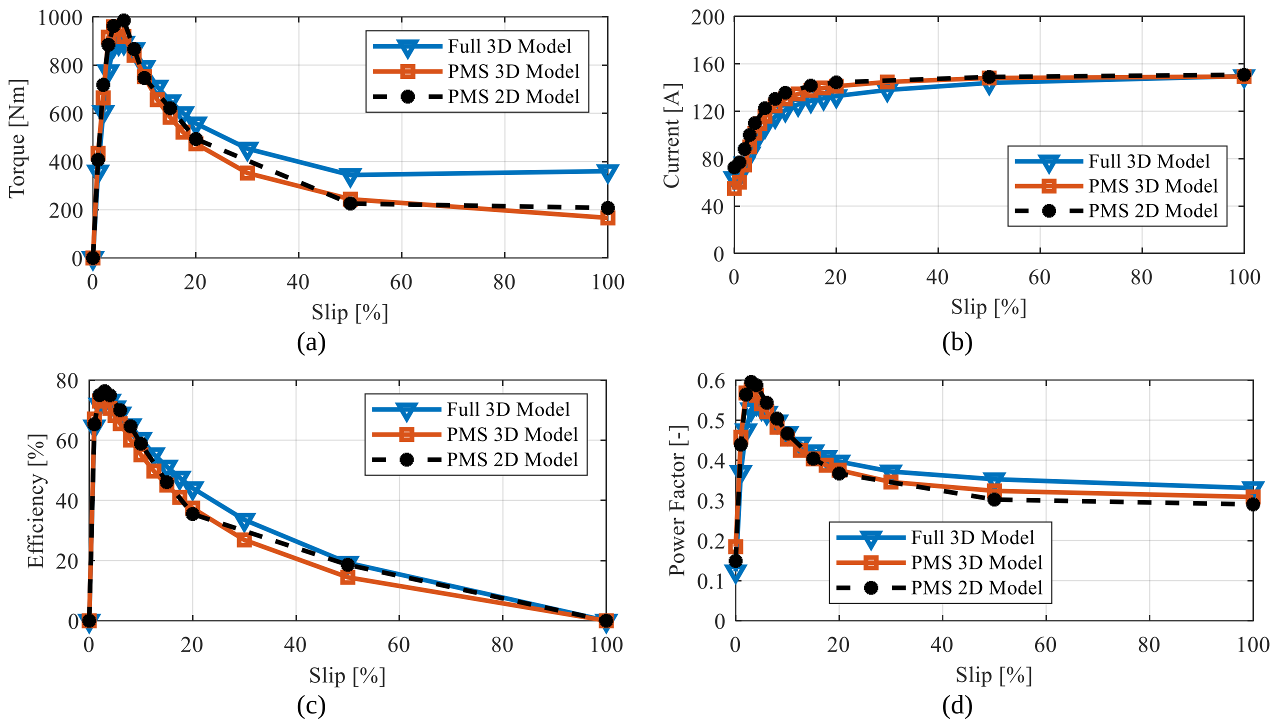

Fig. 3.14 Comparison of the electromagnetic behavior of the MR-AFIM obtained by means of different stages of the PMS, from the detailed full 3D model down to the simplified triple-slice 2D model.
(a) Electromagnetic torque. (b) RMS value of stator line current. (c) Efficiency. (d) Power factor.

Table 3.3 Comparison of performance estimation over the initially sized MRIM

Symbol	Variable	Full 3D model	PMS 3D model	PMS 2D model
T_{r}	Rated torque	588 Nm	628 Nm	712 Nm
η_{r}	Rated efficiency	71.2%	72.9%	75.0%
$\cos\phi_r$	Rated power factor	0.48	0.53	0.56
$I_{\mathrm{L,r}}$	Rated line current	76.1 A	75.8 A	86.1 A
T_{max}	Max. torque	919 Nm	962 Nm	998 Nm
$\cos\phi_{\mathrm{max}}$	Max. power factor	0.55	0.58	0.60
η_{max}	Max. efficiency	73.8%	74.2%	76.3%
$I_{\mathrm{L,max}}$	Max phase current	149.7 A	151.0 A	156.0 A
T_{stall}	Stall torque	365 Nm	174 Nm	201 Nm
$t_{\mathrm{simulation}}$	Simulation time	4296 min	581 min	12 min

Based on Fig. 3.14 and Table 3.3, the PMS 3D stage demonstrates strong agreement with the full 3D model in torque, current and efficiency responses during low-slip operation. Specifically, the differences in accuracy between the full 3D model and the PMS 3D model were less than 8% for torque, 2% for efficiency and current, and 7% for power factor calculations. This close correspondence stems from consistent current paths and electric response in the rotor structure, with negligible iron losses in the matrix rotor under these operational conditions. In turn, the accuracy differences between the full 3D model and the 2D PMS model were within 25% for torque, and 14% and 7% for current and efficiency estimation, respectively, with a 10% discrepancy in power factor calculations. As expected, the 2D model tends to slightly overestimate machine performance, while the 3D model provides a more accurate representation. Both simplified models, nonetheless, correctly capture the shape of the slip characteristic curves. In contrast, it is important to note that the PMS method des not accurately estimate stall torque, as it assumes conditions that do not hold during startup, such as high iron losses, the relevance of the iron/copper structure and patterns of iron wires at high-slip operations. Nevertheless, both the 3D and 2D PMS models should be suitable for accurately estimating the low-slip performance of an AF-MRIM, facilitating optimization and other analyses at larger scale.

In order to complement the FE validation, three additional AF-MRIM designs with 12 and 24 poles were developed using general sizing equations and assessed using the PMS method. Main data of the machines are summarized in Table 3.4. Table 3.5 presents the performance of these designs obtained by the different proposed methods, showcasing good agreement between full 3D FE simulations and PMS results.

Table 3.4 Main data of the AF-MRIM specimens devised to validate the accuracy of the PMS

Symbol	Variable	M#2	M#3	M#4	Unit
D_{o}	Outer diameter	520.0	702.0	310	mm
D_{i}	Inner diameter	300.0	478.0	180	mm
δ	Airgap length	1.2	2.0	1.0	mm
D_{fe}	Iron wire diameter	5	5	2.5	mm
V_{LL}	Line-to-line voltage	220	380	220	V
J_s	Stator current density	5	3	5	A/mm^2
P_r	Rated power	6	85	1	HP
Q_{s}	Number of stator slots	72	72	54	-
n_{cond}	Number of conductors per slot layer	9	5	32	-
p	Number of pole pairs	12	6	6	-
l_{r}	Rotor axial length	40.0	50.0	20.0	mm
h_{ys}	Height of stator yoke	20.0	26.2	14.4	mm
k_{matrix}	Rotor iron proportion	0.5	0.46	0.56	-
b_{s}	Slot width	8.0	13.3	6.6	mm
h_{s}	Slot height	30.0	45.8	13.6	mm
-	Overall volume	0.031	0.078	0.006	m^3

Table 3.5 Comparison of performance estimation tools for different AF-MRIM designs

Machine	Quantity	Full 3D	PMS 3D	PMS 2D
24-pole M#2	T_{r}	234.4 Nm	238.7 Nm	252.5 Nm
	η_{r}	63.8%	64.8%	66.4 %
	$\cos\phi_r$	0.53	0.55	0.54
	$I_{\mathrm{L,r}}$	62.3 A	61.9 A	66.8 A
12-pole M#3	T_{r}	1268.2 Nm	1322.1 Nm	1410.9 Nm
	η_{r}	88.1%	88.9%	90.7 %
	$\cos\phi_r$	0.77	0.78	0.81
	$I_{\mathrm{L,r}}$	174.0 A	179.4 A	188.2 A
12-pole M#4	T_{r}	15.2 Nm	14.7 Nm	16.0 Nm
	η_{r}	72.8 %	71.9%	74.3%
	$\cos\phi_r$	0.70	0.68	0.74
	$I_{\mathrm{L,r}}$	6.6 A	6.8 A	6.5 A

In summary, the PMS proved to be suitable for a correct evaluation of rated operation, reducing computational burden in an 87% for the 3D PMS model, and 99.7% for the 2D PMS model. This enables large-scale assessments in AF-MRIMs, as verified below.

3.4.3 PMS applicability example: MRIM optimization

In this section, the initially sized MRIM undergoes design optimization to maximize power and torque capacity while adhering to current density limits and volume constraints. The rated current density must not exceed 3 A/mm^2, and the volume of the machine's active parts must be $\leq$ 0.077 m^3, based on the original pre-sized dimensions. Three 2D linear models were integrated using ANSYS Workbench with embedded ANSYS Electronics simulations. The final performance indicators were determined by averaging results across three layers of the machine, as depicted in Fig. 3.13(c). Table 3.6 summarizes the ranges set for each dimensional parameter involved in the optimization process, aimed at exploring designs around the initially sized MRIM from Section 3.3.1. Other dimensional parameters remain constant throughout the optimization. A MOGA was used to solve the optimization problem, aimed at maximizing torque capacity, efficiency and power factor, while minimizing current density at rated slip. An initial population of 100 machine specimens was considered, and the optimization search grid for dimensional parameters was set with increments of 0.1 mm, aligning with typical manufacturing tolerances found in laser cutting [43]-[73]. Fig. 3.15 displays the raw optimization data, highlighting on relevant performance indicators for each assessed specimen.

Table 3.6 Proposed optimization problem of a maximum power factor AF-MRIM

Symbol	Variable	Min. value	Pre-sized value	Max. value
l_{r}	Rotor axial length	40.0 mm	67.5 mm	90.0 mm
h_{ys}	Height of stator yoke	10.0 mm	38.0 mm	50.0 mm
k_{matrix}	Rotor iron proportion	0.35	0.45	0.55
b_{s}	Slot width	6.0 mm	12.0 mm	18.0 mm
h_{s}	Slot height	35.0 mm	60.0 mm	80.0 mm
b_{o}	Slot opening (% of b_{s})	0%	50%	100%
h_{tt1}	Tooth-tip minor height	0 mm	1.0 mm	4.0 mm
h_{tt2}	Tooth-tip major height	0 mm	2.0 mm	6.0 mm
n_{cond}	Number of conductors per slot layer	7	11	14

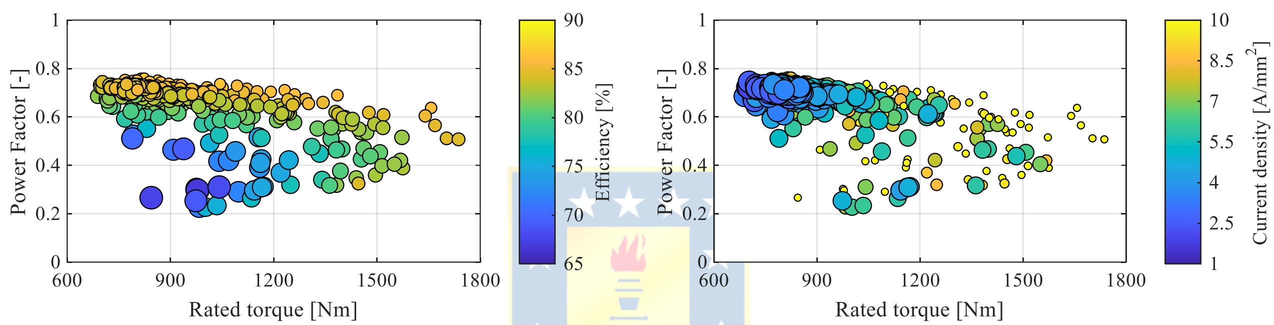

(a) (b)

Fig. 3.15 Evolution of 24-pole AF-PMSM specimens seeking maximum torque, efficiency and power factor, while minimizing current density.
(a) Torque, power factor and efficiency of each specimen is presented; (b) Torque, power factor and current density of each specimen is presented.

In Fig. 3.15, maximum power factor was observed near 0.85, with the peak rated torque reaching approximately 1500 Nm. Additionally, the highest efficiency recorded was approximately 89%, indicating a significant improvement over the initial AF-MRIM sizing. It should be noted that these findings are based on the 2D PMS, which has been shown to slightly overestimate the performance of evaluated machine prototypes. Therefore, actual performance in final designs is expected to be slightly lower, requiring validation using the full 3D model for a more accurate final assessment.

After solving the optimization problem presented in Table 3.6, best candidates were obtained after 13 iterations, with each iteration assessing 100 designs. The final design was selected by considering the trade-off between relevant performance ratings, with a particular focus on enhancing power factor. Main dimensions of the final optimized 24-pole MRIM are summarized in Table 3.7.

Table 3.7 Dimensional values of the best AF-MRIM design aiming at maximizing power factor

Symbol	Variable	Pre-sized value	Optimized value
D_o	Machine outer diameter	600.0 mm	696.2 mm
D_i	Machine inner diameter	400.0 mm	458.7 mm
l_r	Rotor axial length	67.5 mm	58.1 mm
δ	Airgap length	2 x 1.5 mm	2 x 1.5 mm
h_{ys}	Height of stator yoke	38.0 mm	19.7 mm
k_{matrix}	Rotor iron proportion	0.45	0.52
b_s	Slot width	12.0 mm	11.5 mm
h_s	Slot height	60.0 mm	46.9 mm
b_o	Slot opening (% of b_s)	50%	62%
h_{tt1}	Tooth-tip minor height	1.0 mm	0.6 mm
h_{tt2}	Tooth-tip major height	2.0 mm	1.2 mm
$V_{overall}$	Overall volume	0.077 m^3	0.076 m^3
n_{cond}	Number of conductors per slot layer	11	10

The observed reduction in slot height compared to the initial design is a direct response to the objective of minimizing leakage inductance to increase power factor. Additionally, there is a slight increase in k_{matrix}, which reflects adjustments in stator tooth/slot ratio achieved through optimization. The optimized MRIM, evaluated through the full 3D model, is compared with the initially sized MRIM in Fig. 3.16.

From Fig. 3.16 illustrates a substantial increase in torque capacity and efficiency. The maximum torque achieved by the optimized design 1.51 kNm, with efficiency peaking at 85.2% and a maximum power factor of 0.72. Moreover, the rated power of this new design is 30 HP. Efficiency at rated power has increased by 12 percentage points (from 72% to 84%), and the power factor was boosted in 18 points, reaching 0.70 at 3 A/mm^2. Current density response remains comparable between both machines at low-speed operation, whereas the optimized machine exhibits significantly higher current density at high slips. Nevertheless, the optimized MRIM, resulting from the integration of MOGA optimization with PMS tools, offers significant overall advantages over the initially sized machine. This improvement stems from the reduction in leakage flux achieved with the optimized machine, facilitated by the structural benefits and magnetic response of the matrix rotor structure.

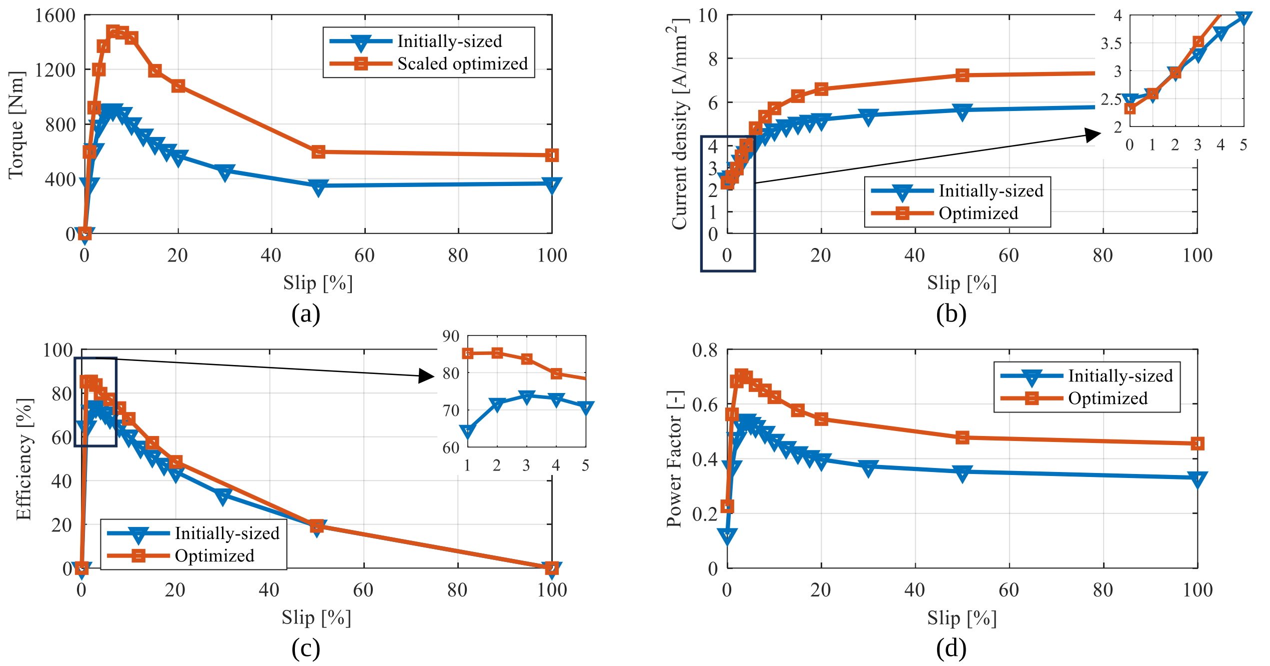

Fig. 3.16 Electromagnetic comparison of the initially-sized and the optimized AF-MRIM (evaluated by means of the full 3D model).
(a) Electromagnetic torque. (b) Current density; (c) Efficiency; (d) Power factor. It should be noted that both machines have the same overall volume.

3.5. Identification of design parameters with the most sensitiveness on AF-MRIMs

Results investigating the impact of varying design parameters on AF-MRIM performance have been preliminary obtained and published in [27]. The study utilized the FLUX 3D commercial software from Altair due to its efficiency in steady-state simulations, and two CAD models were integrated into the FLUX interface. In this thesis, the PMS 3D model is evaluated to using Ansys Electronics Desktop, yielding comparable results and consistent trends, as described below.

3.5.1 Evaluation of parameter variation by means of simplified PMS 3D model.

Fig. 3.17 presents relevant performance indices of the initially sized AF-MRIM evaluated using the PMS, with rotor height (h_r) values ranging from 50 to 84.4 mm in 5 uniform increments, covering $\pm$ 25% of the original value. The curve representing the original design is highlighted by a **thicker line** compared to other designs. Fig. 3.17(a), Fig. 3.17(b) and Fig. 3.17(c) depict the torque-slip characteristic, efficiency, and power factor respectively. The findings are summarized as follows:

I) Torque-slip characteristic:

- Increasing rotor height decreases the slip at maximum torque and slightly enhances starting torque.

II) Efficiency:

- Smaller h_r results in higher slip at maximum efficiency, consistent with the observed increase in slip at maximum torque in Fig. 3.17(a).
- Machines with smaller h_r exhibit lower efficiency at low slips but achieve higher efficiency at high slips, as shown in Fig. 3.17(b).

III) Power factor:

- The slip at maximum power factor decreases with increasing h_r, aligning with the reduction in slip at maximum torque.
- Lowering h_r results in lower power factor values at sable-state low slips.

IV) Line current:

- Increasing h_r leads to a decrease in line current across all slip values.

The variations in performance observed with changes in rotor height can be understood by examining the current path within the machine rotor: h_r directly affects the cross-sectional area through which current flows, hence altering the rotor's equivalent resistance. A decrease in h_r decreases this cross-sectional area and consequently raises rotor resistance. This change influences the slip at maximum torque, efficiency, and power factor.

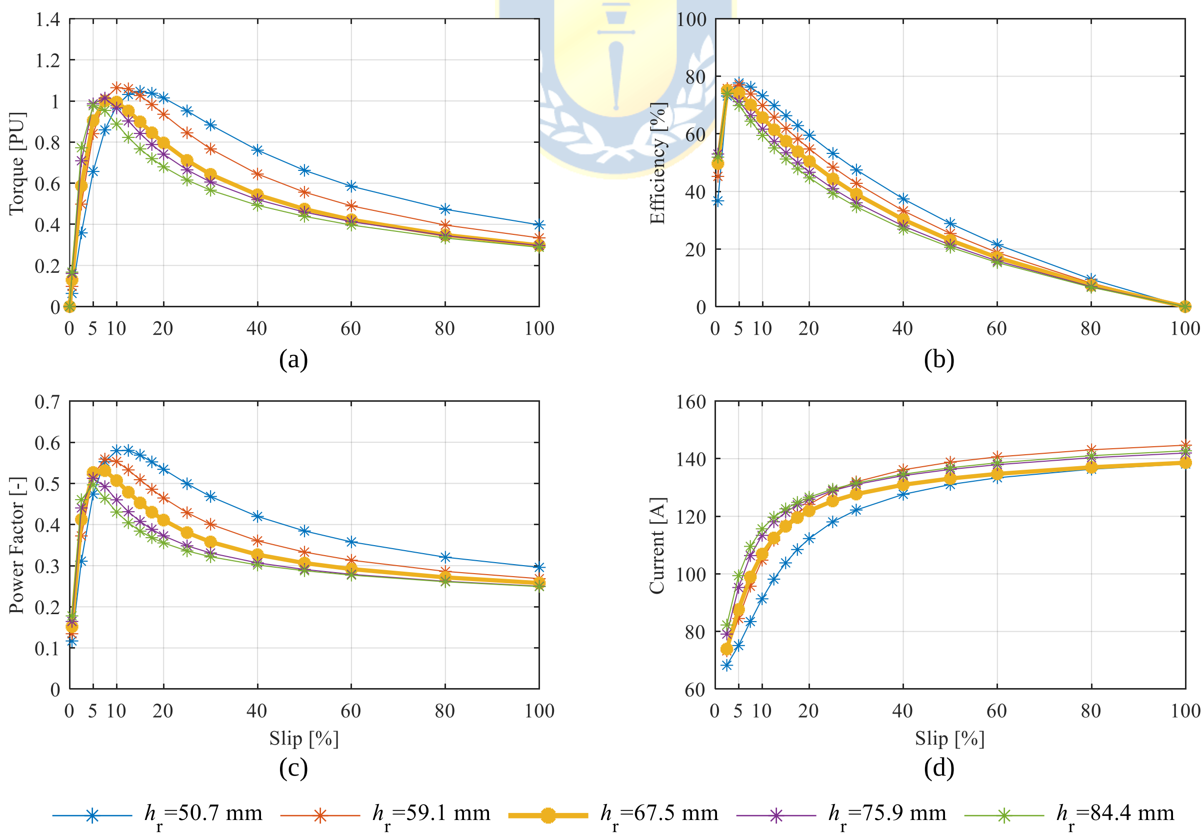

Fig. 3.17 Evaluation of AF-MRIM performance using 3D PMS model when varying rotor height (h_r).
a) Torque-slip characteristic, b) Efficiency, c) Power factor; d) Line current.

Fig. 3.18 presents the evaluation of the machine using the PMS 3D model with varying slot height (h_s) from 45 to 75 mm in 5 uniform increments, covering a $\pm$ 25% of the original value. Similar to previous evaluations, the curve representing the original design is highlighted with a **thicker line**. In Fig. 3.18(a), Fig. 3.18(b) and Fig. 3.18(c), the torque-slip characteristic, efficiency and power factor are evaluated respectively. Relevant findings include:

I) Torque-slip characteristic:

- The machine exhibits significantly higher torque as h_s decreases, attributed to reduced slot leakage inductance with shorter slots.

II) Efficiency:

- A slight reduction in efficiency is observed with increasing slot width at higher slips.

III) Power factor:

- The power factor improves across all slips from 0 to 1 as slot width decreases.

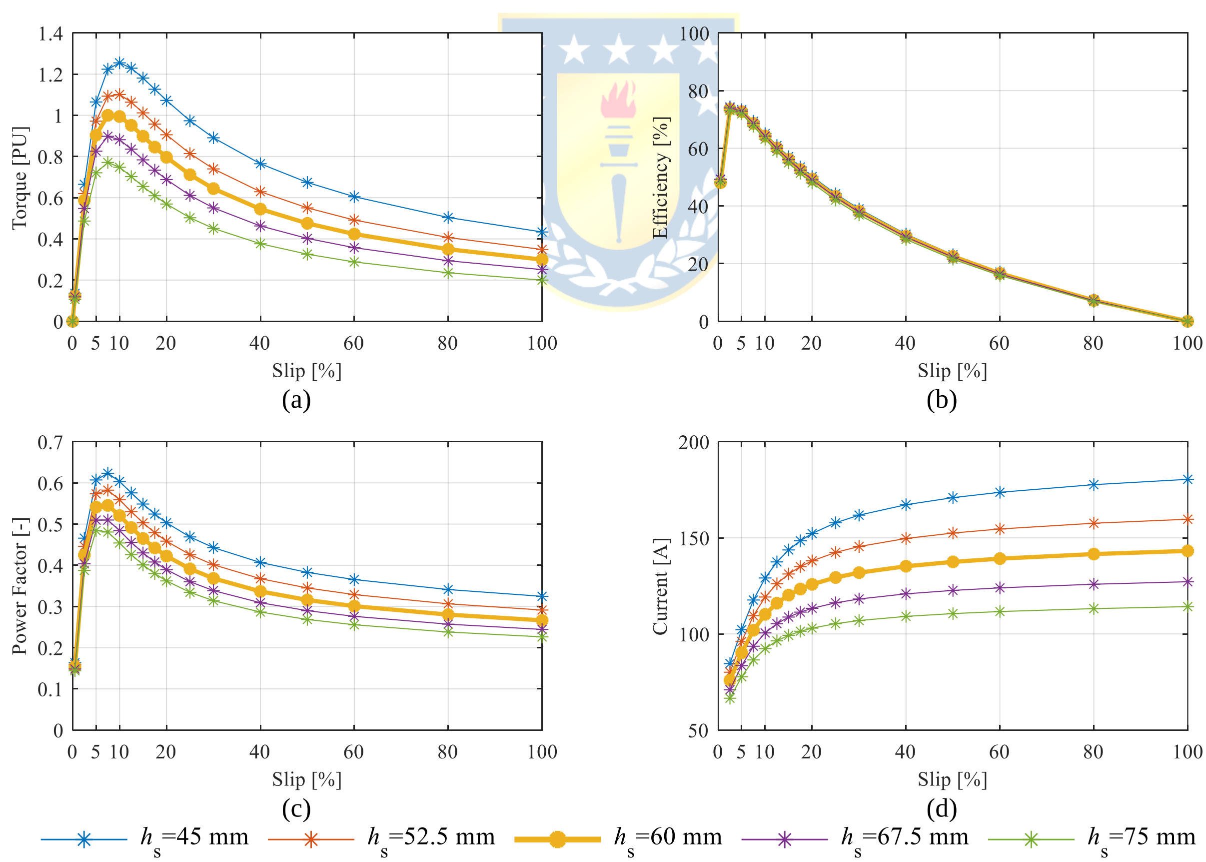

Fig. 3.18 Evaluation of AR-AFIM performance by means of the 3D PMS model when varying slot height (h_s).
a) Torque-slip characteristic, b) Efficiency, c) Power factor; d) Line current.

III) Line current:

- Line current increases for all evaluated slips as slot width decreases, due to reduced cross-sectional area of conductors. This configures a trade-off between increased torque and higher line current.

Fig. 3.19 shows relevant performance metrics of the initially sized MRIM using the PMS 3D model, examining different airgap lengths (δ) ranging from 1.1 and 1.9 mm in increments of 0.2 mm, covering $\pm$ 25% of the original value. In Fig. 3.19(a), Fig. 3.19(b) and Fig. 3.19(c), the torque-slip characteristic, efficiency, power factor and current are evaluated, respectively. The findings are summarized as follows:

I) Torque-slip characteristic:

- Maximum torque decreases with larger airgaps.
- Starting torque shows minimal variation with slight adjustments in airgap length.

II) and III) Efficiency and power factor

- Increasing the airgap results in a slight reduction in efficiency and power factor.

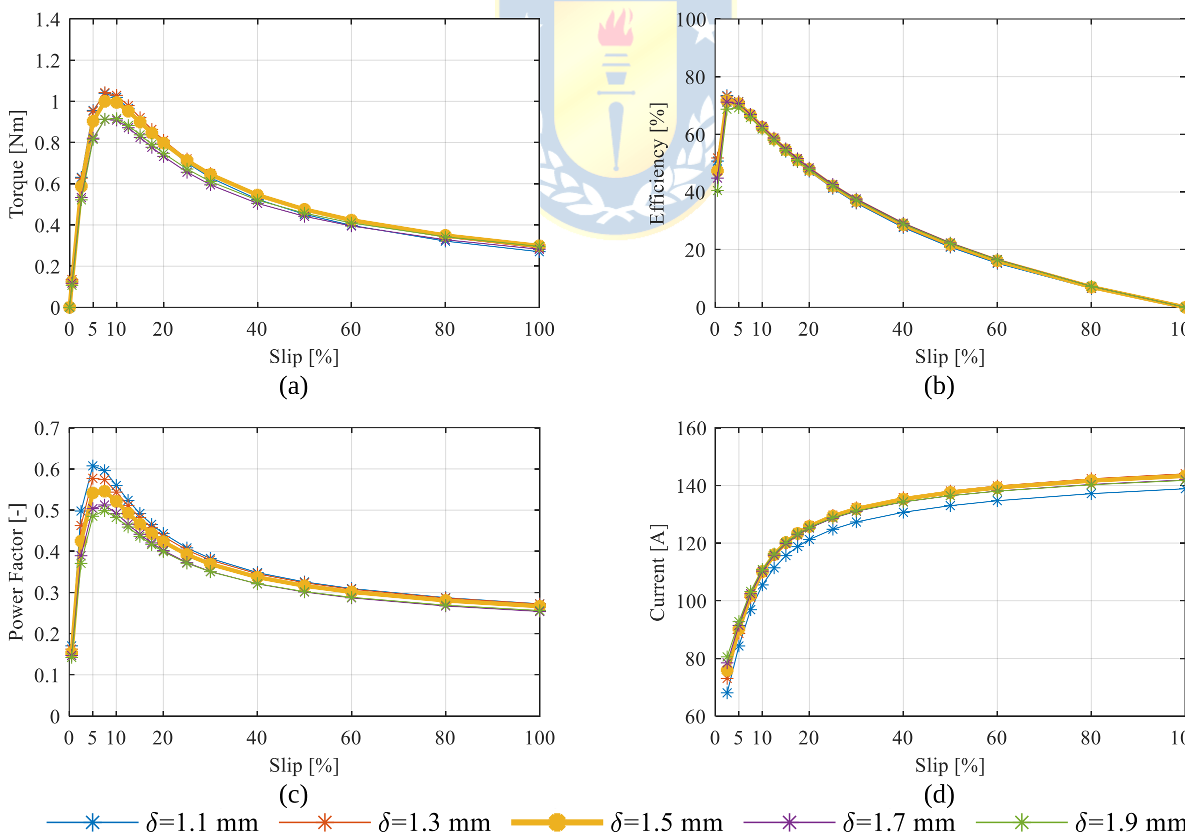

Fig. 3.19 Evaluation of AR-AFIM performance by means of the 3D PMS model when varying airgap length (δ).
a) Torque-slip characteristic, b) Efficiency, c) Power factor; d) Line current.

IV) Line current

- Enlarging the airgap increases the current requirement across all slip values due to corresponding increase in airgap reluctance.

Fig. 3.20 shows relevant performance indices of the MRIM using the 3D PMS model for different slot widths from 9 to 15 mm in steps of 1.5 mm, covering $\pm$ 25% of the original value. In Fig. 3.20(a), Fig. 3.20(b), Fig. 3.20(c), and Fig. 3.20(d), the torque-slip characteristic, efficiency, power factor and current are analyzed, respectively. The findings indicate that:

I) and III) Torque-slip characteristic and power factor:

- Increasing the slot width results in a slight torque improvement, with no significant impact on power factor.

II) Efficiency

- There is a minor reduction in efficiency with increasing slot width.

IV) Line current:

- Enlarging the slot width increases current demand during high slip operations.

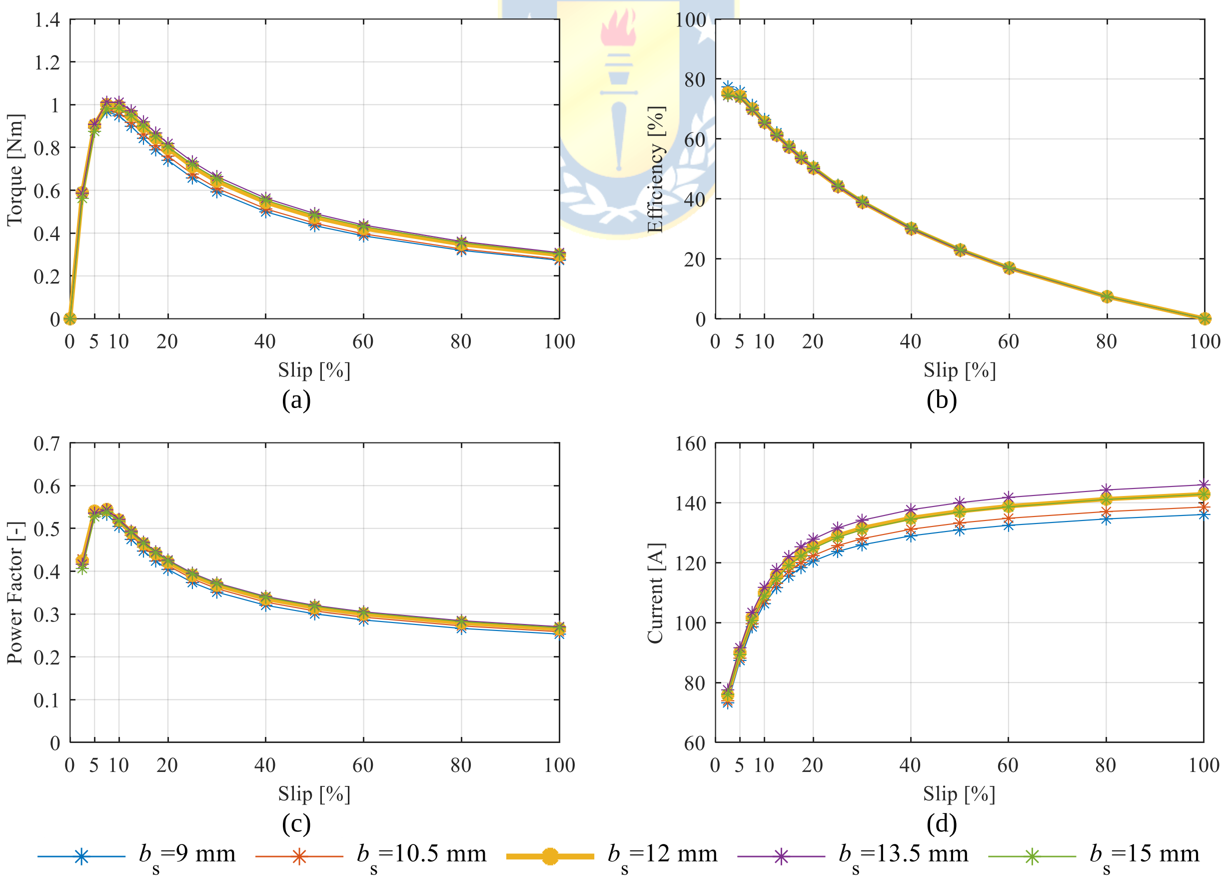

Fig. 3.20 Evaluation of AR-AFIM performance by means of the 3D PMS model when varying slot width (b_s).
a) Torque-slip characteristic, b) Efficiency, c) Power factor; d) Line current.

It should be noted that the initially sized MRIM was designed to operate at a current density of 3A/mm^2, aiming for passive cooling, which represents a low current density value [59].

3.5.2 Evaluation by means of the 3D full model and summary

To validate the primary findings obtained from the PMS 3D model, the full 3D model was also used to evaluate the machine's performance. The slip-torque characteristic, efficiency, and power factor were assessed while varying dimensional parameters. Each design evaluation using the full model required approximately 72 hours using direct solvers. Additionally, variations in D_{fe} values ranging from 2.1 to 3.5 mm were evaluated, representing a $\pm 25\%$ deviation from the original value. However, these assessments demonstrated negligible impact on the torque-slip characteristic, efficiency, or power factor of the machine. Similar conclusions were drawn from assessments of k_{matrix} variations, consistent with Fig. 3.7.

The findings from the full model align with those from the 3D PMS model regarding the machine's performance response to varying design parameters, as summarized in Table 3.8. This confirms that the 3D PMS model effectively enables identifying dimensional parameters influencing the machine's torque-slip characteristic, efficiency, and power factor, with significantly lower computational load.

Table 3.8 Influence of dimensional parameters on AF-MRIM performance indices

Constructive Parameter	**Performance Index**	**Influence**
Rotor height (h_{r})	Torque-slip	Reducing the rotor height increases the slip at maximum torque, reducing the torque capacity at low slips and increasing the maximum torque. The opposite effect is observed when increasing the rotor height.
	Efficiency	Reducing the rotor height increases the slip at maximum efficiency, reducing the efficiency of the machine at low slips. The opposite effect is expected when increasing the rotor height.
	Power factor	Reducing the rotor height decreases the power factor at low slips but improves the maximum power factor the machine can develop. The opposite effect is expected when increasing the rotor height
	Line current	Reducing the rotor height provides a line current decrease for all slips from 0 to 1. The opposite effect is expected when increasing the rotor height
Slot height (h_{s})	Torque-slip	Reducing the slot height provides an overall boost in the machine torque capacity, including starting torque, maximum torque, and low-slip torque. The opposite effect is expected when increasing the slot height.
	Efficiency	No significant effect on the efficiency was observed.
	Power factor	Reducing the slot height provides a power factor increase for high slips, but no significant effect was observed at low slips. The opposite effect at high slips is expected when increasing the slot height
	Line current	Reducing the slot height increases line current for all slips from 0 to 1. The opposite effect is expected when increasing the slot height

Airgap length (δ)	Torque-slip	Increasing the airgap length triggers a significant reduction in the torque capacity. The opposite effect is expected for the case of an airgap length reduction.
	Efficiency	Increasing the airgap length produces a relevant reduction of the efficiency. The opposite effect is expected when the airgap is shortened.
	Power factor	Increasing the airgap length reduces the power factor for all slip values from 0 to 1. The opposite effect is expected when a shorter airgap is adopted.
	Line current	Increasing the airgap length also increases line current requirement for all slips from 0 to 1.
Slot width (b_s)	Torque-slip	No significant effect on the torque-slip was observed.
	Efficiency	No significant effect on the efficiency was observed.
	Power factor	No significant effect on the power factor was observed.
	Line current	Increasing the slot width translates into a current increase at low- and high-slip operation.
Iron wire diameter (D_{fe})	Torque-slip	No significant effect on the torque-slip was observed.
	Efficiency	No significant effect on the efficiency was observed.
	Power factor	No significant effect on the power factor was observed.
	Line current	No significant effect on the line current was observed.

3.6. Section summary

This section presented steps for obtaining and analyzing an attractive design proposal for AF-MRIMs, supported by several devised tools as follows:

- **Analytical Pre-Sizing methodology:** An analytical approach was developed to focus on key design parameters of AF-MRIMs, emphasizing the selection of the matrix rotor structure. It includes equations to determine advisable value of rotor iron proportion and simulations illustrating the impact of iron wire diameter on AF-MRIM performance. Validation was conducted through 3D FE simulations and experimental testing, demonstrating satisfactory outcomes in terms of output power and torque capacity.
- **Semi-Analytical Tool – Progressive Model Simplification (PMS):** A semi-analytical tool was created to assess AF-MRIM performance efficiently. PMS progressively simplifies the complex matrix rotor structure: first to a uniform equivalent material in a 3D model, then to a set of 2D linear models. The tool aids in identifying estimation errors and support multi-objective optimization of AF-MRIMs. It provides electrical machine designers with powerful means to efficiently assess the performance of a MRIM based on computational resources. The integration of PMS with MOGA optimization can significantly enhance an initial AF-MRIM design, yielding improvements in torque capacity, efficiency and power factor.
- **Individual Sensitivity Analysis:** An individual sensitivity analysis was conducted on the initial MRIM design to identify critical parameters influencing machine performance. Results indicate that varying airgap length, rotor height and stator height significantly affect torque,

efficiency, power factor and line current. Conversely, parameters like slot width and iron wire diameter were found to have minimal impact on MRIM performance.

The findings of this section fully address SO1, and partially cover SO2 and SO4 (refer to Section 1.4.2).

4. Tools for assessing the impact of manufacturing uncertainties on synchronous and asynchronous machines

4.1. Introduction

As presented in Section 3, design strategies typically aim to achieve a refined design with assured dimensional parameters. However, upon construction and assembly of the machine, both uniform and non-uniform dimensional deviations may arise, significantly influencing its performance. This section introduces fast methodologies for evaluating design robustness and predicting the effects of dimensional deviations in structural units on electromagnetic torque for typical asynchronous and synchronous machines.

4.2. Uniform and non-uniform uncertainties methods (UUM and non-UUM)

Two approaches are commonly used to assess the impact of manufacturing tolerances on electrical machine performance: the UUM, and the non-UUM [64].

The UUM assumes uniform uncertainty across structural units (e.g. magnets, slots), reducing the number of uncertain parameters and computational burden. This method is often integrated with robust design techniques like Taguchi and six sigma criteria. For example, a time-efficient methodology combining DOE an UUM was proposed in [65] and [66] to evaluate uncertainties affecting the cogging torque of PMSMs. In turn, in [9], uniform tolerance distribution was used to develop a robust design approach for surface-mounted PM motors. Another example can be found in [67], addressing the impact of manufacturing tolerances on cogging torque and back-EMF in PMSMs.

The non-UUM approach considers varying dimensional deviations for each structural unit, reflecting real-world manufacturing variability but requiring assessment of a larger set of machines. This has leveraged the necessity of space-reduction techniques, statistical methods, and semi-analytical approaches. For instance, in [68], the authors evaluated the cogging torque sensitivity of a 12-slot 4-pole motor under tolerances of PM thickness, magnetization and position. The study discretized uncertainty into 3 levels (lower, nominal and upper), calculating all possible combinations through the FEM to examine sensitivity to different parameters. Likewise, in [63], assuming Gaussian distribution of magnet placement on the rotor, a superposition technique was devised to analytically determine cogging torque harmonic magnitudes and analyze uncertainties related to PM and teeth positions. Nonetheless, none of these methods have effectively managed the issue of evaluating the influence of a large number of manufacturing uncertainties so far [64], and there is a scarcity of fast techniques in the literature for assessing the impact of tolerances on machine torque, efficiency and power factor. Aiming at filling this gap, this thesis devises and adapts different tools for assessing synchronous and asynchronous machines, facilitating comparative analysis.

4.3. UUM: Tools to determine the impact of manufacturing tolerances and design robustness.

In this work, three tools are considered to assess the impact of manufacturing tolerances on a machine performance from a UUM perspective: preliminary single-dimensional sensitivity analysis, multi-objective optimization, and representative statistical analysis.

4.3.1 Preliminary sensitivity analysis

Starting from an initial design or an optimized design, it is possible to explore the dimensional parameters that significantly impact machine performance by means of a sensitivity analysis. This can be performed either by evaluating individual variations of parameters (while keeping other parameters constant) or by assessing box-Behnken designs in the vicinity of the initial design, as shown in Fig. 4.1.

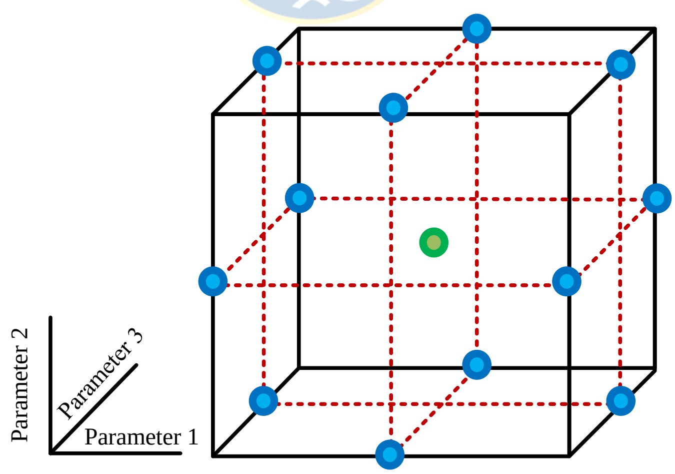

Fig. 4.1 Exploration of designs in the vicinities of the initial design (green dot) by means of box-Behnken design.

The outcome of this initial assessment is useful for identifying parameters that exhibit high sensitiveness and can cause significant variations in performance [69]. Section 3.5.2 is an example of this method, although it focuses on major parametrical variations instead of dimensional tolerances.

In consequence, when assessing tolerances and manufacturing uncertainties, the range of design explorations should cover typical tolerances found in electrical machine manufacturing processes. In the literature, a tolerance of 0.1 mm is commonly accepted in laser cutting and CNC steel punching [43], [73]. This method is applicable to any synchronous and asynchronous machine.

4.3.2 Statistical analysis of a representative set of machine designs

Once the most relevant and sensitive design parameters are identified, a statistical analysis can be conducted using a large number of deviated machines to assess the robustness of each selected machine design. Each selected parameter (P_i) in these random machines should follow a Gaussian distribution of manufacturing dimensional and assembly deviations, within predefined lower and upper tolerance boundaries, illustrated in Fig. 4.2 ranging from -3σ to 3σ. This approach ensures that the assessment better reflects real-world manufacturing processes [50].

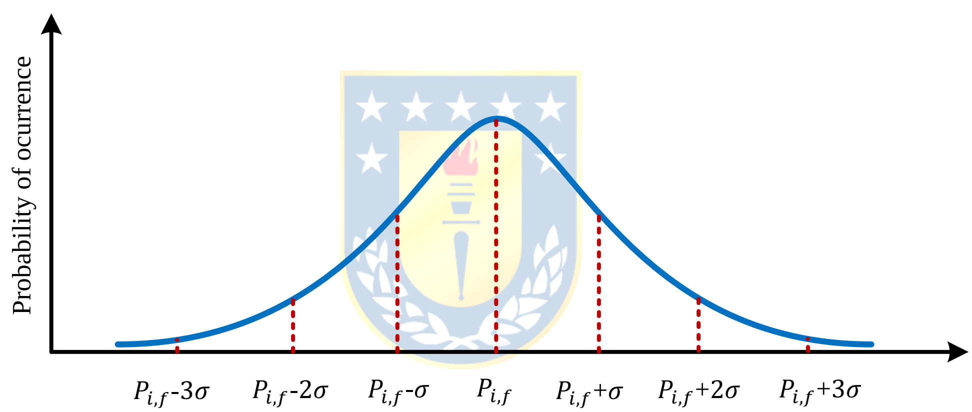

Fig. 4.2 Gaussian distribution of manufacturing uncertainties used for creating a representative set of machines.

Therefore, when assessing N_p parameters under manufacturing uncertainties, it is necessary to generate and evaluate designs with combinations of deviated parameters following a Gaussian distribution across N_p dimensions. This approach increases the number of designs required to achieve better representativeness. Fig. 4.3 visually illustrates the set of designs that require evaluation when $N_p = 3$. Based on the evaluation of this set of deviated machines derived from a single machine specimen, a histogram of performance characteristics can be created to obtain relevant statistical indicators: the median, representing the expected characteristic of the machine specimen; and the standard deviation, which represents the robustness of the design [41]. This analysis must be carried for each design selected for analysis. This method is applicable to synchronous and asynchronous machines.

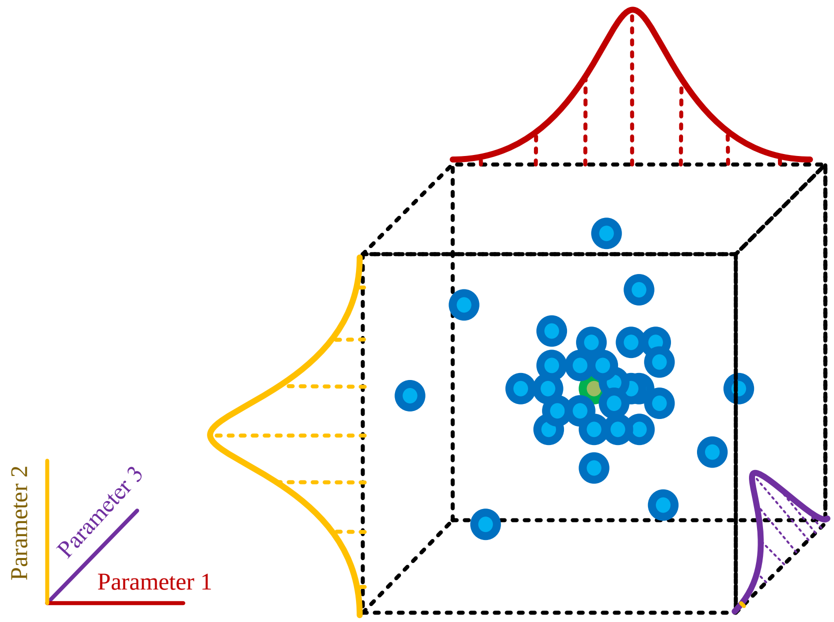

Fig. 4.3 Set of representative designs to assess the impact of manufacturing uncertainties.

4.3.3 Multi-objective optimization seeking the worst uncertain design

When a large number of design parameters are subject to tolerances, conducting a statistical analysis becomes impractical due to the significant computational burden involved. In such cases, search algorithms can be used to find the worst-case design in the vicinity of an initial design. In this thesis, this is addressed by integrating the MOGA with a 2D PMS model for assessing the AF-MRIM and using a 2D model of the machine cross-section with MOGA for radial flux machines. Fig. 4.4 shows a representation of the multi-objective search when $N_p = 3$. The evolution of designs follows a MOGA optimization approach, constrained within tolerance ranges established for each parameter ($\Delta \mathrm{P_i}$) The difference between the worst-case design and the initial design quantifies the robustness of the latter and allows the comparison with other design candidates. This method is applicable to synchronous and asynchronous machines.

4.4. Non-UUM: Time-efficient torque estimation tool for synchronous machines in the presence of non-uniform tolerances.

In this section, the proposed approach to estimate relevant performance indices in the presence of manufacturing tolerances following a non-UUM approach is described and validated for permanent magnet machines and synchronous reluctance machines. This methodology is inspired by the ones developed in [41], [63], [68], and [70]-[72], with results of these sections already published in [73]-[74].

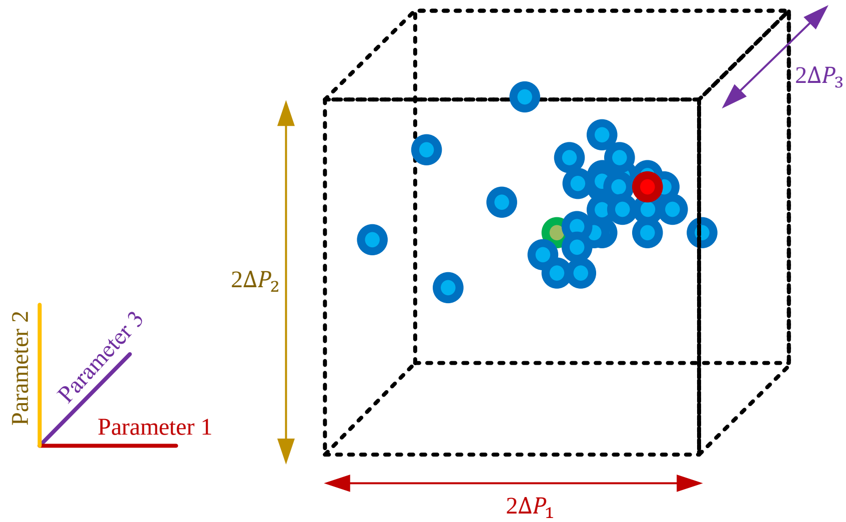

Fig. 4.4 Search for the worst design (red dot) in the vicinities of an initial design (green dot) using the MOGA.

4.4.1 Assumptions, considerations and semi-analytical expressions

In a real manufacturing process, various structural units of an electrical machine (such as slots, magnets, and flux barriers) can exhibit failures that degrade electromagnetic performance. For a single parameter (P_i) subject to a discrete tolerance analysis (e.g, slot height, slot width, tooth-tip length), if F failures are considered in addition to the flawless condition, a total of $F+1$ possible combinations can be assessed. For instance, with $F=2$, parameter P_i could take three values depending on the tolerance range ΔP_i:

- $P_i = P_{i,\mathrm{f}} - \Delta P_i$
- $P_i = P_{i,\mathrm{f}}$
- $P_i = P_{i,\mathrm{f}} + \Delta P_i$

where $P_{i,\mathrm{f}}$ represents the flawless value of the i-th parameter. Higher values of F require evaluating more parameter values within the range $[-\Delta P_i, \Delta P_i]$.

For a synchronous machine topology under analysis, the total number of combinations to evaluate (combinations of $\Delta P_{i,j}$ and $\Delta P_{i,j}$, with $i = 1,2,..,N_p$ and $j = 1,2,..,F+1$) is approximated by

$$Q_{\mathrm{eval}} \cong (F+1)^{N_p \cdot N_{\mathrm{su}}}, \tag{4.1}$$

where N_p is the number of parameters under tolerance analysis and N_{su} is the number of structural units affected by these tolerances. As an example, if only the height, angular position and radial position of magnets in a 20-pole PMSM are to be assessed, then $N_p = 3$ and $N_{\mathrm{su}} = 20$. In turn, for a 3-barrier 6-

pole SynRM, analyzing the end positions of each barrier (2 per barrier), $N_p = 6$, and $N_{\mathrm{su}} = 6$. Evaluating the latter with $F = 2$ would require assessing approximately 387 million designs, making it impractical without space reduction techniques. Therefore, in order to accelerate the non-uniform tolerance analysis for synchronous machines, a method based on the superposition technique was implemented. Its main assumptions and considerations are as follows:

- A discrete tolerance distribution is applied to each parameter, dividing the dimensional range in $F + 1$ values.
- Typical laser-cutting tolerances are taken into account for magnetic steel dimensions, according to [43], [73].
- Poles are treated as relatively independent structural units concerning their electromagnetic response.
- The method allows for consideration of saturation effects, given that it is based on direct FE evaluations.

4.4.2 Expressions

The proposed method aims to reconstruct the torque waveform considering the error contribution of all the structural units of the machine, as explained in the flowchart of Fig. 4.5.

When a certain parameter of a *structural unit* (eg. magnet radial position of a *magnetic pole*) presents a deviation due to tolerances in a machine called *X*, there will be a difference between the developed torque of the machine *X* and the flawless design. A tolerance matrix of $F + 1$ elements is created from a predefined tolerance range in the vicinity of the flawless value, such that:

$$\boldsymbol{M}_{\mathbf{tol},\boldsymbol{i}} = \left[-\Delta\mathrm{P_i}, -\Delta\mathrm{P_i} + \frac{\Delta\mathrm{P_i}}{F}, \Delta\mathrm{P_i} + 2\frac{\Delta\mathrm{P_i}}{F}, \dots, 0, \dots, \Delta\mathrm{P_i}\right]. \tag{4.2}$$

Then, the i-th parameter of the machine *X* can take any value of $\boldsymbol{M}_{\mathbf{tol},\boldsymbol{i}}$. If the element #1 is selected, then the parameter will have the lowest value possible of $\boldsymbol{M}_{\mathbf{tol},\boldsymbol{i}}$. If the element $\#F + 1$ is selected, the parameter will have the highest value of $\boldsymbol{M}_{\mathbf{tol},\boldsymbol{i}}$. An arbitrary element of $\boldsymbol{M}_{\mathbf{tol},\boldsymbol{i}}$ is in the position $\#l$.

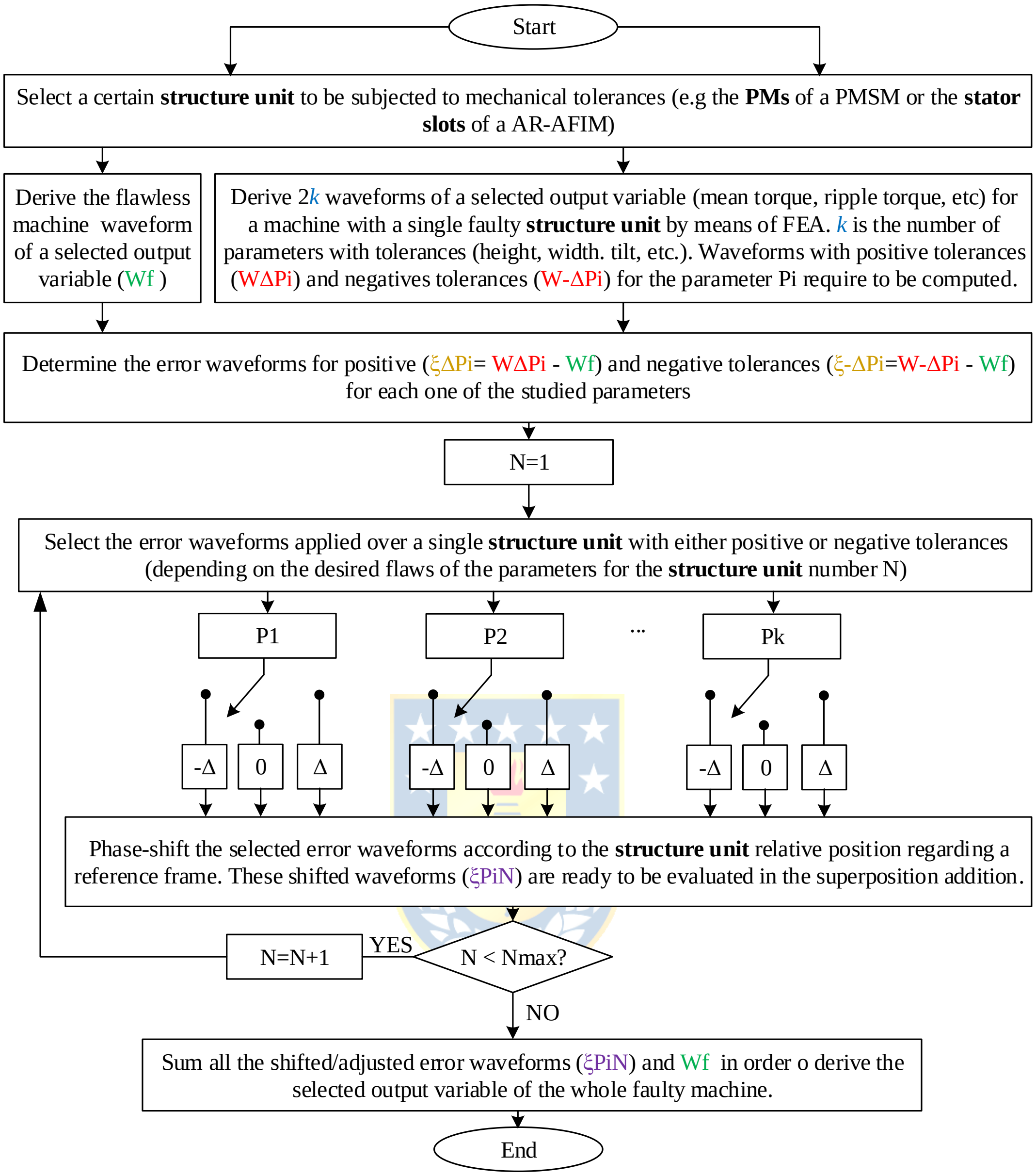

Fig. 4.5 Flowchart of the proposed method to evaluate faulty synchronous machines.

The difference between the developed torque of the machine X (selecting the element $\#l$ of the tolerance matrix) and the flawless design is from now on called tolerance error (ξ), and can be represented by:

$$\xi_{i,j}(\theta_r) = \mathrm{T}_{i,j}(\theta_r) - \mathrm{T}_f(\theta_r), \tag{4.3}$$

where T_f is the torque waveform of the flawless machine, and $\mathrm{T}_{i,j}$ is the torque waveform of a machine with the *i*-th parameter of the *j*-th structural unit being deviated with a severity given by the element $\#l$ of $\boldsymbol{M}_{\mathbf{tol},\boldsymbol{i}}$.

The tolerance error waveforms can be estimated from FE simulations by assessing a single structural unit of the machine, called *reference structural unit* (RSU). Then, the torque of the machine considering any possible deviation within $\boldsymbol{M}_{\mathbf{tol},\boldsymbol{i}}$ on the RSU is given by:

$$\mathrm{T}_{\mathrm{RSU}}(\theta_r) = \mathrm{T}_f(\theta_r) + \sum_{i=1}^{N_p} \{\xi_{i,1,l}(\theta_r)\} \tag{4.4}$$

If the remaining structural units require to be evaluated considering dimensional deviations, then the superposition approach can be applied. This method offers a way to effectively decouple parameters such as slot position, pole placement and pole strength, as it was demonstrated in [71]-[72]. According to [72] and [41], notwithstanding, there are limitations that must be quantified to ensure the synthesis of highly accurate data, such as the effect of high magnitude magnetic saturation, and the magnetic independence of structural units. In this work, and from the findings published in [73], it is assumed that applying a dimensional deviation on other structural units has a similar error waveform as the RSU but with a mechanical angular shift (γ). This assumption is a key aspect of the methodology:

$$\gamma(n) = \frac{360°}{N_{\mathrm{su}}} n, \tag{4.5}$$

where n represents the number of structural units between the unit being assessed and the RSU (for which error waveforms were computed by means of FEA).

Finally, the torque of a machine with any combination of deviations in its SUs can be computed using the torque waveform of the RSU and the tolerance errors calculated for each of the other SUs:

$$\mathrm{T}_{\mathrm{final}}(\theta_r) = \mathrm{T}_{\mathrm{RSU}}(\theta_r) + \sum_{j=1+1}^{N_{\mathrm{su}}} \sum_{i=1}^{N_{\mathrm{p}}} \{\xi_{i,1,l}(\theta_r - \gamma_n(j-1))\}, \tag{4.6}$$

where $\mathrm{T}_{\mathrm{RSU}}(\theta_r)$ is the torque waveform of the RSU (assumed as SU with $j = 1$), and $\xi_{i,1,l}$ represents the tolerance error of the RSU machine due to a deviation in its *i*-th parameter. The value of *l* allows for the selection of different tolerance severities assigned to a SU, as described in (4.2).

4.4.3 Validation for SynRMs, the rare-earth free competitor of IMs

Synchronous reluctance machines (SynRMs) have gained increasing attention in the past decade, especially in applications where enhanced efficiency and cost-effective power conversion is required [75]. When compared with the widely used induction motors (IMs), the absence of rotor windings in SynRM (as sketched in Fig. 4.6) leads to lower rotor losses and higher efficiency for the same frame size. Additionally, SynRM are proposed as a rare-earth magnet-free technology with lower cost than permanent magnet (PM) machines [76]. Moreover, they are highly reliable, robust, and easy to maintain. Nevertheless, they have two critical disadvantages with an impact on their competitivity as stated in the literature: high torque ripple and low power factor [77].

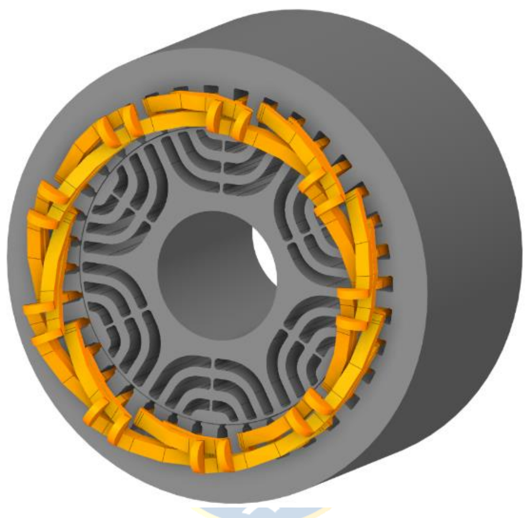

Fig. 4.6 3D sketch of a triple-barrier six-pole synchronous reluctance machine.

The performance of SynRM is strongly dependent on the rotor configuration and shape of the flux barriers [78]. Their dimension and position within the rotor, including the thickness and design of the iron bridges are main contributors of the torque ripple [79]. Accurate refinements of the rotor parameters have been proposed in the literature, aiming at improving the machine performance [80]-[81]. Notwithstanding, these analyses are based on designs with exact dimensions, and the impact of manufacturing/dimensional tolerances or material degradation has been scarcely included in the design steps for SynRM [79]. This configures as a very critical aspect that can lead to significant differences between the expected performance (from the blueprint) and the built machine if the dimensional tolerances are not considered [84]: the expected performance enhancements stemmed from advanced techniques may not be effectively obtained if dimensional deviations are present in the manufactured machine. In this regard, tolerance analysis on SynRM is mandatory if accurate refinements of the rotor structure are adopted. Analytical models found in literature [83]-[84] do not consider the non-linearities of the machine and often limit its application to low-speed scenarios. Although these models are considerably helpful to derive preliminary design parameters, they are not compatible with tolerance analysis requirements. In this regard, a fast yet accurate performance evaluation method for multi-barrier SynRMs including dimensional allowances and focusing on their electromagnetic torque generation was developed and published in [74].

In order to validate the proposed torque reconstruction method, SynRM specimens with two and three pole pairs, each with one or two barriers per pole, were assessed using exaggerated tolerances on the barrier positions (left and right flux barrier positions, in mechanical degrees). This results in a total of four machines, illustrated in Fig. 4.7. Non-optimized SynRMs were considered for this thesis to better visualize the effect of rotor structure variations on the torque waveform.

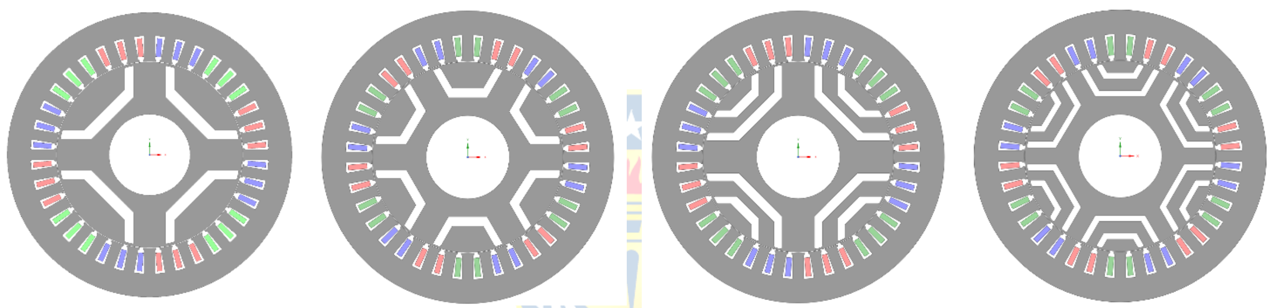

(a) (b) (c) (d)

Fig. 4.7 2D schematics of selected SynRMs to validate the proposed semi-analytical tool
(a) four pole with one barrier; (b) four pole with two barrier; (c) six pole with one barrier; (d) six pole with two barrier.

The common data for all machines are presented in Table 4.1. Specific rotor data for the machines with one and two barriers are provided in Table 4.2 and Table 4.3 respectively. Fig. 4.8 and Fig. 4.9 show the schematic of rotor parameters for the selected one-barrier and two-barrier machines, respectively.

Table 4.1 Common data for all selected SynRMs

Parameter	Symbol	Value
Stator outer diameter	D_{so}	245 mm
Stator inner diameter	D_{si}	161.4 mm
Rotor inner diameter	D_{ri}	70 mm
Air-gap length	δ	0.5 mm
Stack length	l_{stk}	120 mm
Number of slots	Q_{s}	36
Speed	n	3000 rpm
Stator current density	J_{s}	10 A/mm^2
Current angle	$\alpha_{\mathrm{i}}^{\mathrm{e}}$	60°electric

Table 4.2 Specific data of 1-barrier rotors

		4-pole	6-pole
Parameter	**Symbol**	**Value**	**Value**
Flux barrier position (right)	α_r	8°	8°
Flux barrier position (left)	α_l	8°	8°
Flux barrier opening (right)	β_r	5°	5°
Flux barrier opening (left)	β_l	5°	5°
Flux barrier width q-axis	t_{b_q}	10 mm	8 mm
Flux barrier width d-axis (right)	$t_{b_{dr}}$	5°	5°
Flux barrier width d-axis (left)	$t_{b_{dl}}$	5°	5°
Inner barrier radius	R_b	45 mm	50 mm
Insulation ratio	k_{air}	0.11	0.08

Parameters considered for the proposed method

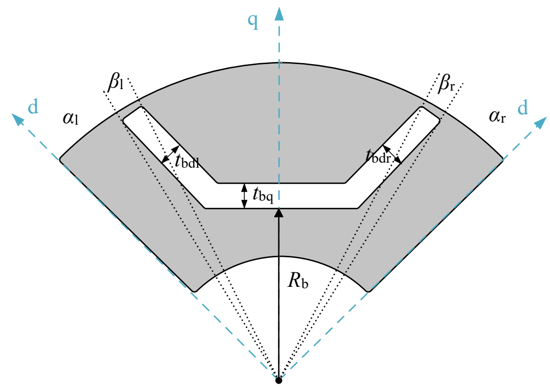

Fig. 4.8 Schematic of the rotor structure for a 1-barrier configuration.

Table 4.3 Specific data of 2-barrier rotors

		4-pole	6-pole
Parameter	**Symbol**	**Value**	**Value**
Flux barrier (1) position (right)	α_{r1}	10°	6°
Flux barrier (1) position (left)	α_{l1}	10°	6°
Flux barrier (2) position (right)	α_{r2}	10°	5°
Flux barrier (2) position (left)	α_{l2}	10°	5°
Flux barrier (1) opening (right)	β_{r1}	5°	4°
Flux barrier (1) opening (left)	β_{l1}	5°	4°
Flux barrier (2) opening (right)	β_{r2}	5°	4°
Flux barrier (2) opening (left)	β_{l2}	5°	4°
Flux barrier (1) width q-axis	$t_{b_{q1}}$	8 mm	5 mm
Flux barrier (2) width q-axis	$t_{b_{q2}}$	8 mm	5mm
Flux barrier (1) width d-axis (right)	$t_{b_{dr1}}$	5°	4°
Flux barrier (1) width d-axis (left)	$t_{b_{dl1}}$	5°	4°
Flux barrier (2) width d-axis (right)	$t_{b_{dr2}}$	5°	4°
Flux barrier (2) width d-axis (left)	$t_{b_{dl2}}$	5°	4°
Width between barrier 1-2	w_q	7 mm	10 mm
Inner barrier radius	R_b	60 mm	65 mm
Insulation ratio	k_{air}	0.17	0.11

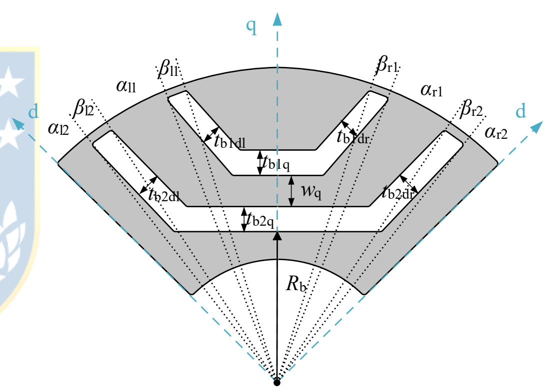

Fig. 4.9 Schematic of the rotor structure for a 2-barrier configuration.

In this validation, the position of the barriers (α_{r} and α_{l}) is varied since it has proven to develop a significant impact on the SynRM performance. Fig. 4.10 depicts the representation of possible failures of the right position of a single rotor barrier with $F = 2$. In this case, the parameter α_r can adopt three values ($l = 1, 2$ and 3): $\alpha_{\mathrm{r},i} = \alpha_{r,\mathrm{f}} - \Delta\alpha_r$; $\alpha_{\mathrm{r},i} = \alpha_{r,\mathrm{f}}$, and $\alpha_{\mathrm{r},i} = \alpha_{r,\mathrm{f}} + \Delta\alpha_r$, with $\Delta\alpha_r$ being the upper limit of the tolerance range. If F is higher, then more values of α_r must be evaluated within the range $[-\Delta\alpha_r\ ,\ \Delta\alpha_r]$.

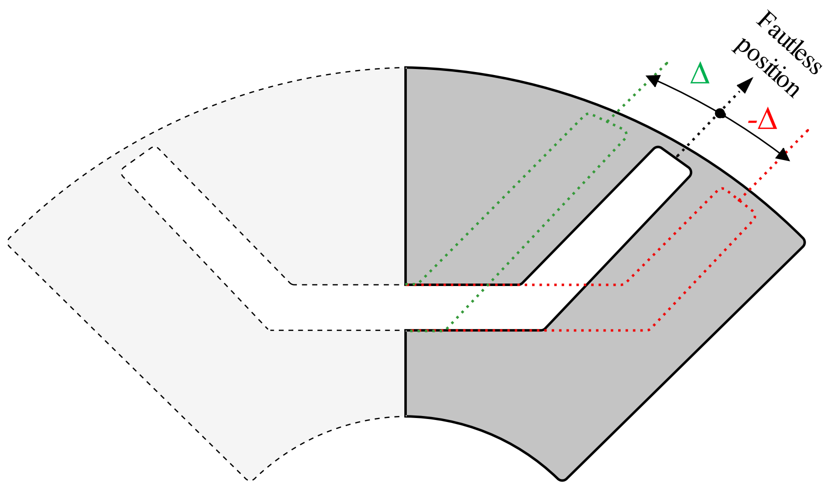

Fig. 4.10 Schematics of possible failures with $F = 2$ on the right side of a barrier of a single pole.

Adapting from (4.1), and focusing on the relevant SUs of the SynRMs, which are the rotor barriers, the number of combinations which require to evaluate for assessing the impact of manufacturing tolerances is given by:

$$Q_{\text{eval,SynRM}} \cong (F+1)^{4 \cdot p \cdot b} \tag{4.7}$$

Fig. 4.11(a) presents the flowchart for implementing the method described in Section 5.2.1 on SynRMs, while Fig. 4.11(b) presents the simplified methodology for reconstructing the torque waveform in the presence of manufacturing tolerances.

As described in (4.3), the tolerance error generated from the displacement of the left side of the *m*-th barrier can be expressed as:

$$\xi_{lm,l}(\theta_r) = \mathrm{T}_{\mathrm{l}m,l}(\theta_r) - \mathrm{T}_f(\theta_r), \tag{4.8}$$

where T_f is the torque waveform of the flawless machine, and $\mathrm{T}_{\mathrm{l}mi}$ is the torque waveform of a machine where the left side of the m-th barrier is affected by a deviation magnitude (related to *l*). In turn, the error generated by displacements of the right side of the m-th barrier is:

$$\xi_{rm,l}(\theta_r) = \mathrm{T}_{\mathrm{r}m,l}(\theta_r) - \mathrm{T}_f(\theta_r), \tag{4.9}$$

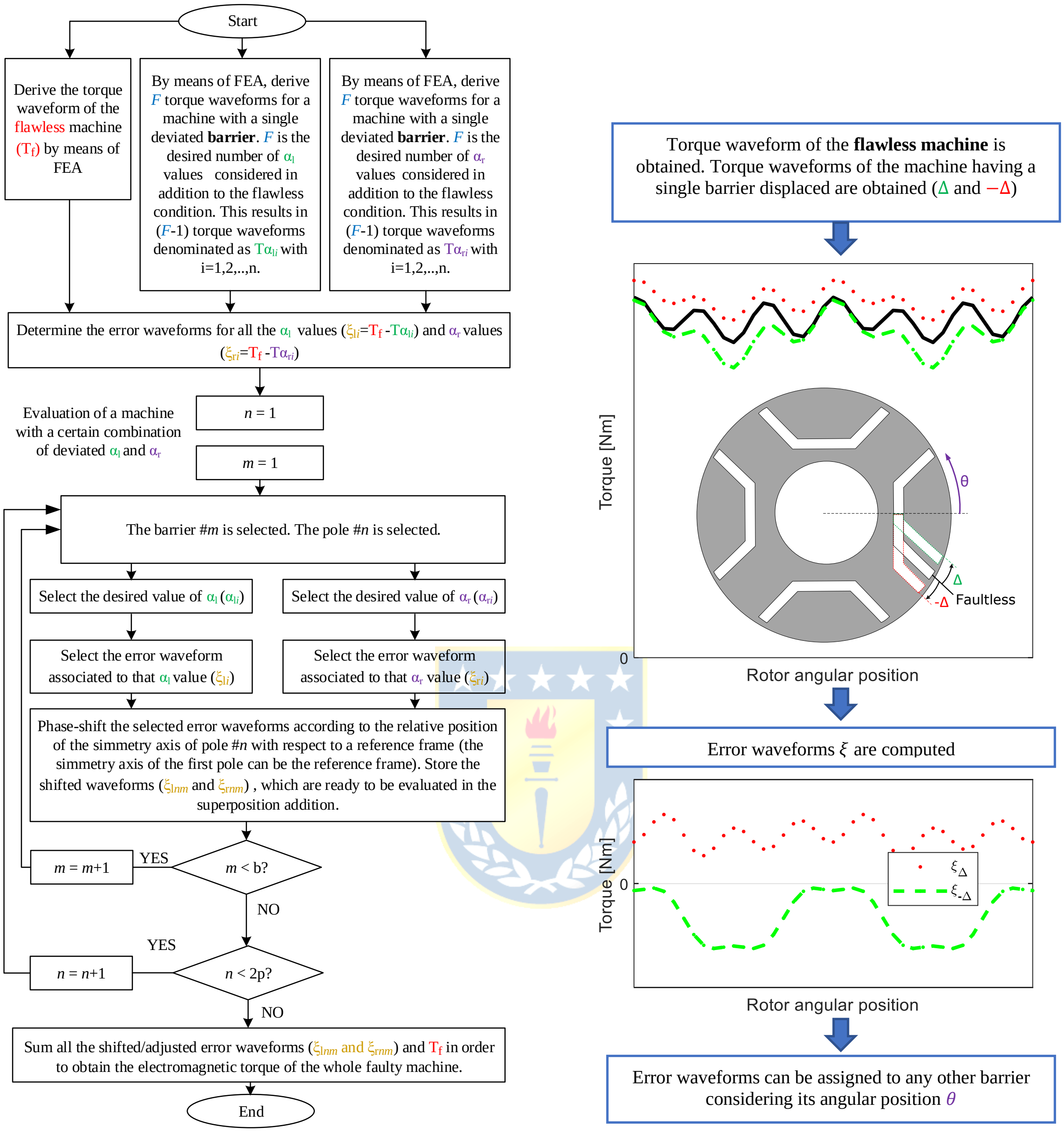

(a) (b)

Fig. 4.11 Explanation of the methodology adaptation in order to be applicable in SynRM.
(a) Detailed flowchart of the proposed methodology to estimate torque waveforms from a few FE simulation runs. (b) Visual explanation of the adapted methodology. Error waveforms are obtained to reconstruct the torque of faulty machines.

where $\mathrm{T}_{rm,l}$ is the torque waveform of a machine which right side of the m-th barrier is affected by a deviation magnitude (related to l). Both $\xi_{lm,l}(\theta_r)$ and $\xi_{rm,l}(\theta_r)$ for $m = 1,2, \ldots, b$ and $l = 1,2, \ldots, F + 1$ can be obtained from FE simulations considering deviations on a single pole of the machine, called reference pole. Therefore, the torque of the machine considering any possible deviation (within the established tolerance matrix) on the reference pole of the machine is given by:

$$T_{\mathrm{RSU}}(\theta_r) = T_f(\theta_r) + \sum_{m=1}^{b}\{\xi_{lm,1}(\theta_r) + \xi_{rm,1}(\theta_r)\} \tag{4.10}$$

As described in (4.5), the errors of the other poles can be obtained from the RSU, considering a mechanical angular shift (γ_{SynRM}) given by:

$$\gamma_{\mathrm{SynRM}} = \frac{180°}{p}n \tag{4.11}$$

Thus, the torque of a SynRM with any combination of displacements on its barriers can be computed as:

$$T_{\mathrm{final}}(\theta_r) = T_f(\theta_r) + \sum_{n=1}^{2p}\sum_{m=1}^{b}\{\xi_{lm,1}(\theta_r - \gamma(n-1)) + \xi_{rm,1}(\theta_r - \gamma(n-1))\}. \tag{4.12}$$

The four machines presented in Fig. 4.7 were evaluated with different displacement values (α_{ri} and α_{li}). This validation consists of comparing the outcome of:

- The proposed method, requiring few simulation runs to obtain input torque waveforms. These waveforms are used to estimate the torque of several machines with deviated dimensional parameters.
- Direct FE evaluation of machines with deviated dimensional parameters.

FE simulations were carried out using ANSYS Electronic Desktop software package for a rotor speed of 3000 rpm and a current density of 11.8 A/mm^2. The current angle was fixed at 60 electrical degrees and the magnetic steel chosen was M350-50A. For both cases, a high-density mesh was considered for the airgap, bridge and barrier zones to obtain an accurate input for the proposed semi-analytical method and a fair comparison between results. In Fig. 4.12, the used FE model and the obtained flux density distribution for the flawless case of each machine are presented. A maximum value of ~2.3 T was obtained around the bridges and ~1.8 T in the teeth and stator-yoke areas. In this sense, mild saturation is considered in this paper to demonstrate the applicability of the proposed method.

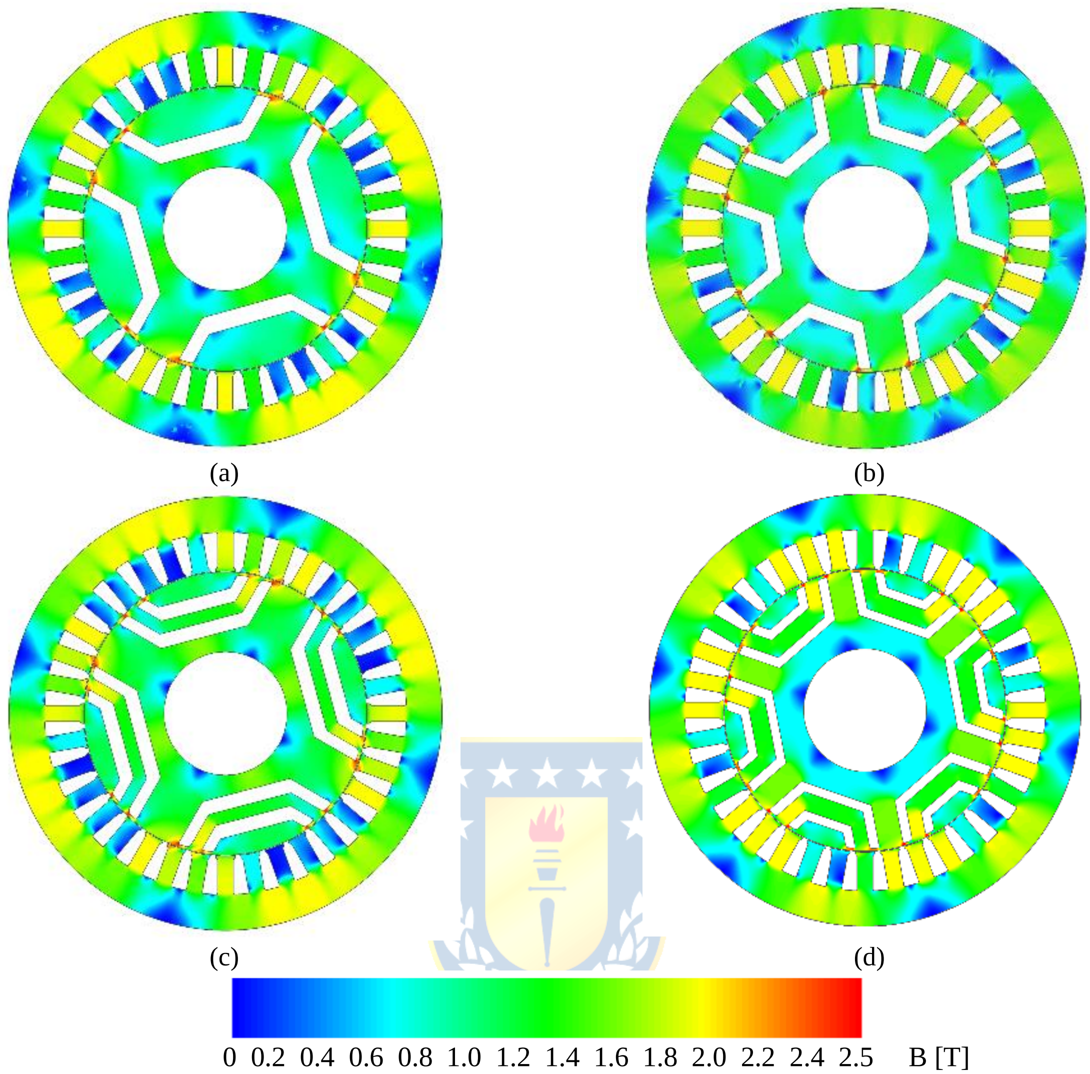

Fig. 4.12 Flux density distribution of the selected machines without dimensional deviations
(a) four pole with one barrier; (b) four pole with two barrier; (c) six pole with one barrier; (d) six pole with two barrier.

Exaggerated displacements on the left side and the right side of the barriers of the machine were considered (refer to Fig. 4.10). This, in order to obtain significant torque variations with respect to the flawless machine and disclose the differences between the proposed method and direct FE evaluation.

The comparison of the rated torque between FEA and the proposed method for the validation scenarios is presented in Fig. 4.13. In Annex B, Table B.1 provides the details of these scenarios.

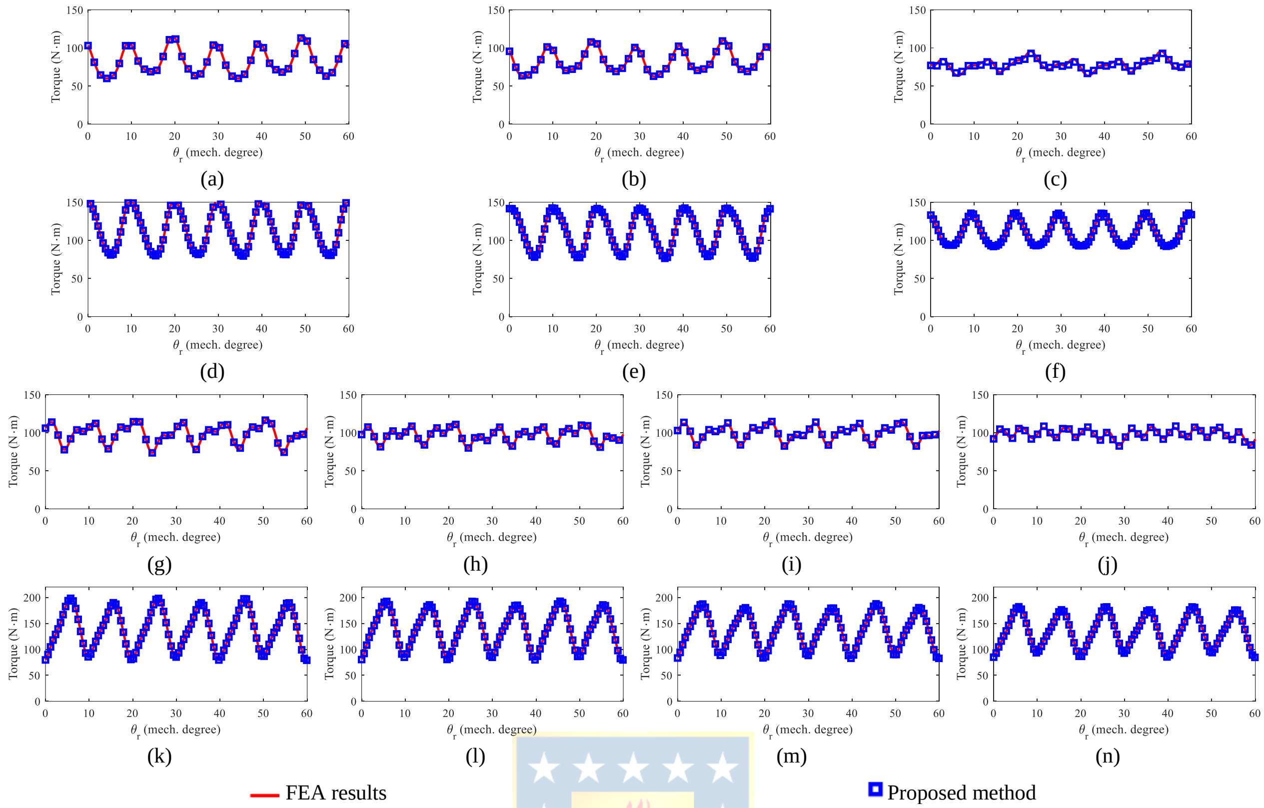

Fig. 4.13 Comparison of the rated torque between FEA and the proposed method
(a), (b), (c) 4P1B machine (d), (e), (f) 6P1B machine; (g), (h), (i), (j) 4P2B machine, and (k), (l), (m), (n) 6P2B machine. Specifications of these scenarios can be found in Table 4.3.

Fig. 4.13 demonstrates consistent results across different methods, even when significant waveform changes and mild saturation are considered. Take as an example the different torque waveforms obtained from Fig. 4.13(g) and Fig. 4.13(j), or the transition between Fig. 4.13(a) to Fig. 4.13(c). The method effectively captures variations in the torque waveform.

Additionally, a second validation involved 100 machine designs with randomly generated dimensional deviations, yielding accurate results. Comparison of torque waveforms estimated by the proposed method with those obtained via direct FE evaluation showed a mean average error below 6%. To replicate this accuracy when implementing the proposed method, it is recommended to use a high-quality mesh and a sampling time adhering to the Nyquist theorem. Likewise, if reducing the simulation time is required, simulating only one electrical period can suffice to obtain baseline results. It is relevant to note that there are no material selection constraints that must be followed in order to obtain accurate estimations.

4.4.4 *Validation for PMSMs, the pinnacle of performance in LSHT applications.*

LSHT motors are essential in direct-drive applications such as energy production, industrial automation, low-head pumps and ship propulsion. PMSMs, illustrated in Fig. 4.14, are widely used in these applications due to their high pole count and strong rare-earth magnets, ensuring high torque density [85]-[87]. Moreover, the integration of TCW configurations with PMSMs provide several advantages over DW counterparts [88], including shorter end windings, low cogging torque, compactness, and a high copper space factor. These features collectively improve the machine's power to weight ratio.

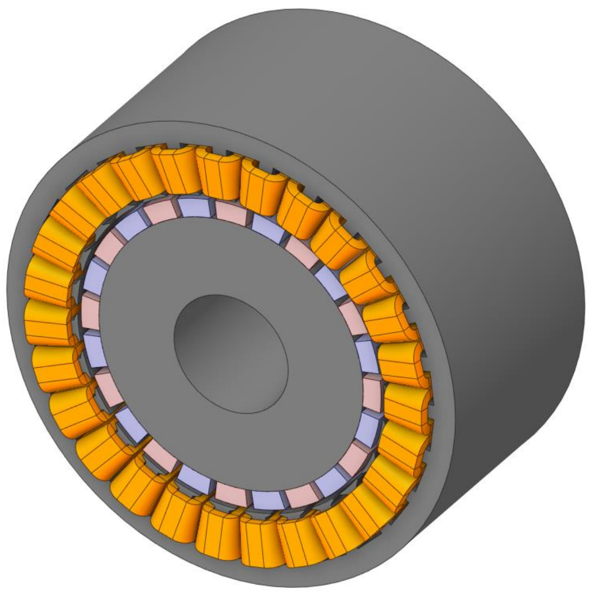

Fig. 4.14 27-slot 24-pole radial-flux TCW-PMSM with surface mounted magnets.

Nonetheless, assembly tolerances such as magnet misplacement, impact both the period and the peak-to-peak value of cogging torque, an inherent undesired effect in PM machines [89]-[90]. Dimensional tolerances also modify the back electromotive force, leading to circulating currents in the stator windings [91]-[92]. Similar effects are obtained from variations in magnetization of the PMs [93]. Among relevant performance indices for PMSMs, cogging torque is critical due to its strong dependence on the geometry of magnets and slots, which are susceptible to manufacturing imperfections. As an example, recent research have demonstrated that asymmetry in the stator generated during punching can lead to an extremely increased cogging torque harmonic content [94], while other performance indices may remain relatively unaffected when subjected to eccentricity tolerances [95].

In this work, several combinations of faulty magnets are evaluated using a non-UUM approach, using a semi-analytical adaptation of the superposition method described in [68]. Rotor magnet angular displacement, rotor magnet radial displacement, and magnet remanence deviations are assessed using three tolerance matrices, expressed as follows:

$$\boldsymbol{M}_{\mathbf{tol},\mathbf{1}} = [-0.1°; -0.05°\,;\ 0°; 0.05°;\ 0.1°]. \tag{4.13}$$

$$\boldsymbol{M}_{\mathbf{tol},\mathbf{2}} = [-0.2\text{ mm}\,, -0.1\text{ mm};\ \ 0;\ \ 0.1\text{ mm}, 0.2\text{ mm}]. \tag{4.14}$$

$$\boldsymbol{M}_{\mathbf{tol},\mathbf{3}} = [-5\%, -2.5\%\,, 0, 2.5\%, 5\%]. \tag{4.15}$$

Then, the torque of the PMSM with any combination of faults in its magnets can be computed by adapting (4.6):

$$\mathrm{T}_{\text{final}}(\theta_r) = \mathrm{T}_f(\theta_r) + \sum_{n=1}^{2p}\sum_{i=1}^{3}\{\xi_{n,i,1}(\theta_r - \gamma(n-1))\}. \tag{4.16}$$

The validation of this method is conducted on a 27-slot 24-pole TCW-PMSM, illustrated in Fig. 4.15, with main data summarized in Table 4.4.

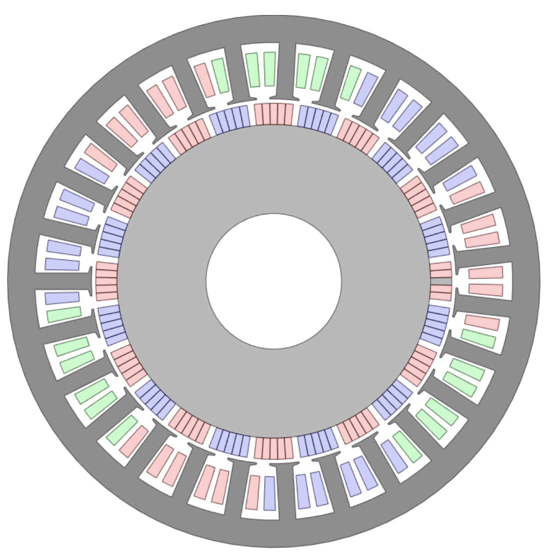

Fig. 4.15 Schematics of the considered TCW-PMSM to validate the adaptation of torque estimation tools.
(a) 24-slot 20-pole machine; 27-slot 24-pole machine.

Table 4.4 Main data of the considered TCW-PMSM, used to validate torque estimation tools

Symbol	Quantity	Value	Unit
l_{ef}	Effective core length	250.0	mm
D_{so}	Stator outer diameter	250.0	mm
δ_{g}	Air-gap length	3	mm
h_{s}	Slot height	50.0	mm
b_{t}	Tooth width	16.0	mm
h_{ys}	Height of the stator yoke	25.0	mm
h_{yr}	Height of the rotor yoke	60.0	mm
h_{tt}	Height of tooth-tip	3.0	mm
h_{pm}	PM height	20.0	mm
B_{r}	PM remanence	1.08	T
μ_{r}	Relative recoil permeability	1.041	-
N_{phase}	Turns per phase	117	-

In Annex B, Table B.2 groups the main data of the validation scenarios, including the tolerance ranges and severities assigned to each design. Fig. 4.16 compares the electromagnetic torque obtained through direct FE analysis with the fast torque estimation tool described in Section 4.4.1, specifically for the 24-pole PMSM.

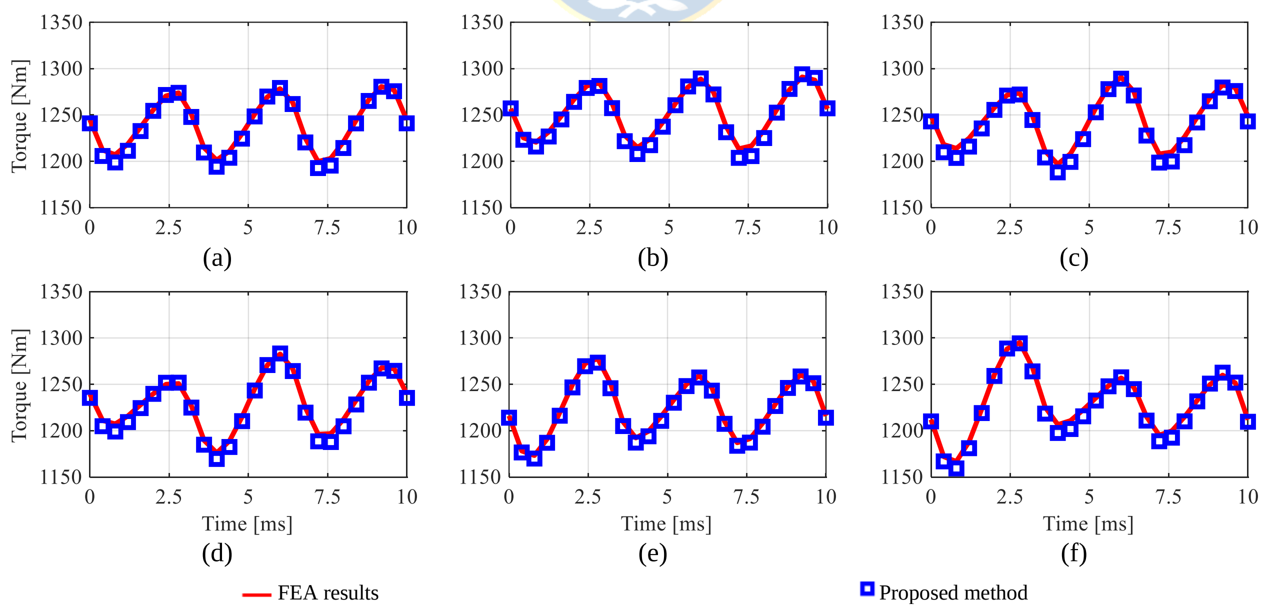

Fig. 4.16 Comparison of the rated torque between FEA with the proposed method when assessing electromagnetic torque of a 27-slot 24-pole PMSM.

Fig. 4.16 shows that in all 6 cases, the torque waveforms obtained have strong agreement, demonstrating that the proposed non-UUM estimation tool effectively tracks variations in torque waveform even under severe waveform variations and mild saturation.

4.4.5 Discussion and applicability

For SynRMs, results indicate a significant reduction in computation time, approximately 99.993%, compared to direct FE analysis of rotor barrier tolerance effects on torque ripple. In turn, for PMSMs, results showcased a considerable computation time reduction, approximately 99.992%, compared to direct FE evaluation of magnet displacement effects on electromagnetic torque. These validations enable detailed tolerance analysis of rotor geometries and assessment of asymmetric designs. To disclose the robustness of a design, nonetheless, these tools must be integrated with statistical analysis.

4.5. Non-UUM: Other relevant tools.

In the case of asynchronous machines, a statistical analysis of uniformly distributed or gaussian distributed tolerances can be performed following a non-UUM approach. In this scenario, each structural unit can adopt different and independent levels of tolerance (F). Nonetheless, achieving a representative set of machine designs, as depicted in Fig. 4.3, is challenging due to exponential increase in search space dimensions. Performing a statistical non-UUM assessment through direct FE analysis involves a significant computational burden due to the following time-consuming factors:

- The entire machine must be simulated or evaluated, and the design periodicity or symmetry cannot be exploited.
- The number of parameters subject to tolerance increases by a factor of N_{su}, which is critical in high pole-count or high slot-count machines, such as LSHT designs.

As a solution, using multi-objective optimization to identify the worst-case design within tolerance ranges is an effective approach for establishing the lower performance boundary of a machine design. Finally, non-UUM assessment is recommended if a space-reduction technique is available, or if the number of dimensional parameters subject to analysis is limited. Moreover, it is relevant to evaluate the relevance of non-UUM evaluation: asynchronous machine generally exhibit low sensitivity to slightly asymmetrical structures, unlike SynRM [77], or cases of PMSM where minimizing cogging torque is critical [41].

4.6. Section summary

In this section, mathematical tools and semi-analytical methods sourced from existing literature were adapted to evaluate design robustness and predict the impact of dimensional deviations on performance ratings of asynchronous and synchronous machines. Key points of this section are described below:

- For fast tolerance analysis in asynchronous and synchronous machines, a UUM assessment can be conducted. This method assumes uniform dimensional deviations across the parameters of structural units (e.g. stator slot height), reducing computational burden while disclosing design robustness.
- Design robustness can be identified by UUM tools, including: i) statistical analysis of the performance provided by a representative set of machine designs under Gaussian-distributed manufacturing tolerances; ii) multi-objective optimization to disclose worst-case designs within typical tolerance ranges.
- In order to conduct a comprehensive non-UUM tolerance analysis in synchronous machines, a semi-analytical tool based on the superposition method was adapted and general expressions were provided; such assessments evaluate non-uniform dimensional variations across structural units, and are required for torque ripple evaluation in PMSMs and torque computation in SynRMs. Validation included a 27-slot 24-pole PMSM and four SynRM, demonstrating strong agreement with existing literature and significant simulation time reduction of over 99.9%.
- The points raised above support the comparative analysis in Section 5 by not only evaluating the performance of exact design buy also considering performance variability due to manufacturing tolerances, essential for robust design practices.

The findings of this section completely cover SO2, and contributes to the fulfillment of SO4 (refer to Section 1.4.2).

5. Comparative study of AF-MRIM and conventional machines: disclosing the suitability of matrix-rotor machines

5.1. Introduction

This section aims to compare AF-MRIMs with both non-conventional and conventional topologies, evaluating their raw performance and robust design capabilities. The goal is to assess the suitability and competitiveness of AF-MRIMs in LSHT applications.

5.2. Advantages of the matrix rotor: preliminary comparison with regular AFIM

To preliminary compare the performance of the proposed MR-AFIM with a conventional axial-flux induction machine, the matrix rotor of the initially-sized MRIM (refer to Section 3.3.1) was replaced with an axial squirrel cage rotor. The resulting machine design is illustrated in Fig. 5.1, utilizing a non-skewed rotor structure. This decision was based on evidence that skewing reduces torque capacity and power factor in order to minimize torque ripple, which is not the main focus in LSHT applications.

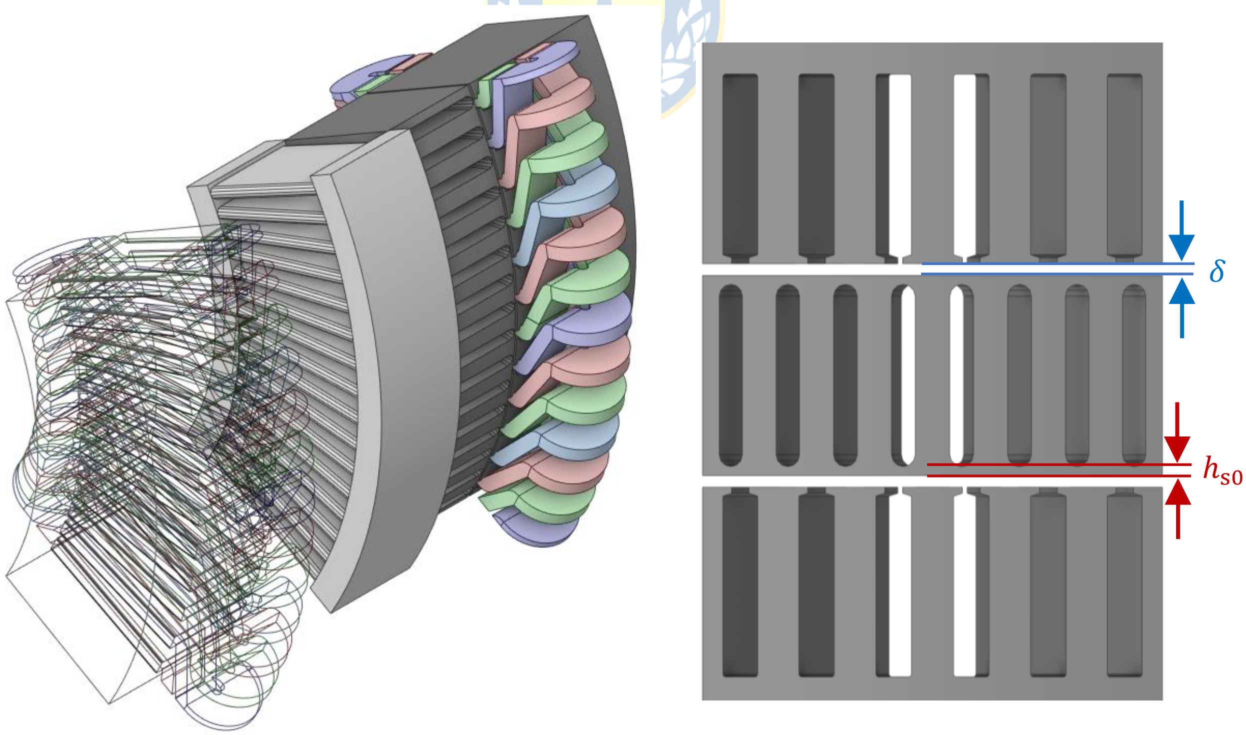

(a) (b)

Fig. 5.1 Matrix rotor of the proposed MRIM was replaced with a squirrel-cage for comparison ends.
(a) Sketch of a four-pole section of the SC-AFIM; (b) Depiction of airgap length ($\boldsymbol{\delta}$) and squirrel cage depth ($\boldsymbol{h_{s0}}$).

As initially described in Section 1.1, adopting a high pole count in conventional IMs leads to significant flux leakage, impacting overall machine performance. Two main parameters influencing flux leakage are airgap length and bar depth, depicted in Fig. 5.1(b). To ensure a fair comparison, the airgap length is maintained equal to that of the original MRIM, allowing for variations in bar depth dimensioning. From a magnetic circuit perspective, enlarging h_{s0} should increase flux leakage, resulting in a substantial decrease in torque capacity, power factor, and efficiency. By the contrary, positioning the rotor bars closer to the airgap reduces flux leakage, potentially enhancing overall machine performance. However, this approach leads to a more complicated rotor manufacturing and compromises the mechanical robustness of the rotor structure. When $h_{s0} = 0$ mm, the rotor core consists of Q_r individual segments that must be bonded to the rotor cage using specific adhesives or carefully soldered, which is undesirable for applications involving fluctuating high-torque conditions. Fig. 5.2 presents a performance comparison of the equivalent SC-AFIM with varying values of h_{s0}.

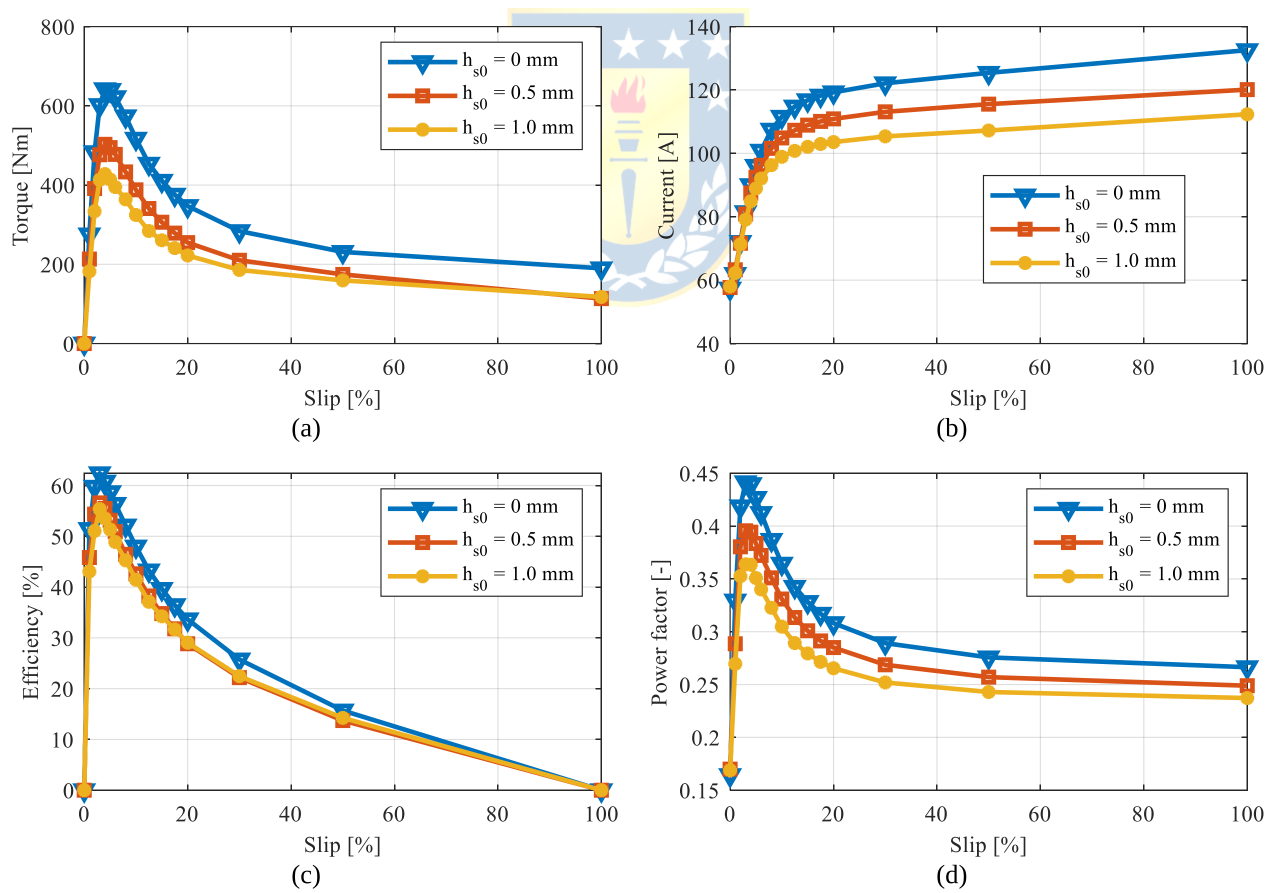

Fig. 5.2 Electromagnetic response of the equivalent AF-SCIM across the entire motor slip range, considering various rotor bar depths (h_{s0}).

(a) Electromagnetic torque. (b) RMS value of stator line current. (c) Efficiency. (d) Power factor.

From Fig. 5.2. it is evident that lower values of h_{s0} correspond to significantly higher torque capacity, power factor, and efficiency. A detailed examination of flux density lines is provided in Fig. 5.3, showing additional magnetic paths that do not cross the airgap when h_{s0} is higher, hence not contributing to torque production.

(a)

(b)

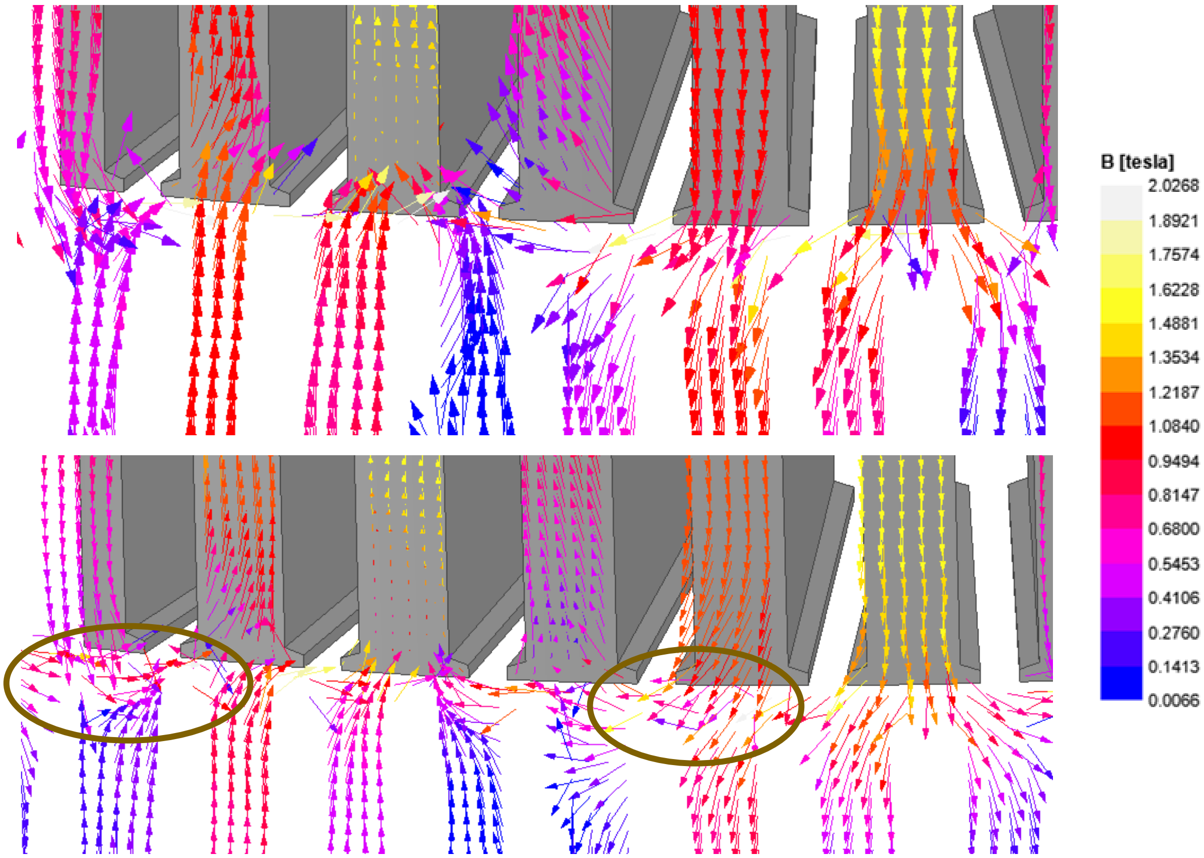

Fig. 5.3 Close-up of the flux density distribution around the airgap, focusing on flux leakage and magnetic paths that do not cross the airgap.

(a) $\boldsymbol{h_{s0} \to 0}$ **mm**; (b) $\boldsymbol{h_{s0} = 1}$ **mm**.

In this context, the best performance is achieved with the smallest achievable h_{s0} value. For comparative purposes, despite its impracticality and relative infeasibility, the AF-SCIM configured with $h_{s0} = 0$ is selected to benchmark against the initially sized MRIM, as illustrated in Fig. 5.4. It can be noted that replacing the matrix rotor with a squirrel cage significantly compromises the performance of the machine. Specifically, there is a 12-point reduction in power factor, a 35% decrease in torque capacity, and efficiency drops by 10-15 percentage points. In turn, current values were found to be comparable between both designs. These findings start to showcase the matrix-rotor design advantages in high-pole-count low-speed applications.

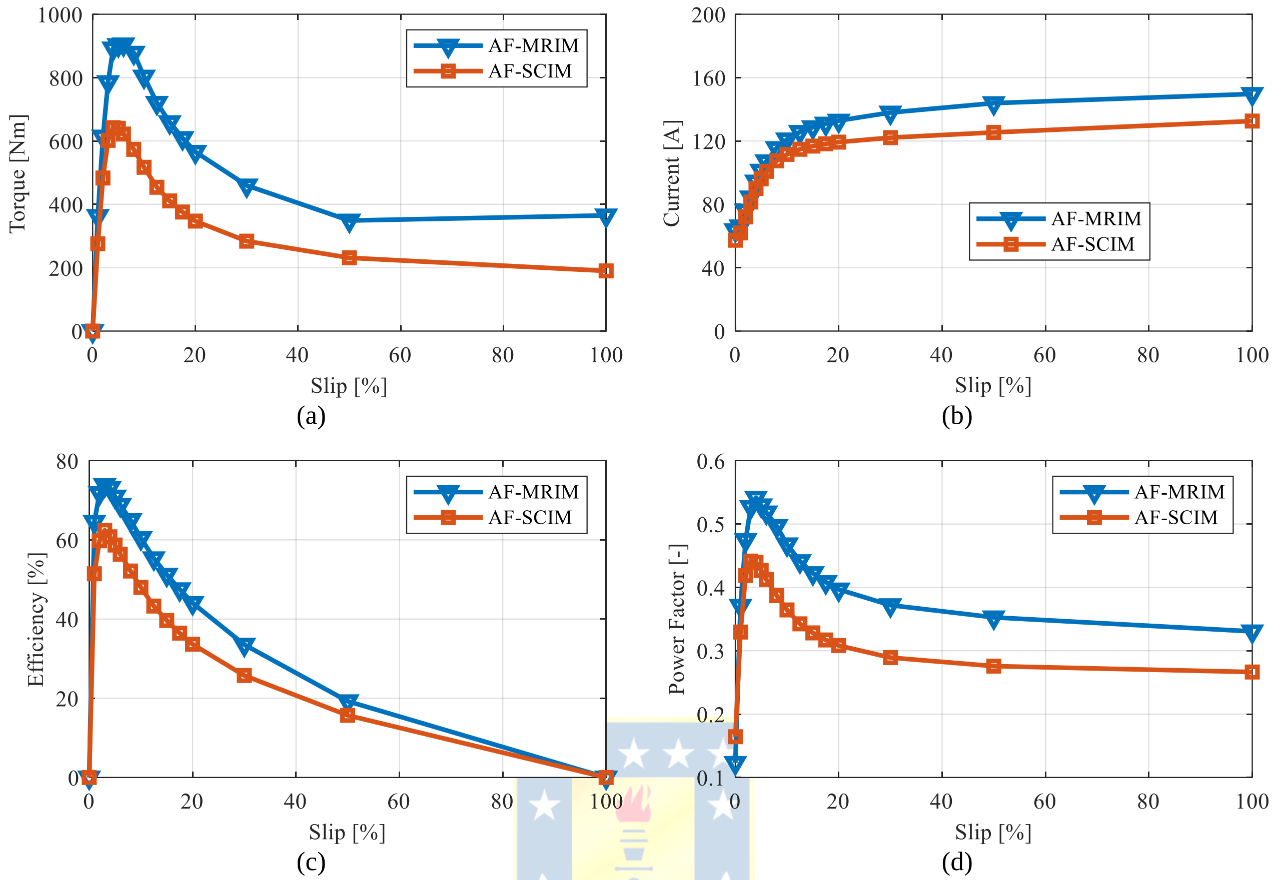

Fig. 5.4 Comparison of the performance of the initial AF-MRIM design vs an equivalent AF-SCIM with $h_{s0} = 0$.
(a) Electromagnetic torque. (b) RMS value of stator line current. (c) Efficiency. (d) Power factor.

5.3. Competitivity of AF-MRIM: Comparison with conventional topologies at 250 rpm

To compare the proposed AF-MRIM design for low-speed operation with different conventional topologies, three well-known radial topologies are considered: RF-SCIM, RF-PMSM and RF-SynRM. To this end, the following steps are considered:

- Optimizing the AF-MRIM under volume and current density constraints, aiming at maximizing torque, power factor and efficiency to operate at ~250 rpm.
- Optimizing a radial RF-PMSM, a RF-SCIM, and a RF-SynRM under the same volume and current density limitations, aiming to maximize performance at ~250 rpm.
- Conducting UUM statistical assessment on all four machines and extending robustness evaluation to non-UUM for the synchronous machines.

- Comparing deterministic performance indicators such us electromagnetic torque, efficiency, power factor, and torque density, along with robust design indices across the four topologies.

5.3.1 Optimizing an assessing an AF-MRIM aiming for ~250 rpm

The optimization of the AF-MRIM for operation at 250 rpm was performed through initial sizing, followed by further refinement using the 2D PMS model, detailed in Section 3.3.1 and Section 3.4.3. The main data of the resulting 24-pole MRIM can be found in Table C.1 in Annex C, while Fig. 5.5 illustrates the machine's geometry.

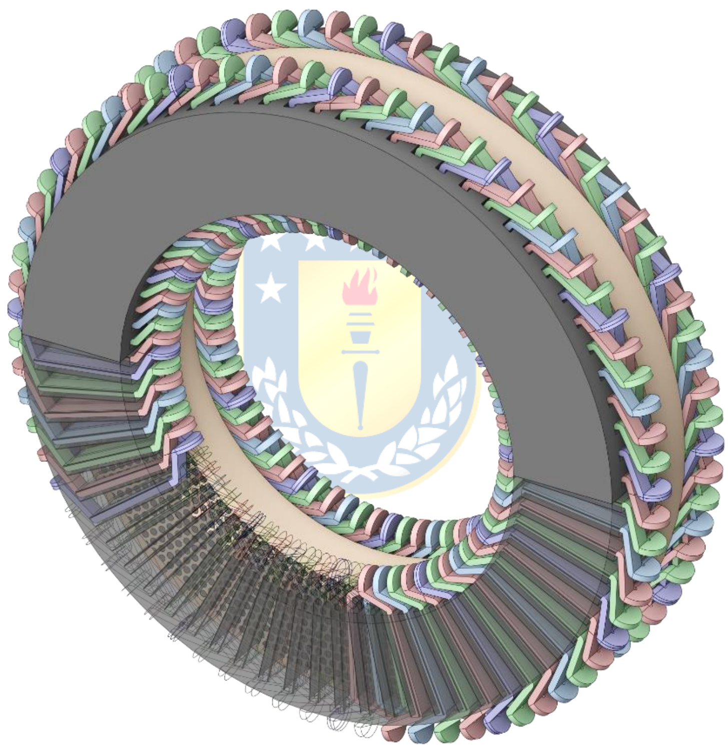

Fig. 5.5 Schematic of the best 24-pole MRIM design obtained from multi-objective optimization.

The performance of the machine, estimated using the 3D full model, is summarized in Table 5.1. To assess design robustness, a tolerance analysis using a UUM approach was performed on the optimized 24-pole MRIM. This analysis focused on the most sensitive dimensional parameters disclosed in Section 3.5: airgap length, rotor height and stator slot height. A statistical analysis involving 2000 machines, each subject to Gaussian-distributed tolerances, was performed using the 2D PMS model. The findings are detailed in Fig. 5.6.

Table 5.1 Performance ratings of optimized 24-pole AF-MRIM

Parameter	Symbol	Value
Rated current density	J_{rated}	$3.0\ A/mm^2$
Overload current density	J_o	$4.8\ A/mm^2$
Rated slip	s_r	2 %
Overload slip	s_o	6 %
Rated mean torque	T_r	881.4 Nm
Rated torque ripple	$T_{r_{rp}}$	11.3 %
Starting torque	T_{stall}	621.6 Nm
Overload mean torque	$T_{o_{mean}}$	1616.1 Nm
Overload torque ripple	$T_{o_{rp}}$	21.2%
Rated efficiency	η_r	84.8 %
Rated power factor	$\cos\phi_r$	0.69
Overload efficiency	η_o	77.1 %
Overload power factor	$\cos\phi_o$	0.67

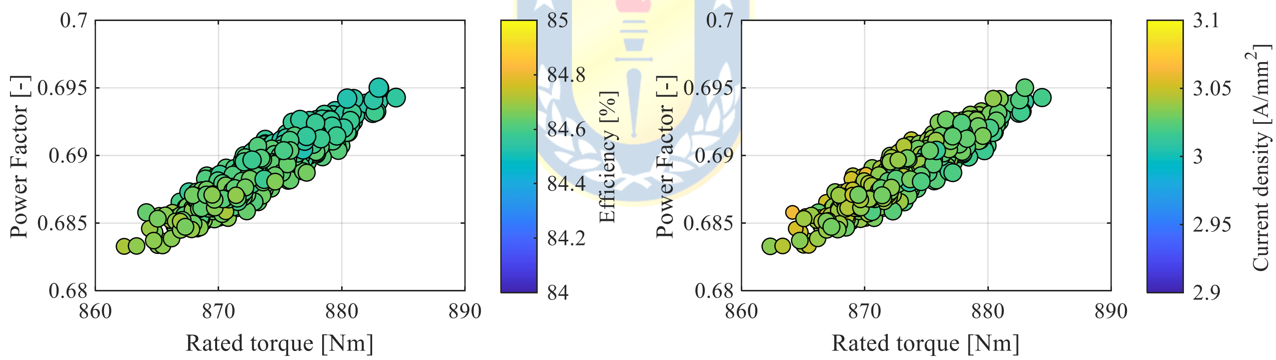

(a) (b)

Fig. 5.6 Performance indices of a representative set of AF-MRIM designs to assess manufacturing tolerances. (a) Rated torque, power factor and efficiency are presented; (b) Rated torque, power factor and current density are presented.

From the obtained data, the standard deviation and median of each performance indicator were calculated. Additionally, a MOGA optimization was performed to identify the worst-case design within the tolerance range of laser cutting and CNC steel punching (0.1 mm), utilizing the 2D PMS model. The results, detailed in Table 5.2, illustrate the robustness of the optimized 24-pole MRIM design. Notably, the statistical indicators in Table 5.2 demonstrate a robust design: response: the standard deviation of mean torque among the representative faulty machines is 0.4% of the faultless value, and the worst torque ripple remains below 15%.

Table 5.2 Design robustness indicators of 24-pole AF-MRIM

Quantity	Symbol	Indicator	Value	Unit
Mean torque	$\overline{T}_{\mathrm{m}}$	Median	877.6	Nm
	$\sigma_{\mathrm{T_m}}$	Standard deviation	3.4	Nm
	$T_{\mathrm{m},w}$	Rating of worst design	855.3	Nm
Torque ripple	$\overline{T}_{\mathrm{rp}}$	Median	11.7	%
	$\sigma_{\mathrm{T_{rp}}}$	Standard deviation	0.2	%
	$T_{\mathrm{rp},w}$	Rating of worst design	14.3	%
Efficiency	$\overline{\eta}$	Median	84.6	%
	σ_{η}	Standard deviation	0.01	%
	η_{w}	Rating of worst design	83.1	%
Power factor	$\overline{PF}$	Median	0.689	-
	σ_{PF}	Standard deviation	0.002	-
	PF_{w}	Rating of worst design	0.678	-
Slot current density	$\overline{J}$	Median	3.03	A/mm^2
	σ_{J}	Standard deviation	0.01	A/mm^2
	J_{w}	Rating of worst design	3.11	A/mm^2

It should be noted that even in the presence of airgap dimensional deviations, both power factor and efficiency exhibit robust responses within expected tolerances, showing standard deviation values of less than 0.2%. Moreover, the median values of the dataset closely approximate those of the faultless design, with variations under 0.4% across all performance indices. Since it is of interest to disclose the robustness of the design, it is suggested to represent machine performance using the dataset median. Also, it is advisable to exhibit the lower and upper performance boundaries, represented by three times the standard deviation, including more than 95% of the machine specimens. Further discussion on these results is presented in Section 5.3.5.

5.3.2 Optimizing an assessing a SCIM aiming for ~250 rpm

Using the generalized torque relation for common cylindrical machines derived from airgap magnetic field energy [59], the initial outer diameter can be chosen based on:

$$\mathrm{OD} \cong \left(4\sqrt{2\frac{\mathrm{P}}{\omega}\frac{1}{\pi\,\alpha}\frac{\mathrm{p}}{A\,\mathrm{B_{g1}}\mathrm{k_{w1}}}}\right)^{\frac{1}{3}}, \tag{5.1}$$

The initial output power selected was 20 HP, in order to align with the initial objectives of the AF-MRIM. Magnetic and electric loading parameters were chosen based on guidelines for air-cooled machines [59]. For the RF-SCIM, a combination of 72 stator slots and 96 rotor slots was chosen, as it is recommended for high-pole count IMs [96]. The main geometric constraint for electromagnetic optimization was maintaining the same volume as the AF-MRIM (~0.077 m^3) to ensure a fair comparison. The optimization problem was devised with specific geometry boundaries to explore designs within practical standards:

- Aspect ratio: 0.4-0.8.
- Back iron to stator stack ratio: 0.3-0.6.
- Shaft to rotor ratio: 0.3-0.6.

The optimization process was conducted using the MOGA within the ANSYS commercial software package. Initial population consisted of 150 machine specimens, which progressed through a maximum of 35 iterations. 100 designs were analyzed per iteration, and the analysis converged after 1807 evaluations. The evolutionary progress of the optimization is illustrated in Fig. 5.7. Detailed specifications of the resulting 24-pole SCIM are provided in Table C.2 in Annex C, and the machine's geometry is depicted in Fig. 5.8. In turn, the performance of the machine is presented in Table 5.3.

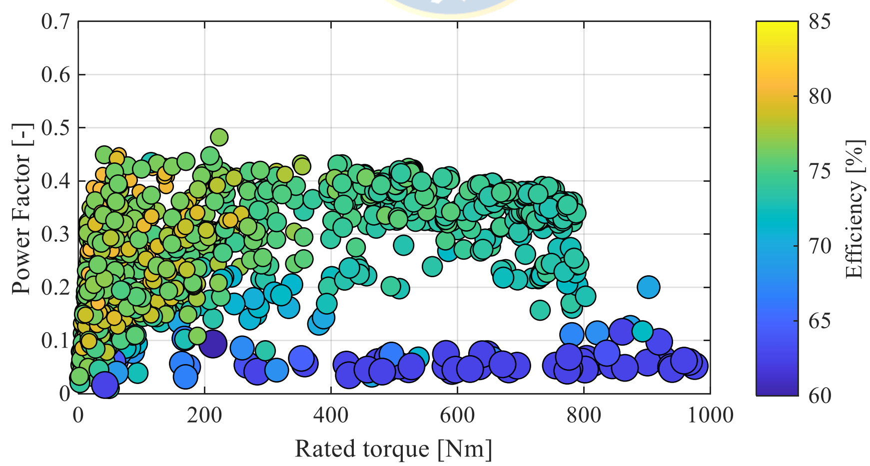

Fig. 5.7 Evolution of SCIM specimens seeking maximum torque, efficiency, and power factor, whilst minimizing current density.

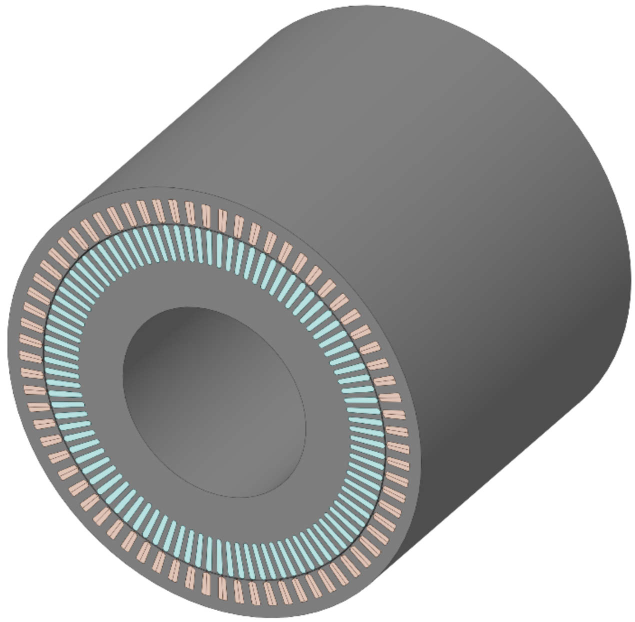

Fig. 5.8 Sketch of the best 24-pole SCIM design obtained from multi-objective optimization.

To assess the design robustness, an UUM tolerance analysis was performed on the optimized 24-pole SCIM, considering the most sensitive dimensional parameters found after an individually assessed sensitivity analysis: airgap length, rotor bar depth and stator slot height. A statistical analysis involving 2000 machines, each subject to Gaussian-distributed tolerances, was performed using a simplified 2D FE model. The findings of this assessment are detailed in Fig. 5.9.

Table 5.3 Performance ratings of optimized 24-pole RF-SCIM

Parameter	Symbol	Value
Rated current density	J_n	$3.0\ \mathrm{A/mm^2}$
Rated slip	s_r	2 %
Rated mean torque	$T_{n_{mean}}$	750.7 Nm
Rated torque ripple	$T_{n_{rp}}$	13.3 %
Rated power factor	$\cos\phi_r$	0.39
Rated efficiency	η_r	78.0 %
Overload mean torque	$T_{o_{mean}}$	1460.8 Nm
Overload torque ripple	$T_{o_{rp}}$	20.1%
Overload power factor	$\cos\phi_o$	0.49
Overload efficiency	η_o	66.3 %
Starting torque	T_s	663.2 Nm

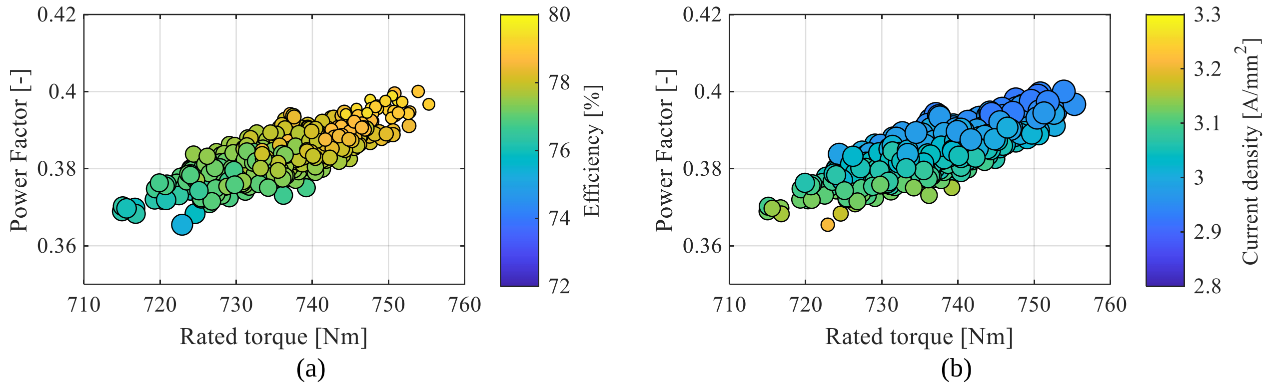

Fig. 5.9 Performance indices of a representative set of RF-SCIM designs to assess manufacturing tolerances. (a) Rated torque, power factor and efficiency are presented; (b) Rated torque, power factor and current density are presented.

Based on results of the statistical analysis, the standard deviation and median of each performance indicator was calculated. Additionally, a MOGA optimization was performed to obtain the worst-case design within typical tolerances of laser cutting and CNC steel punching. All results are summarized in Table 5.4, showing the robustness of the optimized 24-pole RF-SCIM.

Table 5.4 Design robustness indicators of 24-pole RF-SCIM

Quantity	Symbol	Indicator	Value	Unit
Mean torque	$\overline{T}_{\mathrm{m}}$	Median	736.7	Nm
	$\sigma_{\mathrm{T_m}}$	Standard deviation	6.6	Nm
	$T_{\mathrm{m},w}$	Rating of worst design	686.4	Nm
Torque ripple	$\overline{T}_{\mathrm{rp}}$	Median	15.5	%
	$\sigma_{\mathrm{T_{rp}}}$	Standard deviation	1.1	%
	$T_{\mathrm{rp},w}$	Rating of worst design	20.3	%
Efficiency	$\overline{\eta}$	Median	77.8	%
	σ_{η}	Standard deviation	0.63	%
	η_{w}	Rating of worst design	74.3	%
Power factor	$\overline{PF}$	Median	0.383	-
	σ_{PF}	Standard deviation	0.005	-
	PF_w	Rating of worst design	0.357	-
Slot current density	$\overline{J}$	Median	3.03	A/mm^2
	σ_J	Standard deviation	0.04	A/mm^2
	J_w	Rating of worst design	3.25	A/mm^2

Discussion on these results is presented in Section 5.3.5.

5.3.3 *Optimizing an assessing a SynRM aiming for 250 rpm*

Similar to the IM optimization, the main geometric constraint for the SynRM design is to maintain a comparable overall volume to that of the AF-MRIM. The optimization problem was set with the same geometry restrictions as for the SCIM, with an additional specific constraint relevant to SynRMs [78]: the reluctance insulation ratio, explored within the range 0.3 to 0.6.

The initial positions and the thicknesses of the flux barriers were fixed according to the method defined in [97]. The positions of the flux barriers along the airgap, illustrated in Fig. 5.10, were determined by:

$$\alpha = \frac{180}{2p}\frac{1}{b+1}. \tag{5.2}$$

Considering rotor flux barriers of uniform width, their initial width calculation, accounting for the effect of stator teeth width, is given by [97]:

$$h_c = \frac{h_{tq} - b_{ts}(b-1)}{n_l}, \tag{5.3}$$

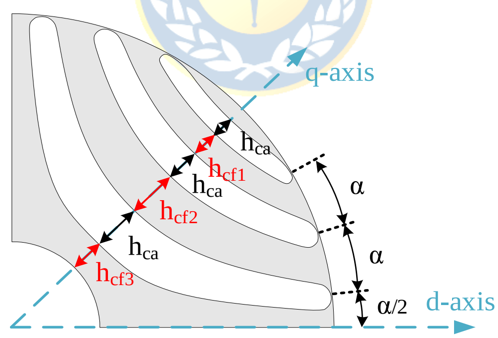

Fig. 5.10 Sketch of dimensional parameters of a SynRM rotor.

The width of the rotor flux carriers (ferromagnetic steel) matches that of the stator teeth. To maintain consistency with the proposed AF-MRIM, a stator configuration with 72 slots was chosen. The optimal number of flux barriers is determined based on the number of stator slots. For example, while some authors advise against using more than three flux barriers in a 36-slot machine, higher stator slot counts allow the adoption of four or more flux barriers per pole [80],[98]. Accordingly, a configuration with four flux barriers per pole and three-phase double-layer distributed windings was selected. In turn, the ferromagnetic material used in both the stator and rotor cores is Cogent Power M235- 35A.

Objective function was set to maximize power factor, average torque and efficiency. The optimization was implemented complementing optimization tools of ANSYS Workbench and embedded ANSYS Electronics Desktop simulations, using a MOGA approach. The process starts with an initial number of 150 samples and proceeded through a maximum of 35 iterations; 100 designs were analyzed per iteration, converging after 1426 evaluations. The evolutionary progress of SynRM specimens is presented in Fig. 5.11.

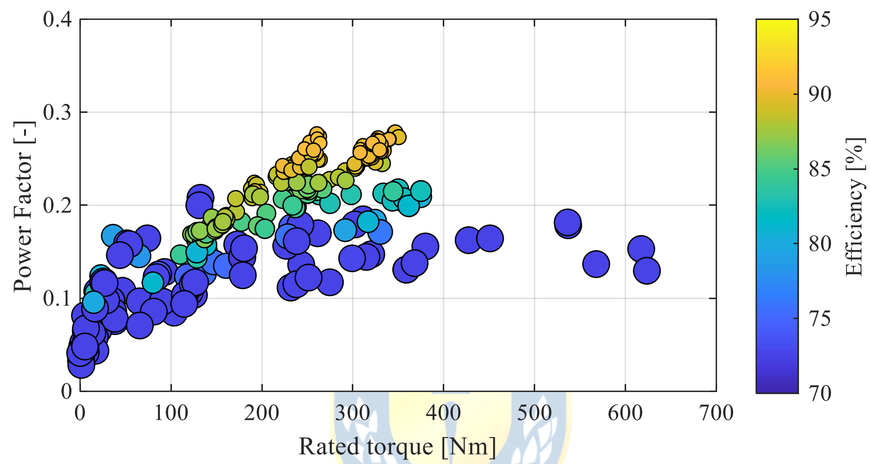

Fig. 5.11 Evolution of RF-SynRM specimens seeking maximum torque, efficiency, and power factor, whilst minimizing current density.

Detailed specifications of the resulting 24-pole SynRM are provided in Table C.3 in Annex C, and the machine's geometry is depicted in Fig. 5.12. The performance of the machine is summarized in Table 5.5.

Table 5.5 Performance ratings of the optimized 24-pole RF-SynRM

Parameter	Symbol	Value
Rated current density	J_n	$3.0\ A/mm^2$
Rated mean torque	T_{n_mean}	335.1 Nm
Rated torque ripple	T_{n_rp}	44.2 %
Rated efficiency	η_r	92.6 %
Rated power factor	$\cos\phi_r$	0.27

To evaluate the design robustness, an UUM tolerance analysis was conducted on the optimized 24-pole SynRM, taking into account dimensional parameters with the most sensitiveness, found after an individual sensitivity analysis: airgap length and the length of the tangential bridge closest to the airgap. To this end, a statistical analysis of 2000 machines following a Gaussian distribution of tolerances was carried out using a 2D simplified FE model. The findings of this analysis are presented in Fig. 5.13.

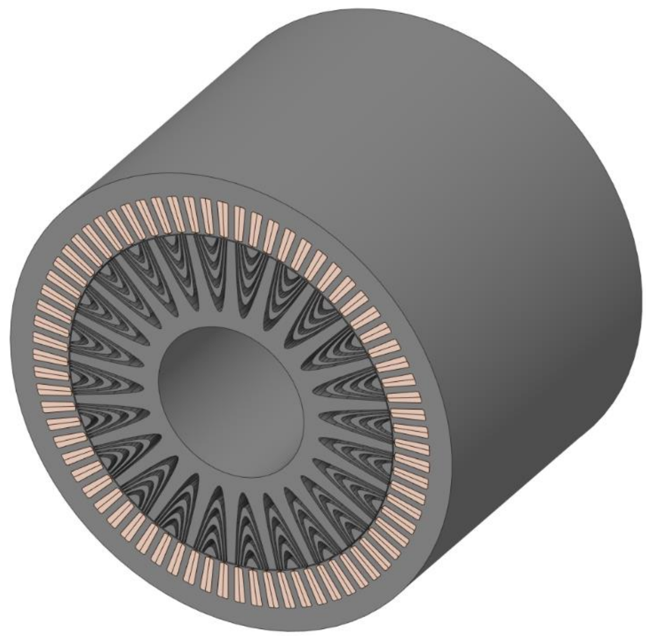

Fig. 5.12 Sketch of the best 24-pole SynRM design obtained from multi-objective optimization.

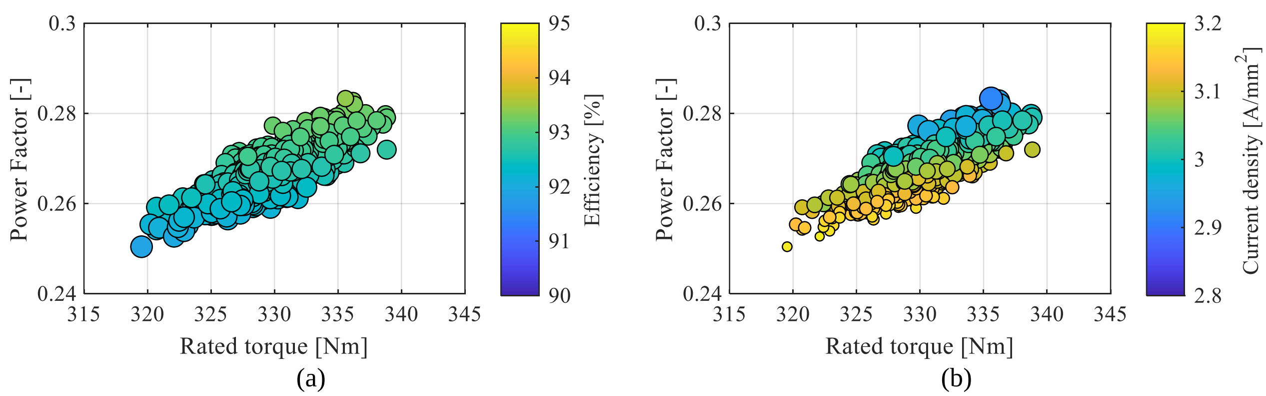

Fig. 5.13 Performance indices of a representative set of SynRM designs to assess manufacturing tolerances.
(a) Rated torque, power factor and efficiency; (b) Rated torque, power factor and current density.

From the obtained data, the standard deviation and median of each performance indicator was extracted. Additionally, a MOGA optimization was performed to obtain a worst design within typical tolerances of laser cutting and CNC steel punching. All results are summarized in Table 5.6, which accounts for the robustness of the optimized SynRM design.

Table 5.6 Design robustness indicators of 24-pole SynRM

Quantity	Symbol	Indicator	Value	Unit
Mean torque	$\overline{T}_{\mathrm{m}}$	Median	330.2	Nm
	$\sigma_{\mathrm{T_m}}$	Standard deviation	3.1	Nm
	$T_{\mathrm{m},w}$	Rating of worst design	262.1	Nm
Torque ripple	$\overline{T}_{\mathrm{rp}}$	Median	46.1	%
	$\sigma_{\mathrm{T_{rp}}}$	Standard deviation	0.6	%
	$T_{\mathrm{rp},w}$	Rating of worst design	54.9	%
Efficiency	$\overline{\eta}$	Median	92.6	%
	σ_{η}	Standard deviation	0.23	%
	η_{w}	Rating of worst design	89.7	%
Power factor	$\overline{PF}$	Median	0.27	-
	σ_{PF}	Standard deviation	0.005	-
	PF_w	Rating of worst design	0.22	-
Slot current density	$\overline{J}$	Median	3.00	A/mm^2
	σ_J	Standard deviation	0.04	A/mm^2
	J_w	Rating of worst design	3.16	A/mm^2

Additionally, a non-UUM assessment of torque waveform was conducted, based on the methodology described in Section 4.4.3. This assessment involved a statistical analysis of 144.000 designs incorporating parameter uncertainties. The positional parameters of the barriers were subjected to manufacturing tolerances following a uniform distribution with 5 tolerance steps ($F = 4$). The tolerance range for dimensional parameters was set from $-1°$ to $+1°$. The summarized results of this evaluation are presented in Table 5.7.

Table 5.7 Torque robustness indicators of 24-pole SynRM following a non-UUM approach

Quantity	Symbol	Indicator	Value	Unit
Mean torque	$\overline{T}_{\mathrm{m}}$	Median	330.6	Nm
	$\sigma_{\mathrm{T_m}}$	Standard deviation	3.7	Nm
Torque ripple	$\overline{T}_{\mathrm{rp}}$	Median	45.6	%
	$\sigma_{\mathrm{T_{rp}}}$	Standard deviation	0.5	%

Table 5.7 reveals that the non-UUM assessment yields no significant differences compared to the UUM results. Interestingly, the non-UUM findings align more closely with the faultless design, suggesting potential performance improvements when adopting asymmetrical rotor barriers [100].

Nonetheless, this difference is not statistically significant. The proposed SynRM exhibits robust torque response even in the presence of typical dimensional uncertainties, consistent with previous findings reported in [74]. In this regard, the non-UUM tools developed in this thesis could be valuable for refining designs to explore promising asymmetrical configurations rather than for conducting tolerance analyses. For a detailed comparison refer to Section 5.3.5 where these results are further discussed.

5.3.4 Optimizing an assessing a PMSM aiming for 250 rpm

Based on the outer diameter estimated by (5.1), an optimization problem was formulated for a 27-slot 24-pole TCW-PMSM. This specific slot/pole combination was chose due to its potential to minimize cogging torque and provide good torque density, benefiting from the close alignment between the number of poles and slots, as well as from the winding arrangement [101]. The optimization was constrained by geometric boundaries described below, adhering to standard design criteria:

- Arc-to-pole ratio: 0.6-0.9.
- Aspect ratio: 0.35-0.65.
- Number of layer conductors: 4-20.
- Magnet height to outer diameter ratio: 2-8%
- Tooth width to outer diameter ratio: 4-12%
- Slot height to outer diameter ratio: 1-25%

Objective function was set to maximize power factor, average torque and efficiency. The optimization was implemented complementing optimization tools of ANSYS Workbench and embedded ANSYS Electronics Desktop simulations, using a MOGA approach. The process starts with an initial number of 150 samples and proceeded through a maximum of 35 iterations; 100 designs were analyzed per iteration, converging after 631 evaluations. The evolutionary progress of PMSM specimens is presented in Fig. 5.14. The main data of the resulting 24-pole TCW-PMSM, depicted in Fig. 5.15, is presented in Table C.4 in Annex C, and Table 5.8 summarizes obtained performance.

To assess the design robustness, an UUM tolerance analysis was performed on the optimized 24-pole PMSM, considering the most sensitive dimensional parameters found after an individually assessed sensitivity analysis: airgap length, tooth-tip dimensions and magnet remanence. A statistical analysis involving 2000 machines, each subject to Gaussian-distributed tolerances, was performed using a simplified 2D FE model. The findings of this assessment are detailed in Fig. 5.16.

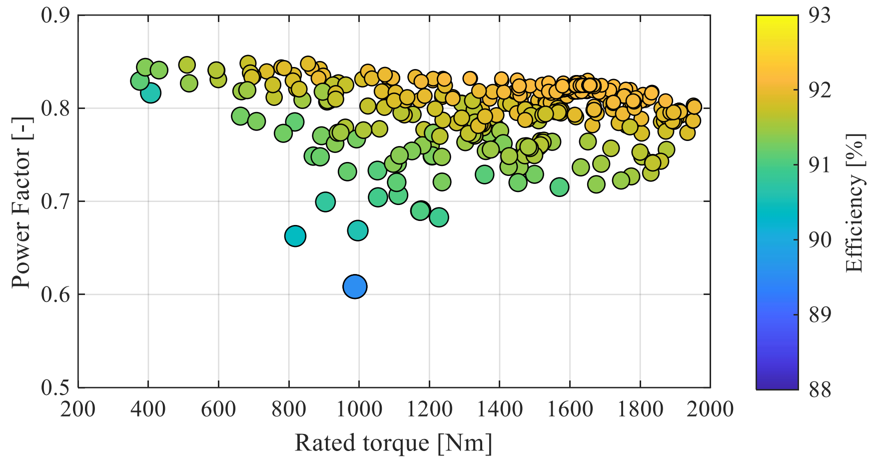

Fig. 5.14 Evolution of RF-TCW-PMSM specimens seeking maximum torque, efficiency, and power factor, whilst minimizing current density.

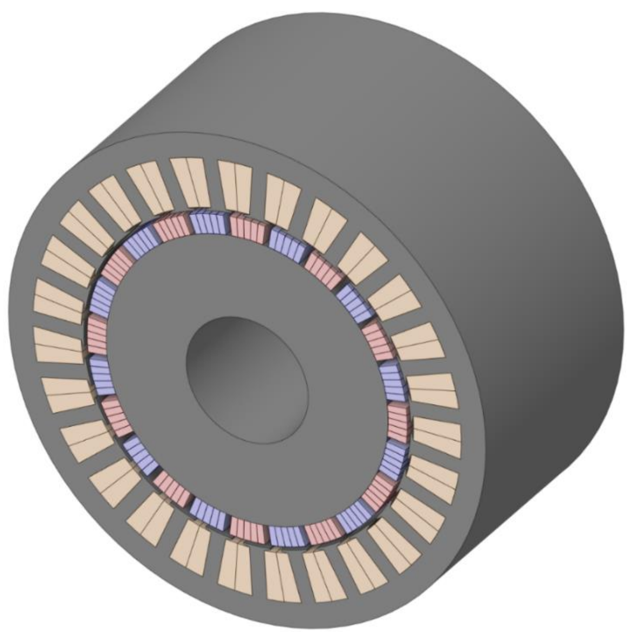

Fig. 5.15 Sketch of the best 24-pole RF-TCW-PMSM design obtained from multi-objective optimization.

Table 5.8 Performance ratings of optimized 24-pole RF-TCW-PMSM

Parameter	Symbol	Value
Rated current density	$\mathrm{J_n}$	$3.0\ \mathrm{A/mm^2}$
Rated mean torque	$\mathrm{T_{r_{mean}}}$	1737.1 Nm
Rated torque ripple	$\mathrm{T_{r_{rp}}}$	4.7 %
Rated efficiency	η_r	92.4 %
Rated power factor	$\cos\phi_r$	0.80
Phase Back-emf	$\mathrm{V_{ind}}$	220 [V]

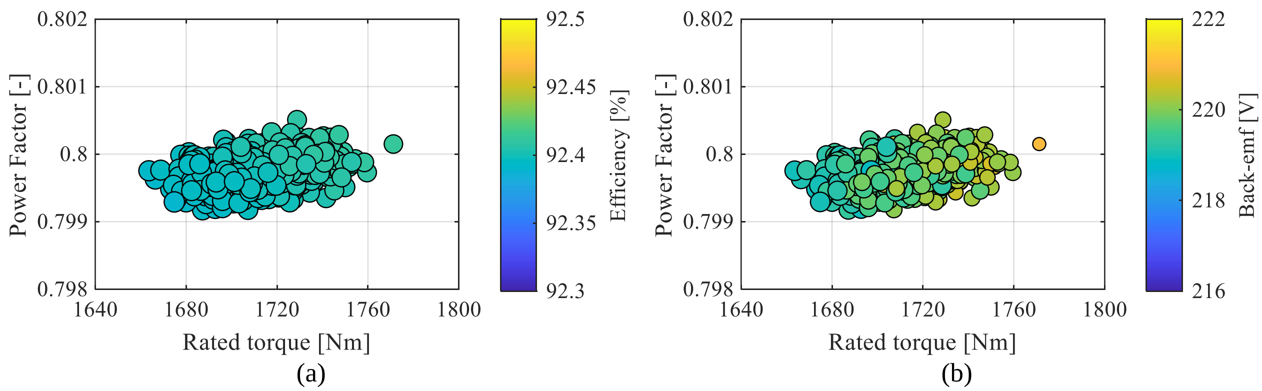

Fig. 5.16 Performance indices of a representative set of RF-PMSM designs to assess manufacturing tolerances. (a) Rated torque, power factor and efficiency are presented; (b) Rated torque, power factor and current density are presented.

Based on results of the statistical analysis, the standard deviation and median of each performance indicator was calculated. Additionally, a MOGA optimization was performed to obtain the worst-case design within typical tolerances of laser cutting and CNC steel punching. All results are summarized in Table 5.9, showing the robustness of the optimized 24-pole RF-PMSM.

Table 5.9 Design robustness indicators of 24-pole PMSM

Quantity	Symbol	Indicator	Value	Unit
Mean torque	$\overline{T}_{\mathrm{m}}$	Median	1720.6	Nm
	$\sigma_{\mathrm{T_m}}$	Standard deviation	16.7	Nm
	$T_{\mathrm{m},w}$	Rating of worst design	1520.2	Nm
Torque ripple	$\overline{T}_{\mathrm{rp}}$	Median	5.4	%
	$\sigma_{\mathrm{T_{rp}}}$	Standard deviation	0.4	%
	$T_{\mathrm{rp},w}$	Rating of worst design	8.7	%
Efficiency	$\overline{\eta}$	Median	92.4	%
	σ_{η}	Standard deviation	0.00	%
	η_{w}	Rating of worst design	92.1	%
Power factor	$\overline{PF}$	Median	0.80	-
	σ_{PF}	Standard deviation	0.000	-
	PF_{w}	Rating of worst design	0.79	-
Back-emf	$\overline{V}_{\mathrm{ind}}$	Median	220.0	V
	$\sigma_{V_{\mathrm{ind}}}$	Standard deviation	0.38	V
	$V_{\mathrm{ind,w}}$	Rating of worst design	217.6	V

Additionally, a non-UUM assessment of torque waveform was carried out, using the methodology described in Section 4.4.4. This evaluation involved a statistical analysis of 54.000 designs with parameter uncertainties. Design parameters were subjected to manufacturing tolerances following a uniform distribution with 5 tolerance steps ($F = 4$). The tolerance range for dimensional parameters was set from -0.1mm to 0.1mm, and remanence varied from -5% to 5%. The summarized results of this evaluation are presented in Table 5.10.

Table 5.10 Design robustness indicators of 24-pole PMSM from a non-UUM approach

Quantity	Symbol	Indicator	Value	Unit
Mean torque	$\overline{T}_{\mathrm{m}}$	Median	1732.8	Nm
	$\sigma_{\mathrm{T_m}}$	Standard deviation	20.1	Nm
Torque ripple	$\overline{T}_{\mathrm{rp}}$	Median	7.1	%
	$\sigma_{\mathrm{T_{rp}}}$	Standard deviation	0.9	%

Comparing Table 5.9 and Table 5.10 reveals no significant differences between the UUM and non-UUM approaches in terms of mean torque, despite variations in stator and rotor periodicities. Similar conclusions were reported in [73] for an AF-PMSM, where mean torque and back-emf were unaffected by manufacturing tolerances when using a non-UUM approach. Instead, mean torque varied primarily with airgap length and core saturation, showing consistent outcomes between UUM and non-UUM assessments. For the airgap length, tolerances were modeled using a Gaussian distribution centered on the nominal value, resulting in negligible shifts in the torque median compared to that of a flawless machine. This stems from UUM and non-UUM approaches sharing the same statistical definition regarding airgap length.

Nonetheless, significant median ripple torque increases were observed in the non-UUM assessment, attributed to variations in stator teeth periodicity, geometric changes, and tooth-tip saturation, as detailed in [41], [73], [102]-[103]. These variations, both positive and negative, mainly increased cogging torque, with only a few tolerance combinations reducing it. Consequently, this led to a notable penalization of the overall cogging torque of the machine specimens, in agreement with the obtained results. In this case, the difference between expected ripple torque and flawless ripple torque is 45%. Further discussion of the robustness results for the PMSM can be found in Section 5.3.5.

5.3.5 *Comparison and discussion*

An optimization and robustness assessment is conducted for the AF-MRIM, RF-SCIM, RF-SynRM and RF-PMSM operating at 380V, 50 Hz, 250 rpm, and 3 A/mm^2, focusing on their suitability for LSHT applications. Table 5.11 provides a summary of the main data of these selected topologies. The comparison includes the weight of active components, calculating by estimating the mass of stator and rotor iron cores, copper coils covering both the active and end-winding regions, rotor cage for the SCIM, steel rotor support, and the portion of the steel axis within the overall axial length of the machine's active components. Fig. 5.17 illustrates the components considered for the AF-MRIM as an example.

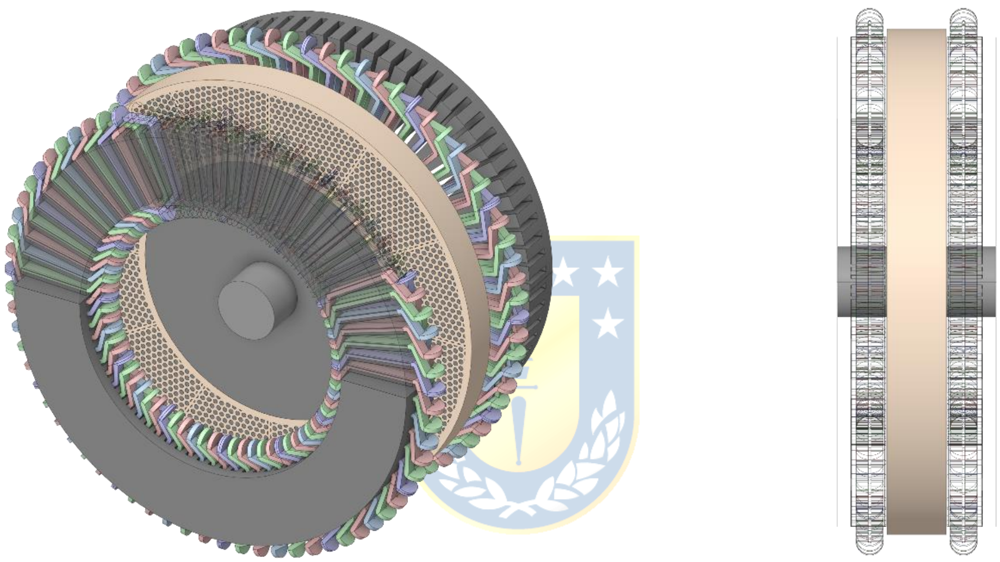

(a) (b)

Fig. 5.17 Considered components for estimating the weight of active parts.
(a) Expanded view; (b) lateral view.

Table 5.11 Main data comparison of optimized 24-pole LSHT machines

Parameter	Symbol	RF-SynRM	RF-SCIM	AF-MRIM	RF-PMSM
Air-gap length	g	1.2 mm	1.2 mm	2 x 1.5 mm	3.0 mm
Stack length	l_{st}	378.0 mm	421.1 mm	197.8 mm	280.0 mm
Volume	-	$75.4 \cdot 10^6$ mm^3	$75.9 \cdot 10^6$ mm^3	$76.3 \cdot 10^6$ mm^3	$75.1 \cdot 10^6$ mm^3
Weight of active parts	w_{active}	491.0 kg	531.6 kg	426.5 kg	541.7 kg
Number of stator slots	Q_s	72	72	72	27
Number of pole pairs	p	12	12	12	12
Rated speed	n	250 rpm	245 rpm	245 rpm	250 rpm
Frequency	f	50 Hz	50 Hz	50 Hz	50 Hz

The MRIM exhibits the lowest weight of active parts due to its axial-flux stators, which occupy less volume. This contributes to increase torque density, leveraging the inherent advantages of axial-flux topologies. In turn, the optimized RF-SynRM and RF-SCIM feature significantly smaller airgaps, facilitated by precise manufacturing of these radial configurations. Instead, the MR-AFIM requires a larger airgap considering the challenging manufacturing and axial-flux topology: small airgaps in the presence of unavoidable rotor tilt could lead to rotor-stator contact, potentially damaging the stator windings and compromising machine integrity. Similarly, the PMSM also requires a large airgap since its magnets are mounted on the rotor surface, requiring additional space for magnet fixation and precise assembly. Despite these considerations, both the MRIM and the PMSM feature equivalent airgaps, and further design refinements could be made if smaller airgap were practical.

Table 5.12 summarizes the expected rated performance of each topology, based on the median of 2000 representative machine specimens near the final optimized design. Data from Tables Table 5.2, Table 5.4, Table 5.6, Table 5.7, Table 5.9 and Table 5.10 were used for this comparison. UUM results were used for the optimized SynRM, SCIM and MRIM and PMSM for all results, with the exception of torque ripple for the PMSM, which was extracted from the non-UUM assessment. Fig. 5.18 presents the results of Table 5.12 in a bar chart format to facilitate discussion and enhance comparison visualization.

Table 5.12 Comparison of expected rated performance of optimized 24-pole LSHT machines.

Indicator	Symbol	SynRM	RF-SCIM	AF-MRIM	RF-PMSM
Current density	J_r	$3.0\ A/mm^2 \pm 4.0\%$	$3.0\ A/mm^2 \pm 4.0\%$	$3.0\ A/mm^2 \pm 1.0\%$	$3.0\ A/mm^2 \pm 0.5\%$
Mean torque	$T_{m,rated}$	330.2 Nm $\pm$ 2.8%	736.7 Nm $\pm$ 2.7%	877.6 Nm $\pm$ 1.2%	1720.6 Nm$\pm$ 2.9%
Torque density*	$T_{m,density}$	0.67 Nm/kg	1.39 Nm/kg	2.03 Nm/kg	3.18 Nm/kg
Torque ripple	$T_{r_{rp}}$	46.1 % $\pm$ 1.8%	15.5 % $\pm$ 3.3%	11.7 % $\pm$ 0.6%	6.8 %$\pm$ 2.7%
Efficiency	η_r	92.6 % $\pm$ 0.7%	77.8 % $\pm$ 1.9%	84.6% $\pm$ 0.0%	90.4 %$\pm$ 0.0%
Power factor	$\cos\phi_r$	0.27 $\pm$ 4.0%	0.39 $\pm$ 4.0%	0.69 $\pm$ 0.9%	0.80 $\pm$ 0.0%

*Calculation of torque density only takes into account the weight of active parts and the portion of the shaft that is included in the active zone. Once assembled, case, bearings and lid weight should be considered as well.

Table 5.12 highlights that the optimized PMSM exhibits the higher performance among all considered machines, unsurprisingly offering a 50% higher torque capacity than the second-best machine, the AF-MRIM. Nevertheless, the PMSM lacks self-starting capability and relies on precise current control, rendering it unsuitable for direct-drive LSHT applications. Additionally, the selected PMSM does not provide a robust design response in ripple torque, which translates into severe differences between the ideal flawless machine and the expected performance under tight tolerance conditions.

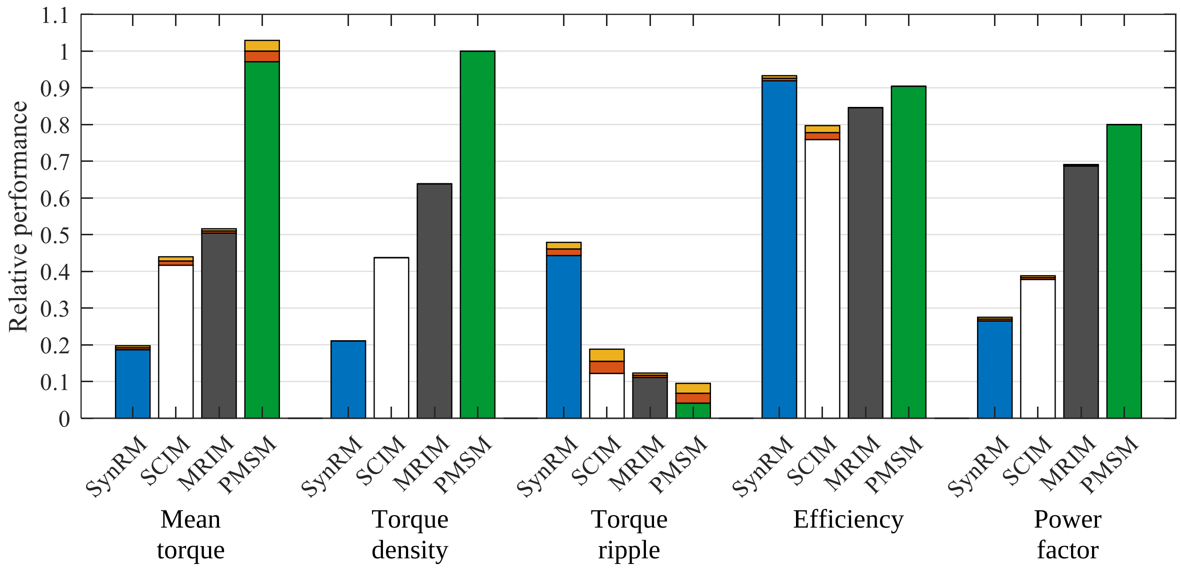

Fig. 5.18 Graphical representation of relative performance obtained by the four optimized 250 rpm LSHT machines. The top of each bar is segmented according to the standard deviation obtained from the robustness assessment.

As expected, the SynRM provides the highest efficiency due to minimal iron core losses, absence of rotor copper or magnet losses, and the use of low-loss ferromagnetic materials. Nonetheless, based on the results from the optimized machine and the evolution of machine specimens previously presented in Fig. 5.13, it is evident that this topology has inherent design limitations that restrict its suitability for LSHT applications. These limitations include an exceptionally low power factor and high torque ripple. Attempts to reduce torque ripple through classical step-skewing further diminish rated torque and power factor, underscoring its lack of competitiveness in these applications.

From Fig. 5.18, it is apparent that among rare-earth-free topologies, the AF-MRIM provides the highest performance. It provides 20% higher torque, 4% lower torque ripple, 7 points higher efficiency, and a substantial 30-point advantage in power factor compared to the next best-performing topology. Its power factor is only 10 points lower than that of the PMSM. Moreover, the MRIM exhibits the highest design robustness among the selected topologies, resulting in minimal deviations between the theoretical performance and actual ratings when the machine is prototyped and assembled under tight tolerances. Comparing with the RF-SCIM, it should be noted that the MRIM achieves its main objective: providing higher torque capacity, significantly improved power factor, reduced torque ripple, and robust design capability. It is interesting to note that the RF-SCIM has rotor continuous skewing with one slot to reduce torque ripple, as the un-skewed machine exhibit ripple exceeding 30% of the mean torque. Despite this effort, the MRIM is able to deliver a lower torque ripple in rated operation.

Table 5.13 presents the performance of each topology under the worst-case scenario, along with the difference compared to the flawless design. It is important to highlight that this scenario represent an extreme case with very low probability of occurrence, aimed at showcasing the lowest performance boundary within typical manufacturing tolerances.

Table 5.13 Comparison of the worst-case scenario of optimized 24-pole LSHT machines considering twice the typical tolerances of laser cutting or CNC steel punching.

Indicator	Symbol	RF-SynRM	RF-SCIM	AF-MRIM	RF-PMSM
Worst expected mean torque	$T_{m,rated}$	262.1 Nm	686.4 Nm	855.3 Nm	1520.2 Nm
Difference from flawless		-21.8 %	-8.6 %	-3.0 %	-12.5 %
Worst expected torque ripple	$T_{r_{rp}}$	54.9 %	20.3 %	14.3 %	8.7 %
Difference from flawless		+24.2%	+52.6%	+22.2 %	+85.1 %
Worst expected efficiency	η_r	93.1 %	74.3 %	83.1%	90.8 %
Difference from flawless		-2.8 %	-4.7 %	-2.0 %	-0.3%
Worst expected power factor	$\cos\phi_r$	0.22	0.36	0.68	0.79
Difference from flawless		-18.5 %	-7.7 %	-1.4 %	-1.3 %

Table 5.13 illustrates that the PMSM continues to offer the best performance among the four selected topologies, providing a robust design response in terms of efficiency and power factor. However, it features nearly double the torque ripple under typical tolerance conditions compared to the flawless design, and a severe 12.5% reduction in mean torque. Detailed evaluation of the design specimens with worst performance reveal that these trend stems from reductions in slot area, an increase in airgap size, and a decrease in magnet remanence. Specifically, the reduction in magnet remanence, within the typical $\pm 5\%$ tolerance provided by manufacturers, is identified as the primary factor contributing to torque reduction, in agreement with findings reported in [73].

In turn, SynRM suffers significant penalties across all performance indices, resulting in a 34% decrease in torque capacity, a 24% increase in torque ripple, and a 19-point drop in power factor. Examination of the worst designs indicates that the increase in airgap length is more severe compared to MRIM and PMSM, accentuating torque and power factor reductions. Additionally, increasing the length of tangential iron bridges due to dimensional variations severely increases flux leakage, reducing the saliency ratio and thus triggering the observed power factor and mean torque reduction.

The optimized RF-SCIM has a relatively robust mean torque response, although significant performance deviations are obtained in terms of efficiency, power factor, and torque ripple. The latter is of concern, since a 50% torque ripple increase is observed in the worst design, reaching 20% of the mean value and raising concerns about vibration and noise. From the analysis of design specimens with highest ripple, it was observed that rotor bar geometry and tooth-tip dimensions are the most significant contributors to torque ripple deviations.

Finally, the AF-MRIM offers the most robust response across mean torque, torque ripple, efficiency and power factor compared to the flawless case. In this sense, the matrix rotor arrangement allows for a robust magnetic electromagnetic response: the use of numerous small iron wires in the rotor means that changes in stator tooth-tip dimensions minimally affect the specific wires conducting flux density lines. Unlike other topologies, the MRIM does not rely on precisely defined paths for flux density, as seen in SynRMs or SCIMs. In this regard, airgap length is the main concern of the AF-MRIM, although no severe deviations of performance ratings are obtained within typical manufacturing tolerances. Consequently, the AF-MRIM configures as a solid rare-earth free alternative for LSHT applications at 250 rpm, in terms of raw performance and design robustness.

5.4. Competitivity of AF-MRIM: Comparison with conventional topologies at 500 rpm

To compare the proposed AF-MRIM design for low-speed 500 rpm operation with different conventional topologies, three well-known radial topologies are considered: RF-SCIM, RF-PMSM and RF-SynRM. To this end, the following steps are considered:

- Optimizing the AF-MRIM under volume and current density constraints, aiming at maximizing torque, power factor and efficiency to operate at ~500 rpm.
- Optimizing a radial RF-PMSM, a RF-SCIM, and a RF-SynRM under the same volume and current density limitations, aiming to maximize performance at ~500 rpm.
- Conducting UUM statistical assessment on all four machines and extending robustness evaluation to non-UUM for the synchronous machines.
- Comparing deterministic performance indicators such us electromagnetic torque, efficiency, power factor, and torque density, along with robust design indices across the four topologies.

5.4.1 *Optimal machines aiming for ~500 rpm*

Following the procedure described in Section 5.3, the selected topologies were optimized, and their robustness was assessed using a UUM approach. The resulting designs are depicted in Fig. 5.19, and detailed data is summarized in Annex C, Section C2.

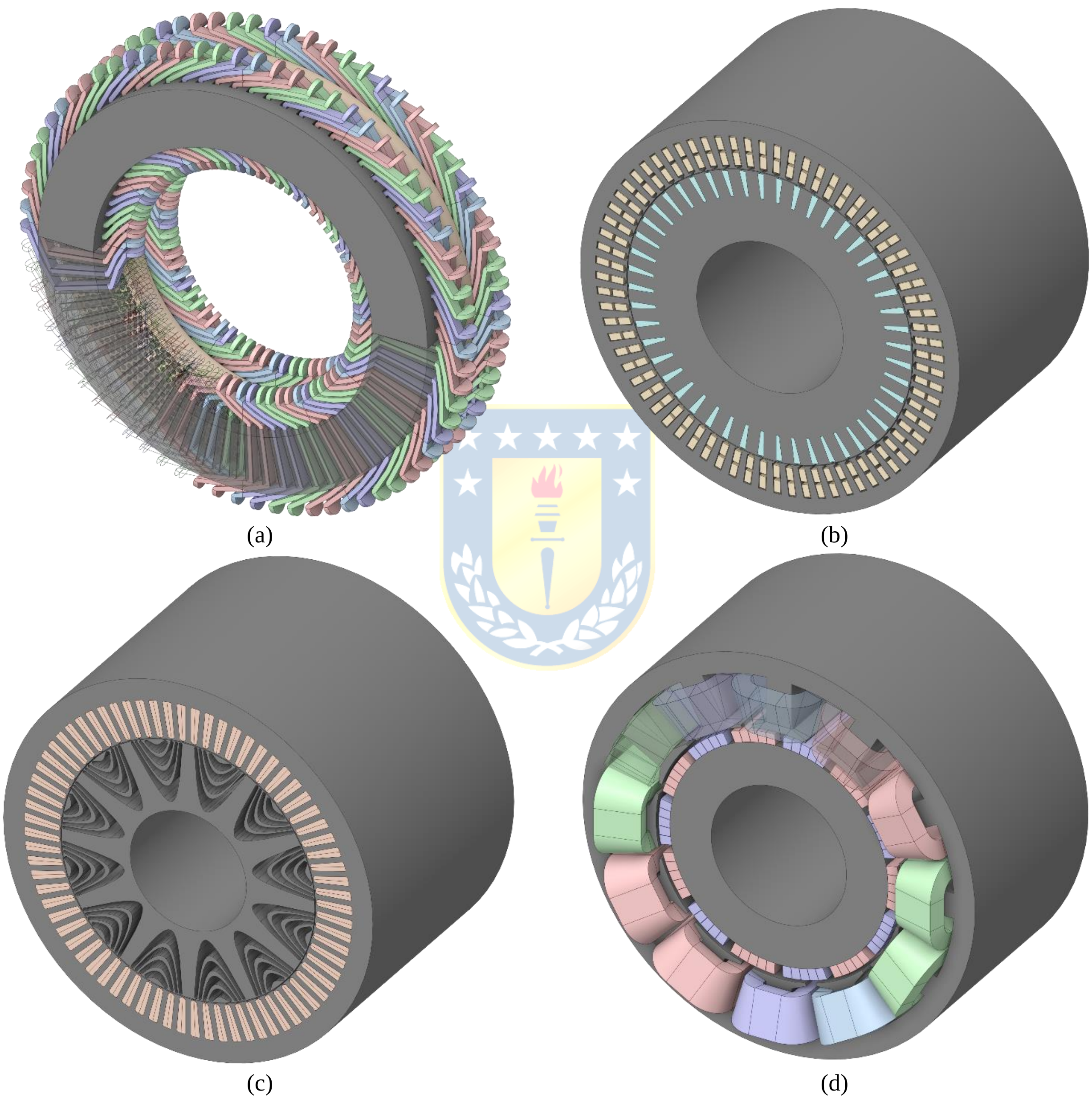

Fig. 5.19 Optimized machines for 500 rpm LSHT applications
(a) 12-pole AF-MRIM, (b) 12-pole RF-SCIM; (c) 12-pole RF-SynRM; (d) 14-pole RF-PMSM.

5.4.2 *Comparison and discussion*

An optimization and robustness assessment is conducted for the AF-MRIM, RF-SCIM, RF-SynRM and RF-PMSM operating at 380V, 50 Hz, 500 rpm, and 3 A/mm^2, focusing on their suitability for LSHT applications. Table 5.14 provides the main data of the selected topologies after optimization.

Table 5.14 Main data comparison of optimized 12-pole LSHT machines

Parameter	Symbol	RF-SynRM	RF-SCIM	AF-MRIM	RF-PMSM
Air-gap length	g	1.2 mm	1.2 mm	2 x 1.5 mm	3.0 mm
Stack length	l_{st}	372.2 mm	336.5 mm	199.0 mm	284.2 mm
Volume of active parts	V_{active}	74.2·10^6 mm^3	75.8·10^6 mm^3	76.2·10^6 mm^3	75.7·10^6 mm^3
Weight of active parts	w_{active}	462.2 kg	541.1 kg	405.6 kg	556.3 kg
Number of stator slots	Q_s	72	72	72	12
Number of rotor slots	Q_r	-	48	-	-
Number of pole pairs	p	6	6	6	7
Rated speed	n	500 rpm	485 rpm	490 rpm	430 rpm
Frequency	f	50 Hz	50 Hz	50 Hz	50 Hz

Similar to the 24-pole study case, the AF-MRIM has the lowest weight of active parts due to its axial-flux stators. The airgap length remains consistent with that of the 24-pole machines, establishing a notable difference between rare earth-free radial-flux topologies and the remainder of designs.

Table 5.15 presents the expected rated performance of each topology, based on the median of 2000 representative designs near the final optimized design. UUM results were used for the optimized SynRM, SCIM and MRIM and PMSM, with the exception of torque ripple for the PMSM, which was extracted from the non-UUM assessment. Fig. 5.20 presents the results of Table 5.15 in a bar chart format to support discussion and for clarity purposes.

Table 5.15 Comparison of expected rated performance of optimized 12-pole LSHT machines.

Indicator	Symbol	SynRM	RF-SCIM	AF-MRIM	RF-PMSM
Current density	J_r	$3.0\ \text{A/mm}^2 \pm 3.0\%$	$3.0\ \text{A/mm}^2 \pm 4.2\%$	$3.0\ \text{A/mm}^2 \pm 1.6\%$	$3.0\ \text{A/mm}^2 \pm 0.6\%$
Mean torque	$T_{m,rated}$	641.6 Nm $\pm$ 2.3%	1035.8 Nm $\pm$ 2.4%	1310.2 Nm $\pm$ 1.5%	2007.8 Nm$\pm$ 3.0%
Torque density*	$T_{m,density}$	1.39 Nm/kg	1.91 Nm/kg	3.23 Nm/kg	3.61 Nm/kg
Torque ripple	$T_{r_{rp}}$	33.6 % $\pm$ 2.1%	27.7 % $\pm$ 3.1%	13.2 % $\pm$ 0.9%	2.6 %$\pm$ 46.1%
Efficiency	η_r	95.5 % $\pm$ 0.4%	90.2 % $\pm$ 1.7%	90.1% $\pm$ 0.2%	96.7 %$\pm$ 0.1%
Power factor	$\cos\phi_r$	0.51 $\pm$ 4.1%	0.68 $\pm$ 2.4%	0.79 $\pm$ 1.2%	0.84 $\pm$ 0.0%

*Calculation of torque density only takes into account the weight of active parts and the portion of the shaft that is included in the active zone. Once assembled, case, bearings and lid weight should be considered as well.

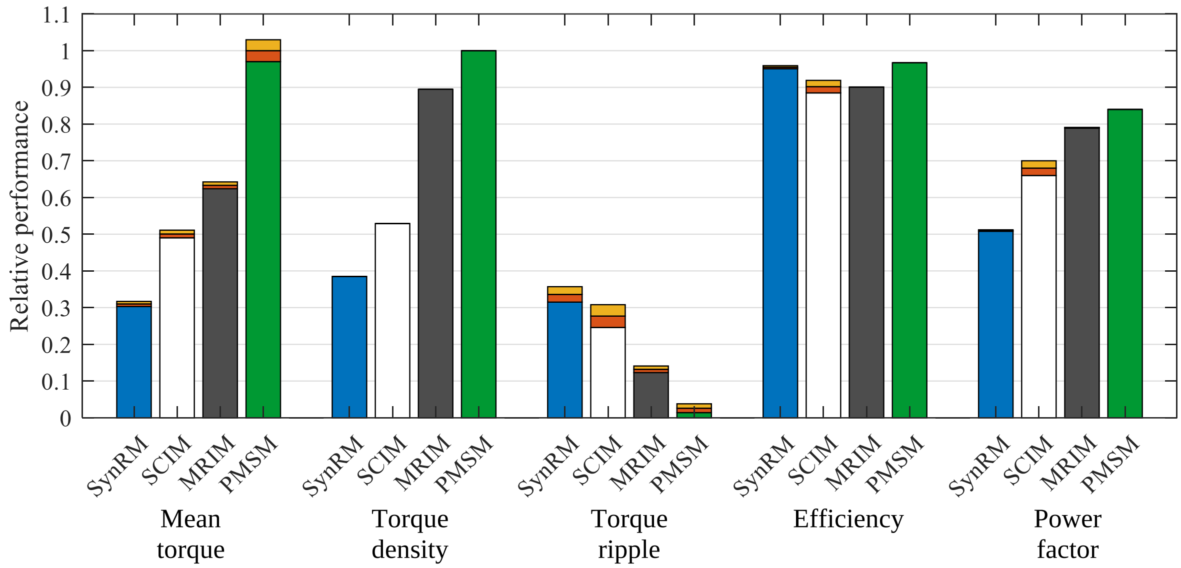

Fig. 5.20 Graphical representation of the relative performance obtained by the four optimized 500 rpm LSHT machines. The top of each bar is segmented according to the standard deviation obtained from the robustness assessment.

From Table 5.15 and Fig. 5.20, it is evident that the optimized 14-pole PMSM once again demonstrates the best performance among all considered machines, providing a 35% higher torque capacity than the second-best machine, the AF-MRIM. It should be noted mentioning that PMSM does not have self-starting capability, and that including PMSMs in the comparison charts aims to illustrate their potential improvements if adopted, although this falls outside the direct-drive scop of this thesis. From Table 5.15, it is apparent that the optimized PMSM does not exhibit robust design response in terms of torque ripple, resulting in significant deviations from the flawless machine under tight tolerances. Nonetheless, the actual torque ripple remains relatively low, making the lack of robustness more of a theoretical concern than a practical issue. This could raise concerns in applications where extremely low torque ripple is crucial, such as in electromobility, which is out of the scope of this work.

From the comparison of Table 5.12 and Table 5.15, SynRM notably improves its performance and approaches that of the RF-SCIM, although it remains the machine with the lowest torque capacity. Nonetheless, the SynRM provides high efficiency. From the results of the optimization process, it is possible to deduce that while the design limitations observed in the 24-pole machine persist in the 12-pole machine, they are somewhat reduced: achieving a low power factor and high torque ripple. None of the SynRM specimens evaluated in the multi-objective optimization achieved a power factor higher than 0.57.

From Fig. 5.18, it is clear that the AF-MRIM and RF-SCIM have similar performance ratings, and that the design advantages provided by the matrix rotor are less pronounced than in the 24-pole machines. Nevertheless, the MRIM still develops superior performance, offering 25% higher torque, 50% lower torque ripple, and a 10-point advantage in power factor compared with the SCIM. Efficiency, on the other hand, is comparable between both designs, and it is conditioned by rotor copper losses. The superiority of the 12-pole AF-MRIM over its SC counterpart mostly lies in reduced torque ripple reduction and robust design response. Once again, the MRIM exhibits the highest design robustness of all the selected topologies, which translates into smaller differences between the projected deterministic performance and the expected ratings post-assembly. Despite the advantages being less pronounced than in the 24-pole case study, the MRIM successfully achieves its main objective: providing higher torque capacity, improved power factor, reduced torque ripple, and providing design robustness.

In Table 5.16, the performance of each topology considering the worst performance scenario, and the difference with respect to the flawless design, is presented. It should be noted that this design is within a parameter range with extremely low probability of occurrence and intends to showcase the lowest performance achievable within typical manufacturing tolerances.

Table 5.16 Comparison of worst performance scenario of optimized 12-pole LSHT machines considering twice the typical tolerances of laser cutting or CNC steel punching.

Indicator	Symbol	RF-SynRM	RF-SCIM	AF-MRIM	RF-PMSM
Worst expected mean torque	$\mathrm{T_{m,rated}}$	629.6 Nm	981.4 Nm	1264.1 Nm	1830.7 Nm
Difference from flawless		-4.7 %	-6.1 %	-4.2 %	-8.8 %
Worst expected torque ripple	$\mathrm{T_{r_{rp}}}$	35.9 %	35.6 %	15.8 %	4.9 %
Difference from flawless		+10.1%	+28.5%	+19.7 %	+188.2 %
Worst expected efficiency	η_r	95.2 %	88.4 %	88.1%	96.4 %
Difference from flawless		-0.5 %	-2.0 %	-2.2 %	-0.3%
Worst expected power factor	$\cos\phi_r$	0.47	0.66	0.77	0.84
Difference from flawless		-7.8 %	-4.3 %	-2.5 %	0.0 %

From Table 5.16, it can be noted that the PM machine develops the best performance among the four selected topologies, demonstrating robust design response in terms of efficiency and power factor. However, worst torque ripple within typical tolerance range is nearly three times that of the faultless design, and a significant 8.8% reduction in mean torque is observed. Analysis of design specimens with worst performance reveal that the observed torque trends are related to reductions in slot area, increased airgap length, and decreased magnet remanence, similar to findings in the 24-pole PMSM (refer to Section 5.3.5).

In turn, SynRM has a relatively robust response across all performance indices, contrasting with the 24-pole variant. Torque capacity decreases by 4.7%, torque ripple increases by 10%, and power drops by 4 points. Examination of the worst designs suggests that dimensional factors contributing to this performance degradation are the same as for the 24-pole machine: the increase in airgap length is proportionally more severe compared to MRIM and PMSM, accentuating torque and power factor reductions. Likewise, increasing the length of tangential iron bridges due to dimensional variations increases flux leakage, reducing the saliency ratio and thus reducing power factor and mean torque. However, the lower pole count of the 12-pole variant cause flux density lines to travel a longer distance through the stator yoke, increasing the distance between the airgap-crossing area of these lines. This diminishes flux leakage and may increase saliency, contributing to improve the machine design robustness.

Similarly to the 24-pole case, the optimized 12-pole RF-SCIM exhibits robust mean torque response, and the main concern is the highly sensitive torque ripple. The worst-case scenario shows a 30% increase in torque ripple, reaching 35.6% of the mean value, potentially raising vibration and noise concerns. It is interesting to note that the RF-SCIM features a continuously skewed rotor structure to reduce its original ripple, which seems to be insufficient to keep the torque ripple within acceptable limits (below 20%)

The MRIM offers a robust response, although it is surpassed by the SynRM in terms of ripple torque deviation. Nonetheless, the flawless torque ripple of the MRIM is significantly lower than the SynRM, providing superior torque quality even under worst-case conditions. As observed in the 24-pole machine, airgap length remains a primary consideration for the AF-MRIM, although no severe deviations in performance ratings occur within typical manufacturing tolerances. Finally, the AF-MRIM presents itself as a dependable rare-earth free alternative for LSHT applications at 500 rpm, offering acceptable performance and design robustness. Significantly lower ripple torque and slightly higher power factor are advantages of the MRIM over the SCIM, at the cost of more complex manufacturing and assembly processes. In this regard, while the adoption of the MRIM for 12-pole direct-drive applications may not be straightforward, it does effectively offer enhanced performance and design robustness.

5.5. Section summary

This section provided a preliminary comparative analysis of the proposed AF-MRIM with an equivalent AF-SCIM, alongside a detailed study comparing it with established machine topologies: direct competitors such as the RF-SCIM, rare-earth free alternatives like SynRMs, and top performers such as PMSMs. To ensure a fair and comprehensive comparison, the proposed topologies were optimized using FE simulations and MOGA, leading to the development of both 24-pole and 12-pole machine designs. From this optimized set, results were computed and compared from both deterministic and robust-design approaches, highlighting the following points:

- Compared to an equivalent AFIM with an unskewed squirrel cage at 250 rpm, the proposed AF-MRIM has superior performance ratings: a 12-point increase in power factor, a 40% boost in torque capacity, and 15-point efficiency improvement.
- When compared to equivalent conventional machines operating at 250 rpm, the proposed AF-MRIM outperforms other rare-earth free topologies but does not reach the performance and torque density of an optimized PMSM. Nonetheless, the MRIM demonstrates superior robustness ratings among the four selected topologies and double the power factor of its radial flux counterpart (the only competitor with self-starting capability). Therefore, adopting the MRIM in 24-pole direct-drive applications is recommended.
- When compared to equivalent conventional machines at ~500 rpm, the proposed AF-MRIM continues to exhibit superior performance among rare-earth free topologies, achieving comparable torque density to the PMSM but with worse power factor and ripple torque. In contrast, the RF-SCIM delivers similar torque output to that of the AF-MRIM but suffers from poorer power factor and higher torque ripple, traded for simpler manufacturing. Hence, while adopting the MRIM in 12-pole direct-drive applications is not a straightforward recommendation, it remains competitive.
- In terms of design robustness, high-pole-count SynRM exhibit severe performance drawbacks and low robustness, whereas PMSM demonstrates sensitivity primarily in ripple torque, with worst-case scenarios potentially showing triple the torque ripple of the flawless design under typical manufacturing tolerances. In contrast, the proposed AF-MRIM, showcases outstanding design robustness, with airgap length being the main critical factor requiring tight tolerances.

The findings in this section complete the coverage of SO4, and fully covers SO3 (refer to Section 1.4.2).

6. Conclusions

The findings of this thesis aim to provide comprehensive guidelines for the initial sizing, design refinement, multi-objective optimization, tolerance analysis, robustness assessment, and competitiveness evaluation of AF-MRIMs using efficient analytical, semi-analytical and numerical tools.

This initial phase of AF-MRIM analysis involved analytical sizing equations and detailed 3D FE simulations. Validation was carried out through experimental testing of a 250 rpm, 24-pole, 20 HP prototype. FE simulations confirmed the main assumptions made in the sizing equations, particularly regarding rotor parameters such as iron wire diameter and rotor iron ratio. Optimizations focusing on these parameters showed promising results in enhancing efficiency and torque capacity. However, conducting a 3D FE evaluation for a single MRIM design can be time-intensive, taking up to 72 hours on a high-end 32-core workstation, which makes impractical its use for design exploration, multi-objective optimization, and tolerance/robustness assessment. Accordingly, it is suggested to reserve the proposed 3D model final design verification rather than sensitivity analysis or iterative refinement.

Previously, there were no works covering the design refinement of AF-MRIMs, which restricted the disclosure of its application niche. To address this gap, a novel methodology was devised to progressively simplify the complexity of the full 3D model, facilitating large-scale evaluations and identifying sources of estimation error. The tools proposed in this thesis enable AF-MRIMs to be integrated into large-scale optimization problems, refining initially sized machines through MOGA paired with a 2D linear PMS model. This approach resulted in substantial improvements in torque capacity, efficiency and power factor. The final optimized 24-pole AF-MRIM design studied in this thesis was achieved a 50% increased rated torque, 13 points higher efficiency, and an impressive 20-point power factor increase when compared to the initial design, maintaining the same overall volume and current restraints. Sensitivity analysis using the 3D PMS model identified critical parameters like airgap length, stator slot height, and tooth-tip dimensions, crucial for maintaining robust performance.

To demonstrate the superiority of AF-MRIM in LSHT applications, direct comparisons were made with established electrical machines using deterministic and robust design approaches. Recommendations for application can be summarized as follows.

For asynchronous machines, a UUM assessment is recommended due to its low computational burden. To disclose expected performance within typical manufacturing tolerance ranges, it is advised to create a representative set of machines with Gaussian distribution of dimensional deviations. If a more catastrophic approach wants to be considered, worst-case designs can be identified using reverse multi-objective optimization. These worst-case scenarios are not representative of the design performance after assembly, but rather sets the lowest performance boundary within the selected tolerance range. In this work, the scope of this assessment is limited to typical tolerances found in laser cutting or CNC steel punching, although extreme tolerances or customized tolerance ranges can also be evaluated by means of this proposal, depending on the manufacturing and assembly resource availability.

For synchronous machines, a UUM assessment is also suitable for most performance indices. Nonetheless, as presented in Section 4.4.4, and in agreement with recent research, torque ripple of PMSM requires a more detailed analysis to disclose its sensitiveness in the presence of unevenly distributed dimensional tolerances. Therefore, it is suggested to analyze the torque waveform of a representative set of machines applying a Gaussian distribution of dimensional deviations across each parameter and structural unit involved. For this evaluation, the superposition method described in Section 4.3 is recommended due to its minimal computational requirements and ease of scalability.

In conclusion, integrating design refinements of AF-MRIMs from Section 3 with robust assessment tools from Section 4 supported a detailed comparative analysis with RF-SCIM, RF-SynRM and RF-PMSM. Qualitative trends and findings from this comparative study on optimized 250 and 500 rpm machines can be found in Table 6.1.

Table 6.1 Comparison of expected rated performance of optimized LSHT machines.

		24-pole				**12-pole**			
Indicator	**Type**	**SynRM**	**SCIM**	**MRIM**	**PMSM**	**SynRM**	**SCIM**	**MRIM**	**PMSM**
Torque density	Value	××	✓	✓✓	✓✓✓	×	✓	✓✓	✓✓✓
	Robustness	✓	✓	✓✓✓	✓	✓	✓	✓✓	✓
Torque ripple	Value	×××	✓	✓	✓✓	××	×	✓✓	✓✓✓
	Robustness	✓	×	✓✓	×××	✓✓	✓	✓✓	×××
Efficiency	Value	✓✓✓	×	✓	✓✓	✓✓✓	✓✓	✓✓	✓✓✓
	Robustness	✓✓✓	✓	✓✓✓	✓✓✓	✓✓✓	✓	✓✓	✓✓✓
Power factor	Value	××	×	✓✓	✓✓✓	×	✓	✓✓✓	✓✓✓
	Robustness	×	×	✓✓	✓✓✓	✓	✓	✓✓	✓✓✓

At last, it was found that the proposed AF-MRIMs are suitable for LSHT applications, with significant advantages at direct-drive 250 rpm operation, and slight advantages at 500 rpm when compared to prominent rare-earth free topologies.

The fulfillment of each specific objective outlined in this thesis (refer to Section 1.4.2) is described below:

- **SO1:** A comprehensive initial-sizing methodology was developed, FE simulations were conducted, and the AF-MRIM model was progressively simplified to estimate efficiency, torque, and power factor of the machine. This approach allowed for large-scale evaluation of the topology considering exact dimensions.
- ***SO2:*** Several FE tools were created and adapted to evaluate the impact of unavoidable manufacturing and assembly tolerances on the performance of both asynchronous and synchronous machines, including AF-MRIMs. UUM and non-UUM tools were introduced, identifying key parameters of the AF-MRIM with the most sensitiveness to variations. These findings served as input for the comparative analysis in Section 5.
- **SO3:** Section 5 provided a detailed comparison of AF-MRIM against other conventional and non-conventional topologies, assessing raw performance and robust design capability to determine its suitability and competitiveness in LSHT applications. Optimization and comparison were performed for two objective speeds across various topologies.
- ***SO4:*** Based on Section 3 findings, guidelines were established for the optimal AF-MRIM design focusing on parameters like iron wire diameter, rotor iron proportion, rotor axial length and stator slot height (Section 3.2 and 3.3). Robust design aspects were addressed through sensitivity analyses, robustness assessments, and relevant tools (Section 3.5, 4.3 and 5), highlighting the AF-MRIM superior design robustness when adhering to matrix-rotor recommendations in Section 3.2.

From the detailed findings and conclusions above, future research include:

- Conducting prototyping and experimental testing of an optimized AF-MRIM design to validate the developed tools.
- Evaluating the performance of the proposed design in regular-speed applications to further establish its applicability in LSHT applications and clarify its limitations in regular industrial applications, Based on obtained results, it was deduced that further decreasing the machine pole count renders SCIM designs comparable to AF-MRIM designs. Further evaluation is required.
- Investigating the impact of steel punching on AF-MRIM performance, accounting for permeability losses around the cutting edges. This aspect may significantly affect performance, and showcase a reason to prefer laser cutting for the MRIM dimensioning.

- Dimensioning and implementing a thermal management system to enhance the maximum current density the machine can develop, in order to further increase performance ratings of the AF-MRIM.

Documentation and References

[1] J. M. Crider and S. D. Sudhoff, "An inner rotor flux-modulated permanent magnet synchronous machine for low-speed high-torque applications," IEEE Trans. Energy Convers., vol. 30, no. 3, pp. 1247-1254, **2015**.

[2] M. Onsal, B. Cumhur, Y. Demir, E. Yolacan and M. Aydin, "Rotor design optimization of a new flux-assisted consequent pole spoke-type permanent magnet torque motor for low-speed applications," IEEE Trans. Magn., vol. 54, no. 11, pp. 1-5, **2018**.

[3] Z. Zhang, S. Yu, F. Zhang, S. Jin and X. Wang, "Electromagnetic and structural design of a novel low-speed high-torque motor with dual-stator and PM-reluctance rotor," IEEE Trans. Appl. Superconduct., vol. 30, no. 4, pp. 1-5, **2020**.

[4] A. Marfoli, M. Di Nardo, M. Degano, C. Gerada and W. Chen, "Rotor design optimization of squirrel cage induction motor - part I: problem statement," *IEEE Transactions on Energy Conversion*, 36(2), pp. 1271-1279, **2021**.

[5] F. Ferreira; G. Baoming; A. Almeida, "Reliability and operation of high-efficiency induction motors," *IEEE Transactions on Industry Applications*, 52(6), pp. 4628-4637, **2016**.

[6] N. Reyes; M. A. Tapia; J. A. Tapia; W. Jara; A. E. Hoffer, "Multiphysical design of an axial induction motor with an anisotropic rotor," *2018 IEEE International Conference on Automation/XXIII Congress of the Chilean Association of Automatic Control* (ICA-ACCA), Concepcion, pp. 1-7, **2018**.

[7] S. Evon; R. Schiferl, "Direct-drive induction motors: using an induction motor as an alternative to a motor with reducer," *IEEE Industry Applications Magazine*, 11(4), pp. 45-51, **2005**.

[8] T. M. Jahns, "The expanding role of PM machines in direct-drive applications," *International Conference on Electrical Machines and Systems*, Beijing, pp. 1-6, **2011**.

[9] B. Zhang, B. Liang, G. Xu, W. Wang and G. Feng, "Research on variable frequency low-speed high-torque squirrel cage induction machine for elevator," 2011 International Conference on Electrical Machines and Systems, Beijing, China, **2011**, pp. 1-5.

[10] L. Bing-Xue, W. Da-Zhi, Z. Bing-Yi and X. Guang-Ren, "Research of Low-Power Low-Speed Squirrel-cage Motor," 2019 Chinese Control And Decision Conference (CCDC), Nanchang, China, **2019**, pp. 3718-3723.

[11] S. Khaliq, M. Modarres, T. A. Lipo and B. -I. Kwon, "Design of novel axial-flux dual stator doubly fed reluctance machine," IEEE Trans. Magn., vol. 51, no. 11, pp. 1-4, **2015**.

[12] M. Mirzaei, "Computational modeling of an axial airgap induction motor with a solid rotor," *IEEE Transactions on Magnetics*, 58(6), pp. 1-9, **2022**.

[13] Z. Cao, A. Mahmoudi, S. Kahourzade, W. L. Soong and J. R. Summers, "A comparative study of axial-flux versus radial-flux induction machines," 2020 IEEE International Conference on Power Electronics, Drives and Energy Systems (PEDES), pp. 1-6, **2020**.

[14] A. Cavagnino; M. Lazzari; F. Profumo; A. Tenconi, "A comparison between the axial flux and the radial flux structures for PM synchronous motors," *IEEE Transactions on Industry Applications*, 38(6), pp. 1517-1524, **2002**.

[15] M. A. Tapia; A. E. Hoffer; J. A. Tapia; R. R. Wallace, "Simulation and analysis of an axial flux induction machine," *IEEE Latin America Transactions*, 15(7), pp. 1263-1269, **2017**.

[16] B. Dianati, S. Kahourzade, A. Mahmoudi, "Optimization of axial-flux induction motors for the application of electric vehicles considering driving cycles", *IEEE Transactions on Energy Conversion*, 35(3), pp. 1522-1533, **2020**.

[17] Z. Nasiri-Gheidari; H. Lesani, "A survey on axial flux induction motors," *Prz. Elektrotechniczny* (Review Electr. Eng)., 88(2), pp. 300– 305, **2012**.

[18] D. K. Banchhor; A. Dhabale, "Design, modeling, and analysis of dual rotor axial flux induction motor," *2018 IEEE International Conference on Power Electronics, Drives and Energy Systems (PEDES)*, Chennai, India, pp. 1-6, **2018**.

[19] S. Das; Y. Sozer, "Design and analysis of an axial flux doubly fed induction generator for wind turbine applications," *2019 IEEE Energy Conversion Congress and Exposition (ECCE)*, Baltimore, MD, USA, pp. 442-447, **2019.**

[20] F. Keskin; I. Senol; Y. Oner; "Performance analysis of axial-flux induction motor with skewed rotor," *Energies*, 13(19), 4991, **2020**.

[21] M. Ito; K. Arai; N. Takahashi; H. Kiwaki; T. Seya, "Magnetically anisotropic solid rotor of an induction motor," *IEEE Transactions on Energy Conversion*, 3(2), pp. 427-432, **1988**.

[22] M. A. Tapia; W. Jara; R.R. Wallace; J. A. Tapia, "Parameters identification of an axial flux induction machine using field equations," *2018 XIII International Conference on Electrical Machines* (ICEM), Alexandroupoli, pp. 351-357, **2018**.

[23] A. Cavagnino, "Accuracy enhanced algorithms for the slot leakage inductance computation of double-layer windings," *IEEE Transactions on Industry Applications*, 53(5), pp. 4422-4430, **2017**.

[24] A. Boglietti; A. Cavagnino; M. Lazzari, "Computational algorithms for induction motor equivalent circuit parameter determination-Part I: Resistances and leakage reactances," *IEEE Transactions on Industrial Electronics*, 58(9), pp. 3723–3733, **2011**.

[25] M. Bortolozzi; L. Branz; A. Tessarolo; C. Bruzzese, "Improved analytical computation of rotor rectangular slot leakage inductance in squirrelcage induction motors," *2015 International Conference on Sustainable Mobility Applications, Renewables and Technology*, Kuwait, pp. 1–5, **2015**.

[26] R. R. Wallace; L. Moran; D. Contreras; J. Valenzuela and L. Laakso, "Construction and evaluation of an anisotropic rotor for axial flux induction motor," *PEMC'94*, Warsaw, Poland, pp. 1341-1346, **1994**.

[27] C. Madariaga, J. Tapia, N. Reyes, W. Jara and M. Degano, "Influence of constructive parameters on the performance of an axial-flux induction machine with solid and magnetically anisotropic rotor," *2021 IEEE Energy Conversion Congress and Exposition (ECCE)*, Vancouver, BC, Canada, pp. 4037-4044, **2021.**

[28] T. Q. Pham and S. N. Foster, "Additive manufacturing of non-homogeneous magnetic cores for electrical machines, opportunities and challenges," *International Conference on Electrical Machines (ICEM)*, pp. 1623-1629, Gothenburg, Sweden, **2020**.

[29] L. Gargalis, V. Madonna, P. Giangrande, R. Rocca, M. Hardy, I. Ashcroft, M. Galea, R. Hague, "Additive Manufacturing and Testing of a Soft Magnetic Rotor for a Switched Reluctance Motor," in IEEE Access, vol. 8, pp. 206982-206991, **2020**.

[30] F. Wu and A. M. EL-Refaie, "Toward additively manufactured electrical machines: opportunities and challenges," *IEEE Transactions on Industry Applications*, 56(2), pp. 1306-1320, **2020**.

[31] R. Wrobel and B. Mecrow, "A comprehensive review of additive manufacturing in construction of electrical machines," *IEEE Transactions on Energy Conversion*, 35(2), pp. 1054-1064, **2020**.

[32] G. Lei, G. Bramerdorfer, C. Liu, Y. Guo and J. Zhu, "Robust design optimization of electrical machines: a comparative study and space reduction strategy," *IEEE Transactions on Energy Conversion*, 36(1), pp. 300-313, **2021**.

[33] G. Bramerdorfer, J. A. Tapia, J. J. Pyrhönen and A. Cavagnino, "Modern electrical machine design optimization: techniques, trends, and best practices," *IEEE Transactions on Industrial Electronics*, 65(10), pp. 7672-7684, **2018**.

[34] J. Buschbeck, M. Vogelsberger, A. Orellano and E. Schmidt, "Pareto optimization in terms of electromagnetic and thermal characteristics of air-cooled asynchronous induction machines applied in railway traction drives," *IEEE Transactions on Magnetics*, 52(3), pp. 1-4, **2016**.

[35] C. Lin and C. Hwang, "Multiobjective optimization design for a six-phase copper rotor induction motor mounted with a scroll compressor," *IEEE Transactions on Magnetics*, 52(7), pp. 1-4, **2016**.

[36] N. Riviére, M. Villani and M. Popescu, "Optimisation of a high speed copper rotor induction motor for a traction application," *IECON 2019 - 45th Annual Conference of the IEEE Industrial Electronics Society*, pp. 2720-2725, **2019**.

[37] T. -V. Tran, E. Nègre, K. Mikati, P. Pellerey and B. Assaad, "Optimal design of TEFC induction machine and experimental prototype testing for city battery electric vehicle," *IEEE Transactions on Industry Applications*, 56(1), pp. 635-643, **2020**.

[38] E. Pérez, W. Jara, C. Madariaga, J. Tapia, G. Bramerdorfer, J. Riedemann, I. Petrov, J. Pyrhönen, "Comparison of optimized fault-tolerant modular stator machines with U-shape and H-shape core structure," *2021 IEEE Energy Conversion Congress and Exposition (ECCE)*, pp. 4254-4259, **2021**.

[39] W. Jara, G. Bramerdorfer, C. Madariaga, J. Riedemann, J. Tapia, G. Segon, W. Koppelstätter, S. Silber, "Analysis and optimization of radial flux modular stator permanent magnet synchronous machines," *2020 IEEE Energy Conversion Congress and Exposition (ECCE)*, pp. 1167-1173, **2020**.

[40] T. Gundogdu, Z. Q. Zhu and J. C. Mipo, "Optimization and improvement of advanced nonoverlapping induction machines for EVs/HEVs," *IEEE Access*, 10, pp. 13329-13353, **2022**.

[41] C. Madariaga, W. Jara, D. Riquelme, G. Bramerdorfer, J.A. Tapia, J. Riedemann, "Impact of tolerances on the cogging torque of tooth-coil-winding PMSMs with modular stator core by means of efficient superposition technique. *Electronics*, 9(10), 1594, **2020**.

[42] Lei, G.; Zhu, J.; Guo, Y.; Liu, C.; Ma, B. "A review of design optimization methods for electrical machines," *Energies*, 10, **2017**.

[43] N. Taran, V. Rallabandi, D. M. Ionel, P. Zhou, M. Thiele and G. Heins, "A systematic study on the effects of dimensional and materials tolerances on permanent magnet synchronous machines based on the IEEE std 1812," *IEEE Transactions on Industry Applications*, 55(2), pp. 1360-1371, **2019**.

[44] G. Bramerdorfer, "Tolerance analysis for electric machine design optimization: classification, modeling and evaluation, and example," *IEEE Transactions on Magnetics*, 55(8), pp. 1-9, **2019**.

[45] H. Guo, Z. Wu, H. Qian, K. Yu, J. Xu, "Statistical analysis on the additional torque ripple caused by magnet tolerances in surface-mounted permanent magnet synchronous motors," *IET Electric Power Applications*, 9(3), pp. 183-192. **2015**.

[46] G. Bramerdorfer, "Effect of the manufacturing impact on the optimal electric machine design and performance," *IEEE Transactions on Energy Conversion*, 35(4), pp. 1935-1943, **2020**.

[47] G. Lei, G. Bramerdorfer, B. Ma, Y. Guo and J. Zhu, "Robust design optimization of electrical machines: multi-objective approach," *IEEE Transactions on Energy Conversion*, 36(1), pp. 390-401, **2021**.

[48] G. Lei, C. Liu, Y. Li, D. Chen, Y. Guo and J. Zhu, "Robust design optimization of a high-temperature superconducting linear synchronous motor based on taguchi method," *IEEE Transactions on Applied Superconductivity*, 29(2), pp. 1-6, **2019**.

[49] M. Klausnitzer, A. Möckel, "Quick cogging torque calculation for electronically commutated motors considering combinations of deviant and flawless magnets," *International Symposium on Power Electronics Power Electronics, Electrical Drives, Automation and Motion*, pp. 66-69, **2012**.

[50] A. Escobar, G. Sánchez, W. Jara, C. Madariaga, J. Tapia, M. Degano, J. Riedemann, "Statistical analysis of manufacturing tolerances effect on axial-flux permanent magnet machines cogging torque," *2021 IEEE Energy Conversion Congress and Exposition (ECCE)*, pp. 4342-4346, **2021**.

[51] M. Valtonen; A. Parviainen; J. Pyrhonen, "The effects of the number of rotor slots on the performance characteristics of axial-flux aluminium-cage solid-rotor core induction motor," *2007 IEEE International Electric Machines & Drives Conference*, Antalya, pp. 668-672, **2007**.

[52] M. Valtonen; A. Parviainen; J. Pyrhönen, "Influence of the air-gap length to the performance of an axial-flux induction motor," *2008 18th International Conference on Electrical Machines*, Vilamoura, Portugal, pp. 1–5, **2008**.

[53] J. Igelspacher; S. Fluegel; H. G. Herzog, "Analytic examination of coupled axial-flux induction machines with reduced yoke," *2011 1st International Electric Drives Production Conference*, Nuremeberg, pp. 153–158, **2011**.

[54] Z. Nasiri-Gheidari and H. Lesani, "Optimal design of adjustable air-gap, two-speed, capacitor-run, single-phase axial flux induction motors," *IEEE Transactions on Energy Conversion*, 28(3), pp. 543-552, **2013.**

[55] B. P. B. Arthur; U. Baskaran; "Improved air-gap flux in axial flux induction machine through shaping of radial slot opening," *Sādhanā* 45(134), **2020**.

[56] K. Bitsi, M. E. Beniakar, O. Wallmark and S. G. Bosga, "Preliminary electromagnetic sizing of axial-flux induction machines," *2020 International Conference on Electrical Machines (ICEM)*, pp. 284-290, **2020**.

[57] C. Hong, W. Huang and Z. Hu, "Performance calculation of a dual stator solid rotor axial flux induction motor using the multi-slice and multi-layer method," *IEEE Transactions on Magnetics*, 55(2), pp. 1-9, **2019**.

[58] D. Spalek, "Synchronous torque of induction motor with solid and magnetically anisotropic rotor," *Maszyny Elektryczne*, vol. 84, **2009**.

[59] J. Pryhönen, T. Jokinen and V. Hrabovcová, "Design of rotating electrical machines," Chichester, West Sussex: John Wiley & Sons, **2014.**

[60] J. A. Tapia, J. Pyrhonen, J. Puranen, P. Lindh and S. Nyman, "Optimal Design of Large Permanent Magnet Synchronous Generators," IEEE Trans. Magn., vol. 49, no. 1, pp. 642-650, Jan. **2013.**

[61] D. M. Ionel, M. Popescu, M. I. McGilp, T. J. E. Miller, S. J. Dellinger, R. J. Heideman, "Computation of core losses in electrical machines using improved models for laminated steel," IEEE Transactions on Industry Applications, pp. 1554 - 1564, Vol. 43, No. 6, Nov. - Dec. **2007**.

[62] C. Madariaga, W. Jara, J. A. Tapia, J. Pyrhönen, P. Lindh and J. A. Riedemann, "Closed-Form Solution for the Slot Leakage Inductance of Tooth-Coil-Winding Permanent Magnet Machines," in IEEE Transactions on Energy Conversion, vol. 34, no. 3, pp. 1572-1580, Sept. **2019.**

[63] G. Heins, T. Brown and M. Thiele, "Statistical analysis of the effect of magnet placement on cogging torque in fractional pitch permanent magnet motors," in IEEE Transactions on Magnetics, vol. 47, no. 8, pp. 2142-2148, Aug. **2011**.

[64] Y. Yang, N. Bianchi, C. Zhang, X. Zhu, H. Liu and S. Zhang, "A Method for Evaluating the Worst-Case Cogging Torque Under Manufacturing Uncertainties," in IEEE Transactions on Energy Conversion, vol. 35, no. 4, pp. 1837-1848, Dec. **2020**.

[65] G. Bramerdorfer and A. -C. Zăvoianu, "Surrogate-Based Multi-Objective Optimization of Electrical Machine Designs Facilitating Tolerance Analysis," in IEEE Transactions on Magnetics, vol. 53, no. 8, pp. 1-11, Aug. **2017**.

[66] G. Bramerdorfer, "Computationally Efficient Tolerance Analysis of the Cogging Torque of Brushless PMSMs," in IEEE Transactions on Industry Applications, vol. 53, no. 4, pp. 3387-3393, July-Aug. **2017**.

[67] M. A. Khan, I. Husain, and M. R. Islam, "Design of experiments to address manufacturing tolerances and process variations influencing cogging torque and back EMF in the mass production of the permanent-magnet synchronous motors," IEEE Trans. Ind. Appl., vol. 50, no. 1, pp. 346–355, Jan./Feb. **2013**.

[68] L. Gasparin, A. Cernigoj, S. Markic and R. Fiser, "Additional Cogging Torque Components in Permanent-Magnet Motors Due to Manufacturing Imperfections," in IEEE Transactions on Magnetics, vol. 45, no. 3, pp. 1210-1213, March **2009**.

[69] H. Chen and C. H. T. Lee, "Parametric Sensitivity Analysis and Design Optimization of an Interior Permanent Magnet Synchronous Motor," in IEEE Access, vol. 7, pp. 159918-159929, Nov. **2019**.

[70] M. Thiele and G. Heins, "Computationally Efficient Method for Identifying Manufacturing Induced Rotor and Stator Misalignment in Permanent Magnet Brushless Machines," in IEEE Transactions on Industry Applications, vol. 52, no. 4, pp. 3033-3040, July-Aug. **2016**.

[71] Z. Q. Zhu, S. Ruangsinchaiwanich and D. Howe, "Synthesis of cogging-torque waveform from analysis of a single stator slot," in IEEE Transactions on Industry Applications, vol. 42, no. 3, pp. 650-657, May-June **2006**.

[72] Z. Q. Zhu, S. Ruangsinchaiwanich, Y. Chen, and D. Howe, "Evaluation of superposition technique for calculating cogging torque in permanent-magnet brushless machines,"IEEE Transactions on Magnetics, vol. 42, pp. 1597-1603, May. **2006**.

[73] A. Escobar; G. Sánchez; W. Jara; C. Madariaga; J. A. Tapia; J. Riedemann; E. Reyes, "Impact of manufacturing tolerances on axial flux permanent magnet machines with ironless rotor core: a statistical approach," Machines, vol. 11, p. 535, May. **2023**.

[74] C. Madariaga, C. Gallardo, J. A. Tapia, W. Jara, A. Escobar and M. Degano, "Fast Assessment of Rotor Barrier Dimensional Allowances in Synchronous Reluctance Machines," in IEEE Access, vol. 11, pp. 58349-58358, Jun. **2023**.

[75] O. Korman, M. Degano, M. Di Nardo, and C. Gerada, "A Novel Flux Barrier Parametrization for Synchronous Reluctance Machines," IEEE Transactions on Energy Conversion, vol. 8969, no. c, pp. 1–11, **2021**.

[76] H. Kim et al., “Study on Analysis and Design of Line-Start Synchronous Reluctance Motor Considering Rotor Slot Opening and Bridges,” IEEE Transactions on Magnetics, vol. 58, no. 2, Feb. **2022**.

[77] C. Gallardo, J. A. Tapia, M. Degano, H. Mahmoud and A. E. Hoffer, "Rotor asymmetry impact on synchronous reluctance machines performance," 2022 International Conference on Electrical Machines (ICEM), **2022**, pp. 848-854.

[78] ST. Boroujeni, M. Haghparast, N. Bianchi, “Optimization of flux barriers of line-start synchronous reluctance motors for transient-and steady-state operation,” Electric Power Components and Systems, vol. 43, no. 5, pp. 594-606, **2015**.

[79] A. Credo, G. Fabri, M. Villani, M. Popescu, “A robust design methodology for synchronous reluctance motors,” IEEE Trans. Energy Convers., vol. 35, no. 4, pp. 2095-2105, Dec. **2020**.

[80] Ibrahim, M.N.F.; Sergeant, P.; Rashad, E. Simple Design Approach for Low Torque Ripple and High Output Torque Synchronous Reluctance Motors. Energies **2016**, 9, 942.

[81] C. Liu, K. Wang, S. Wang, Y. Wang and J. Zhu, "Torque ripple reduction of synchronous reluctance machine by using asymmetrical barriers and hybrid magnetic core," in CES Transactions on Electrical Machines and Systems, vol. 5, no. 1, pp. 13-20, March **2021**.

[82] Y. Hidaka and H. Igarashi, “Topology optimization of synchronous reluctance motors considering localized magnetic degradation caused by punching,” IEEE Trans. Magn., vol. 53, no. 6, pp. 1–4, Jun. **2017**.

[83] H. Mahmoud, N. Bianchi, G. Bacco, and N. Chiodetto, “Nonlinear Analytical Computation of the Magnetic Field in Reluctance Synchronous Machines,” IEEE Transactions on Industry Applications, vol. 53, no. 6, pp. 5373–5382, Nov. **2017**.

[84] C. Gallardo, J. A. Tapia, M. Degano and H. Mahmoud, "Accurate Analytical Model for Synchronous Reluctance Machine With Multiple Flux Barriers Considering the Slotting Effect," in IEEE Transactions on Magnetics, vol. 58, no. 9, pp. 1-9, Sept. **2022**.

[85] G. Artetxe, D. Caballero, B. Prieto, M. Martinez-Iturralde, and I. Elosegui, Eliminating rare earth permanent magnets on low-speed high-torque machines: A performance and cost comparison of synchronous reluctance machines, ferrite permanent magnet-synchronous reluctance machines and permanent magnet synchronous machines for a direct-drive elevator system,” IET Electr. Power Appl., vol. 15, no. 3, pp. 370–3378, Feb. **2021**.

[86] S. Kou, Z. Kou, J. Wu, and Y. Wang, “Modeling and simulation of a novel low-speed high-torque permanent magnet synchronous motor with asymmetric stator slots,” Machines, vol. 10, no. 12, p. 1143, Dec. **2022**.

[87] P. Premaratne, I. Jawad-Kadhim, M. Qadim-Abdullah, B. Halloran, P. James-Vial, “A survey on low speed low power axial flux generator design and optimization using simulation,” Neurocomputing, vol. 509, pp. 272-289, Oct. **2022**.

[88] I. Petrov, M. Niemel¨a, P. Ponomarev, and J. Pyrhönen, “Rotor surface ferrite permanent magnets in electrical machines: Advantages and limitations,” IEEE Trans. Ind. Electron., vol.64, no.7, pp.53145322, Jul. **2017**.

[89] S. G. Min, "Investigation of Key Parameters on Cogging Torque in Permanent Magnet Machines Based on Dominant Harmonic Contents," in IEEE Transactions on Transportation Electrification, vol. 10, no. 1, pp. 174-186, March **2024**.

[90] Y. Zhao, S. Zhang, C. Zhang, G. Yang and Y. Yang, "Analysis of Cogging Torque of Permanent Magnet Motors Under Mixed-Eccentricity and Manufacturing Tolerances," in IEEE Access, vol. 12, pp. 6672-6683, Jan. **2024**.

[91] Hyung Kim and B. Sarlioglu, "Influences of Manufacturing Tolerance on Performance of Axial Flux-Switching Permanent Magnet Machine," in IEEE ECCE, pp. 7322-7329, **2018**.

[92] L. Yang, J. Zhao, X. D. Liu, A. Haddad, J. Liang, and H. Hu, ‘‘Effects of manufacturing imperfections on the circulating current in ironless brushless DC motors,’’ IEEE Trans. Ind. Electron., vol. 66, no. 1, pp. 338–348, Jan. **2019**.

[93] I. Coenen, M. V. D. Giet, and K. Hameyer, “Manufacturing tolerances: Estimation and prediction of cogging torque influenced by magnetization faults,” IEEE Trans. Magn., vol. 48, no. 5, pp. 1932–1936, May. **2012**.

[94] A. Abedini Mohammadi, S. Zhang, J. Gyselinck, A. -C. Pop and W. Zhang, "Manufacturing-Induced Cogging Torque in Segmented Stator Permanent-Magnet Machines With Respect to Steel Punching," in IEEE Transactions on Magnetics, vol. 58, no. 9, pp. 1-8, Sept. **2022**.

[95] D. Riquelme, C. Madariaga, W. Jara, G. Bramerdorfer, J. A. Tapia, and J. Riedemann, “Study on stator-rotor misalignment in modular permanent magnet synchronous machines with different slot/pole combinations,” Applied Sciences, vol. 13, no. 5, p. 2777, Feb. **2023**.

[96] G. Joksimović, J.I. Melecio, P.M Tuohy and S. Djurović, “Towards the optimal ‘slot combination’ for steady-state torque ripple minimization: an eight-pole cage rotor induction motor case study,” in Electrical Engineering, vol. 102, pp. 293–308, Nov. **2019**.

[97] S. Taghavi and P. Pillay, “A novel grain-oriented lamination rotor core assembly for a synchronous reluctance traction motor with a reduced torque ripple algorithm,” IEEE Transactions on Industry Applications, vol. 52, no. 5, pp. 3729–3738, **2016**.

[98] K. B. Tawfiq, M. N. Ibrahim, E. E. El-Kholy, and P. Sergeant, “Performance improvement of synchronous reluctance machines - a review research,” IEEE Trans. Magn., vol. 57, no. 10. **2021**.

[99] Y. Wang, D. M. Ionel, V. Rallabandi, M. Jiang and S. J. Stretz, "Large-Scale Optimization of Synchronous Reluctance Machines Using CE-FEA and Differential Evolution," in IEEE Transactions on Industry Applications, vol. 52, no. 6, pp. 4699-4709, Nov.-Dec. **2016**.

[100] A. Credo, M. Villani, M. Popescu and N. Riviere, "Application of Epoxy Resin in Synchronous Reluctance Motors With Fluid-Shaped Barriers for E-Mobility," in IEEE Transactions on Industry Applications, vol. 57, no. 6, pp. 6440-6452, Nov.-Dec. **2021**.

[101] Z. Q. Zhu, L. J. Wu and M. L. M. Jamil, "Influence of pole and slot number combinations on cogging torque in permanent magnet machines with static and rotating eccentricities," 2013 IEEE Energy Conversion Congress and Exposition, Denver, CO, USA, **2013**, pp. 2834-2841.

[102] Y. Yang; W. Cai; X. Jin; S. Zhang; C. Zhang; R. Li; Y. Zhao, "An approach for estimating the cogging torque performance considering manufacturing uncertainties for the IPM machine," in IEEE Access, vol. 11, pp. 107019-107030, Sep. **2023**.

[103] Y. Zhao, S. Zhang, C. Zhang, G. Yang and Y. Yang, "Analysis of cogging torque of permanent magnet motors under mixed-eccentricity and manufacturing tolerances," in IEEE Access, vol. 12, pp. 6672-6683, Jan. **2024**.

A. Photographic record of the 20 HP MRIM prototype

A 20 HP AF-MRIM prototype with two stators and one rotor was tested for validation in this thesis. Photographs documenting the prototype are presented in the following figures.

(a)

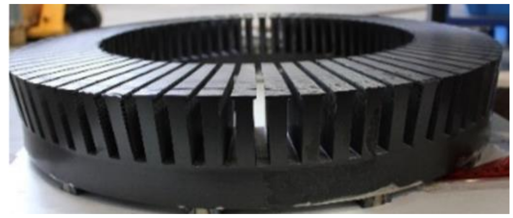

(b)

(c)

Fig. A.1 20-HP AF-MRIM prototype
(a) Outer view of the machine case, (b) stator structure, (c) Rotor, shaft and bearing closeup.

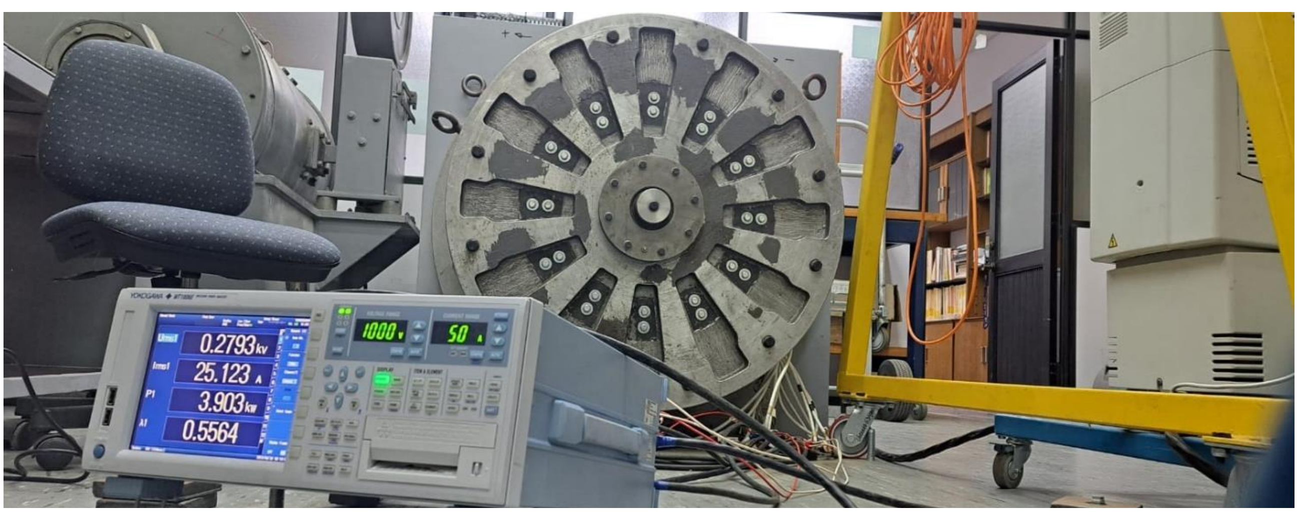

Fig. A.2 Maximum power factor ever achieved by the 20-HP AR-AFIM prototype at 4% slip, 50 Hz, 288 V.

B. Validation scenarios of the tolerance analysis tool

B.1. SynRM

Table B.1 summarizes the data of the validation scenarios considered for the SynRM in Section 4.4.3, including the dimensional deviation magnitude and the barriers and poles affected by dimensional deviations. These scenarios were selected in order to consider i) severe dimensional deviations acting on a single barrier that is different to that evaluated in the first steps of the methodology; ii) dimensional deviations acting on both sides of barriers; iii) dimensional deviations acting on different sides of several barriers simultaneously.

Table B.1 All cases considered to assess the proposed method on SynRMs (using exaggerated tolerance values)

		b_{11l}	b_{11r}	b_{21l}	b_{21r}	b_{31l}	b_{31r}	b_{41l}	b_{41r}	b_{51l}	b_{51r}	b_{61l}	b_{61r}
4P1B	SC1	0	0	0	0	0	+4	0	0	-	-	-	-
	SC2	0	0	-4	+4	0	0	0	0	-	-	-	-
	SC3	0	0	0	+4	+4	-4	+4	-4	-	-	-	-
6P1B	SC1	0	0	0	0	-4	0	0	0	0	0	0	0
	SC2	0	0	0	0	0	0	0	0	+4	-4	0	0
	SC3	0	0	-4	+4	-4	0	0	0	0	0	0	+4
4P2B	SC1	b_{11l}	b_{11r}	b_{21l}	b_{21r}	b_{31l}	b_{31r}	b_{41l}	b_{41r}	b_{51l}	b_{51r}	b_{61l}	b_{61r}
		0	0	0	0	-4	0	0	0	-	-	-	-
		b_{12l}	b_{12r}	b_{22l}	b_{22r}	b_{32l}	b_{32r}	b_{42l}	b_{42r}	b_{52l}	b_{52r}	b_{62l}	b_{62r}
		0	0	0	0	0	0	0	0	-	-	-	-
	SC2	b_{11l}	b_{11r}	b_{21l}	b_{21r}	b_{31l}	b_{31r}	b_{41l}	b_{41r}	b_{51l}	b_{51r}	b_{61l}	b_{61r}
		0	0	0	0	0	0	+4	0	-	-	-	-
		b_{12l}	b_{12r}	b_{22l}	b_{22r}	b_{32l}	b_{32r}	b_{42l}	b_{42r}	b_{52l}	b_{52r}	b_{62l}	b_{62r}
		0	0	0	0	0	0	0	+4	-	-	-	-
	SC3	b_{11l}	b_{11r}	b_{21l}	b_{21r}	b_{31l}	b_{31r}	b_{41l}	b_{41r}	b_{51l}	b_{51r}	b_{61l}	b_{61r}
		0	0	-4	0	0	0	0	0	-	-	-	-
		b_{12l}	b_{12r}	b_{22l}	b_{22r}	b_{32l}	b_{32r}	b_{42l}	b_{42r}	b_{52l}	b_{52r}	b_{62l}	b_{62r}
		0	0	-4	-4	0	0	0	0	-	-	-	-
	SC4	b_{11l}	b_{11r}	b_{21l}	b_{21r}	b_{31l}	b_{31r}	b_{41l}	b_{41r}	b_{51l}	b_{51r}	b_{61l}	b_{61r}
		0	0	0	0	0	-4	0	-4	-	-	-	-
		b_{12l}	b_{12r}	b_{22l}	b_{22r}	b_{32l}	b_{32r}	b_{42l}	b_{42r}	b_{52l}	b_{52r}	b_{62l}	b_{62r}
		0	0	0	-4	+4	+4	0	0	-	-	-	-
6P2B	SC1	b_{11l}	b_{11r}	b_{21l}	b_{21r}	b_{31l}	b_{31r}	b_{41l}	b_{41r}	b_{51l}	b_{51r}	b_{61l}	b_{61r}
		0	0	0	0	0	-3	0	0	0	0	0	0
		b_{12l}	b_{12r}	b_{22l}	b_{22r}	b_{32l}	b_{32r}	b_{42l}	b_{42r}	b_{52l}	b_{52r}	b_{62l}	b_{62r}
		0	0	0	0	0	0	0	0	0	0	0	0
	SC2	b_{11l}	b_{11r}	b_{21l}	b_{21r}	b_{31l}	b_{31r}	b_{41l}	b_{41r}	b_{51l}	b_{51r}	b_{61l}	b_{61r}
		0	0	0	0	0	0	0	+3	0	0	0	0
		b_{12l}	b_{12r}	b_{22l}	b_{22r}	b_{32l}	b_{32r}	b_{42l}	b_{42r}	b_{52l}	b_{52r}	b_{62l}	b_{62r}
		0	0	0	0	0	0	-3	0	0	0	0	0
	SC3	b_{11l}	b_{11r}	b_{21l}	b_{21r}	b_{31l}	b_{31r}	b_{41l}	b_{41r}	b_{51l}	b_{51r}	b_{61l}	b_{61r}
		0	0	0	0	0	0	0	0	0	+3	0	0
		b_{12l}	b_{12r}	b_{22l}	b_{22r}	b_{32l}	b_{32r}	b_{42l}	b_{42r}	b_{52l}	b_{52r}	b_{62l}	b_{62r}
		0	0	0	0	0	0	0	0	-3	+3	0	0
	SC4	b_{11l}	b_{11r}	b_{21l}	b_{21r}	b_{31l}	b_{31r}	b_{41l}	b_{41r}	b_{51l}	b_{51r}	b_{61l}	b_{61r}
		0	0	+3	-3	0	0	0	0	0	0	+3	0
		b_{12l}	b_{12r}	b_{22l}	b_{22r}	b_{32l}	b_{32r}	b_{42l}	b_{42r}	b_{52l}	b_{52r}	b_{62l}	b_{62r}
		0	0	-3	0	0	0	0	0	0	0	+3	0

B.2. PMSM

Table B.2 summarizes the data of the validation scenarios considered for the PMSM in Section 4.4.4, including dimensional deviation magnitude and magnets affected by dimensional deviations. These scenarios were selected in order to consider i) severe angular deviations acting on a single magnet that is different to that evaluated in the first steps of the methodology; ii) severe dimensional deviations acting on several different magnets.

Table B.2 All cases considered to assess the proposed method (using exaggerated tolerance values)

		# of magnet and applied tolerance																							
# of scenario	Tolerance	1	2	3	4	5	6	7	8	9	10	11	12	13	14	15	16	17	18	19	20	21	22	23	24
	$\lvert\Delta\theta_{\mathrm{PM}}\rvert$=0.2°	0	0	0	0	0	0	0	0	0	0	0	0	0	0	0	0	0	0	0	0	0	0	0	0
1	$\lvert\Delta r_{\mathrm{PM}}\rvert$=0.2 mm	0	0	0	+	0	0	0	0	0	0	0	+	0	0	0	0	+	0	0	0	0	0	0	0
	$\lvert\Delta B_{\mathrm{r}}\rvert$=5%	0	0	0	0	0	0	0	0	0	0	0	0	0	0	0	0	0	0	0	0	0	0	0	0
	$\lvert\Delta\theta_{\mathrm{PM}}\rvert$=0.2°	0	0	0	0	0	0	0	0	0	0	0	0	0	0	0	0	0	0	0	0	0	0	0	0
2	$\lvert\Delta r_{\mathrm{PM}}\rvert$=0.2 mm	0	0	0	0	0	0	0	0	0	0	0	0	0	0	0	0	0	0	0	0	0	0	0	0
	$\lvert\Delta B_{\mathrm{r}}\rvert$=5%	0	0	0	+	0	0	0	0	0	0	0	+	0	0	0	0	+	0	0	0	0	0	0	0
	$\lvert\Delta\theta_{\mathrm{PM}}\rvert$=0.2°	0	0	0	0	0	+	0	0	+	0	0	0	0	0	0	0	0	0	0	+	0	0	0	0
3	$\lvert\Delta r_{\mathrm{PM}}\rvert$=0.2 mm	0	0	0	0	0	0	0	0	0	0	0	0	0	0	0	0	0	0	0	0	0	0	0	0
	$\lvert\Delta B_{\mathrm{r}}\rvert$=5%	0	0	0	0	0	0	0	0	0	0	0	0	0	0	0	0	0	0	0	0	0	0	0	0
	$\lvert\Delta\theta_{\mathrm{PM}}\rvert$=0.2°	0	0	-	+	-	0	0	0	0	0	0	0	0	0	0	0	0	0	0	0	0	0	0	0
4	$\lvert\Delta r_{\mathrm{PM}}\rvert$=0.2 mm	0	0	-	+	-	0	0	0	0	0	0	0	0	0	0	0	0	0	0	0	0	0	0	0
	$\lvert\Delta B_{\mathrm{r}}\rvert$=5%	0	0	-	+	-	0	0	0	0	0	0	0	0	0	0	0	0	0	0	0	0	0	0	0
	$\lvert\Delta\theta_{\mathrm{PM}}\rvert$=0.2°	0	0	+	-	+	0	0	0	0	0	0	0	0	0	0	0	0	0	0	0	0	0	0	0
5	$\lvert\Delta r_{\mathrm{PM}}\rvert$=0.2 mm	0	0	-	+	-	0	0	0	0	0	0	0	0	0	0	0	0	0	0	0	0	0	0	0
	$\lvert\Delta B_{\mathrm{r}}\rvert$=5%	0	0	+	-	+	0	0	0	0	0	0	0	0	0	0	0	0	0	0	0	0	0	0	0
	$\lvert\Delta\theta_{\mathrm{PM}}\rvert$=0.2°	0	0	+	-	0	0	+	0	0	0	0	+	0	0	0	+	-	0	0	0	-	0	0	0
6	$\lvert\Delta r_{\mathrm{PM}}\rvert$=0.2 mm	0	0	0	0	0	0	0	0	-	0	-	0	0	0	+	0	0	0	+	0	0	+	0	0
	$\lvert\Delta B_{\mathrm{r}}\rvert$=5%	0	0	+	0	0	0	+	0	0	+	0	-	0	0	-	-	-	0	0	0	0	0	+	0

C. Main data of optimized machines

C.1. Data of optimized 24-pole machines

In Table C.1, the main data of the optimized 24-pole AF-MRIM assessed in Section 5.3.1 is presented, summarizing main dimensional parameters.

Table C.1 Main data of the optimized 24-pole AF-MRIM

Symbol	Variable	Value	Unit
D_{o}	Outer diameter	696.0	mm
D_{i}	Inner diameter	464.0	mm
δ	Airgap length	2 x 1.5	mm
D_{fe}	Iron wire diameter	3	mm
Q_{s}	Number of slots per stator	72	-
p	Number of pole pairs	12	-
l_{r}	Rotor axial length	58.0	mm
h_{ys}	Height of stator yoke	19.7	mm
k_{matrix}	Rotor iron proportion	0.52	-
b_{s}	Slot width	11.5	mm
h_{s}	Slot height	46.9	mm
b_{o}	Slot opening (% of b_{s})	60	%
h_{tt1}	Tooth-tip major height	1.2	mm
h_{tt2}	Tooth-tip minor height	0.6	mm
V_{overall}	Overall volume	0.076	m^3
n_{cond}	Number of conductors per slot layer	10	-

In Table C.2, the main data of the optimized 24-pole RF-SCIM assessed in Section 5.3.2 is presented, considering main dimensional parameters.

Table C.2 Main data of the optimized 24-pole RF-SCIM

Symbol	Variable	Value	Unit
D_{so}	Stator outer diameter	479.8	mm
D_{si}	Stator inner diameter	397.7	mm
D_{ro}	Rotor outer diameter	395.3	mm
D_{ri}	Rotor inner diameter	212.3	mm
N_{m}	Rotor synchronous speed	250	RPM
δ	Airgap length	1.2	mm

J_s	Stator rated current density	3	A/mm2
Q_r	Number of rotor slots	96	-
Q_s	Number of stator slots	72	-
p	Number of pole pairs	12	-
l_{stk}	Stack length	421.1	mm
h_{ys}	Height of stator yoke	13.6	mm
h_{yr}	Height of rotor yoke	51.0	mm
b_{tr}	Rotor tooth width	5.6	mm
h_{tr}	Rotor tooth height	40.5	mm
b_{ts}	Stator tooth width	9.2	mm
h_{ss}	Stator slot height	26.5	mm
b_{os}	Stator slot opening (% of b_s)	24	%
h_{tt1s}	Stator tooth-tip minor height	0.9	mm
h_{tt2s}	Stator tooth-tip major height	2.6	mm
$V_{overall}$	Overall volume	0.0759	m^3
-	Number of parallel paths	2	-
n_{cond}	Number of conductors per slot layer	12	-

In Table C.3, the main data of the optimized 24-pole RF-SynRM assessed in Section 5.3.3 is presented, encompassing main dimensional parameters.

Table C.3 Main data of the optimized 24-pole SynRM

Symbol	Variable	Value	Unit
D_{so}	Stator outer diameter	507.4	mm
D_{si}	Stator inner diameter	372.8	mm
D_{ro}	Rotor outer diameter	370.4	mm
D_{ri}	Rotor inner diameter	167.3	mm
h_{ts}	Stator tooth height	41.5	mm
b_{ts}	Stator tooth width	7.2	mm
g	Air-gap length	1.2	mm
l_{st}	Stack length	378.0	mm
-	Volume	76.4	mm^3
Q_s	Number of stator slots	72	-
N	Number of turns per phase	864	-
p	Number of pole pairs	12	-
b	Number of barriers per pole	4	-
n	Synchronous speed	250	rpm

f	Frequency	50	Hz
V_n	Rated phase voltage	380	Vrms
J_n	Rated current density	3	$Arms/mm^2$
k_s	Stacking factor	0.95	-
e	Lamination thickness	0.35	mm
k_{air}	Insulation ratio	0.43	-

In Table C.4, the main data of the optimized 24-pole RF-PMSM assessed in Section 5.3.4 is presented, encompassing main dimensional parameters.

Table C.4 Main data of the optimized 24-pole RF-PMSM

Symbol	Variable	Value	Unit
D_{so}	Stator outer diameter	584.8	mm
D_{si}	Stator inner diameter	400.4	mm
D_{ro}	Rotor outer diameter	347.9	mm
D_{ri}	Rotor inner diameter	150.6	mm
h_{ts}	Stator tooth height	62.1	mm
b_{ts}	Stator tooth width	18.2	mm
g	Air-gap length	3.0	mm
l_{st}	Stack length	280.0	mm
-	Volume	0.0752	m^3
Q_s	Number of stator slots	27	-
N	Number of turns per phase	117	-
p	Number of pole pairs	12	-
h_{pm}	Magnet height	23.3	mm
n	Synchronous speed	250	rpm
f	Frequency	50	Hz
V_n	Rated line-to-line voltage	380	Vrms
J_n	Rated current density	3	$Arms/mm^2$
k_s	Stacking factor	0.95	-
e	Lamination thickness	0.35	mm
α_{pm}	Arc-to-pole-ratio	0.85	-
B_r	Magnet remanence	1.125	T
$N_{PM,seg}$	Number of magnet radial segments	5	-

C.2. Data of optimized 12-pole machines

In Table C.5, the main data of the optimized 12-pole AF-MRIM assessed in Section 5.4.1 is presented, summarizing main dimensional parameters.

Table C.5 Main data of the optimized 12-pole AF-MRIM

Symbol	Variable	Value	Unit
D_{o}	Outer diameter	702.0	mm
D_{i}	Inner diameter	468.0	mm
δ	Airgap length	2 x 1.5	mm
D_{fe}	Iron wire diameter	3	mm
Q_{s}	Number of slots per stator	72	-
p	Number of pole pairs	12	-
l_{r}	Rotor axial length	49.0	mm
h_{ys}	Height of stator yoke	26.3	mm
k_{matrix}	Rotor iron proportion	0.54	-
b_{s}	Slot width	13.3	mm
h_{s}	Slot height	45.7	mm
b_{o}	Slot opening (% of b_{s})	87	%
h_{tt1}	Tooth-tip major height	1.3	mm
h_{tt2}	Tooth-tip minor height	0.3	mm
V_{overall}	Overall volume	0.0768	m^3
n_{cond}	Number of conductors per slot layer	5	-

In Table C.6, the main data of the optimized 12-pole RF-SCIM assessed in Section 5.4.1 is presented, considering main dimensional parameters.

Table C.6 Main data of the optimized 12-pole RF-SCIM

Symbol	Variable	Value	Unit
D_{so}	Stator outer diameter	535.7	mm
D_{si}	Stator inner diameter	405.1	mm
D_{ro}	Rotor outer diameter	402.7	mm
D_{ri}	Rotor inner diameter	207.7	mm
N_{m}	Rotor synchronous speed	500	RPM
δ	Airgap length	1.2	mm
J_{s}	Stator rated current density	3	A/mm2
Q_{r}	Number of rotor slots	48	-
Q_{s}	Number of stator slots	72	-

p	Number of pole pairs	12	-
l_{stk}	Stack length	336.5	mm
h_{ys}	Height of stator yoke	21.0	mm
h_{yr}	Height of rotor yoke	60.8	mm
b_{tr}	Rotor tooth width	17.3	mm
h_{tr}	Rotor tooth height	34.8	mm
b_{ts}	Stator tooth width	9.5	mm
h_{ss}	Stator slot height	41.6	mm
b_{os}	Stator slot opening (% of b_s)	33	%
h_{tt1s}	Stator tooth-tip minor height	1.0	mm
h_{tt2s}	Stator tooth-tip major height	1.5	mm
$V_{overall}$	Overall volume	0.0758	m^3
-	Number of parallel paths	4	-
n_{cond}	Number of conductors per slot layer	15	-

In Table C.7, the main data of the optimized 12-pole RF-SynRM assessed in Section 5.4.1 is presented, encompassing main dimensional parameters.

Table C.7 Main data of the optimized 12-pole SynRM

Symbol	Variable	Value	Unit
D_{so}	Stator outer diameter	502.4	mm
D_{si}	Stator inner diameter	346.7	mm
D_{ro}	Rotor outer diameter	344.3	mm
D_{ri}	Rotor inner diameter	158.1	mm
h_{ts}	Stator tooth height	46.6	mm
b_{ts}	Stator tooth width	7.0	mm
g	Air-gap length	1.2	mm
l_{st}	Stack length	372.2	mm
-	Volume	0.0742	m^3
Q_s	Number of stator slots	72	-
N	Number of turns per phase	864	-
p	Number of pole pairs	6	-
b	Number of barriers per pole	4	-
n	Synchronous speed	500	rpm
f	Frequency	50	Hz
V_n	Rated phase voltage	380	Vrms
J_n	Rated current density	3	$Arms/mm^2$

k_s	Stacking factor	0.95	-
e	Lamination thickness	0.35	mm
k_{air}	Insulation ratio	0.59	-

In Table C.8, the main data of the optimized 12-pole RF-PMSM assessed in Section 5.4.1 is presented, encompassing main dimensional parameters.

Table C.8 Main data of the optimized 12-pole RF-PMSM

Symbol	Variable	Value	Unit
D_{so}	Stator outer diameter	582.2	mm
D_{si}	Stator inner diameter	365.2	mm
D_{ro}	Rotor outer diameter	324.0	mm
D_{ri}	Rotor inner diameter	201.2	mm
h_{ts}	Stator tooth height	69.4	mm
b_{ts}	Stator tooth width	37.4	mm
g	Air-gap length	3.0	mm
l_{st}	Stack length	284.2	mm
-	Volume	0.0757	m^3
Q_s	Number of stator slots	12	-
N	Number of turns per phase	72	-
p	Number of pole pairs	14	-
h_{pm}	Magnet height	16.4	mm
n	Synchronous speed	500	rpm
f	Frequency	50	Hz
V_n	Rated line-to-line voltage	380	Vrms
J_n	Rated current density	3	$Arms/mm^2$
k_s	Stacking factor	0.95	-
e	Lamination thickness	0.35	mm
α_{pm}	Arc-to-pole-ratio	0.86	-
B_r	Magnet remanence	1.125	T
$N_{PM,seg}$	Number of magnet radial segments	5	-